

2014

Neutron Scattering Studies of Unusual Spin Structure and Local Correlation in Complex Oxides

Dalgis Mesa

Louisiana State University and Agricultural and Mechanical College, dalgis450@gmail.com

Follow this and additional works at: https://digitalcommons.lsu.edu/gradschool_dissertations



Part of the [Physical Sciences and Mathematics Commons](#)

Recommended Citation

Mesa, Dalgis, "Neutron Scattering Studies of Unusual Spin Structure and Local Correlation in Complex Oxides" (2014). *LSU Doctoral Dissertations*. 1284.

https://digitalcommons.lsu.edu/gradschool_dissertations/1284

This Dissertation is brought to you for free and open access by the Graduate School at LSU Digital Commons. It has been accepted for inclusion in LSU Doctoral Dissertations by an authorized graduate school editor of LSU Digital Commons. For more information, please contact gradetd@lsu.edu.

NEUTRON SCATTERING STUDIES OF UNUSUAL SPIN STRUCTURE AND
LOCAL CORRELATION IN COMPLEX OXIDES

A Dissertation

Submitted to the Graduate Faculty of the
Louisiana State University and
Agricultural and Mechanical College
in partial fulfillment of the
requirements for the degree of
Doctor of Philosophy

in

The Department of Physics and Astronomy

by
Dalgis Mesa
B.S., Florida International University, 2007
May 2014

This thesis work is dedicated to my late grandmother Isabel Leyva Chavez; I wish you could have been here with me to celebrate this accomplishment, to my amazing mother Dalgis Rosales, and to my precious two little boys Owen Shane Donovan and Evan Walker Donovan.

Acknowledgements

This work could not have been possible without the best—yes, really—the best-graduate advisor ever: Dr. Jiandi Zhang. I can't count the many discussions, mentoring sessions, and encouraging words that Dr. Zhang has always had for me. I am very thankful that he always considered me—and all of his students—part of his extended family. In January 2010, I reluctantly followed him to Louisiana State University and now looking back I know it was one of the best decisions I have ever made. His patience, encouragement, and love for physics held me together all the way until the completion of my Ph.D.

A very special place is reserved for Dr. Jaime Fernandez-Baca, he has very patiently taught me the beauty of neutron scattering and has always been available to answer all of my questions. I consider myself very fortunate to have had such a knowledgeable and respected mentor in the field of neutron scattering. Special thanks also to Dr. Feng Ye and Dr. Songxue Chi for helping me with all the instrumental set up, data collection, and for providing me with their expertise in neutron scattering. I am very thankful for all those nights they accompanied me in the lab and helped me gather all the data, while their family was waiting for them at home. I couldn't have made it this far in graduate school without the help, expertise, and mentoring from Jaime, Feng, and Songxue.

I owe so much to my true friends from Florida International University: Vashti Sawtelle, Priscilla Pamela, Idaykis Rodriguez, Sarah E. Bryan-Reynoso, Francisco Reynoso, Cristobal Ceron and Luis Lebolo. We all started our journey in academia together and throughout the years we have always been there for each other. I truly cherish and will always keep close to my heart all we went through together, which includes but is not limited to: parties, laughs, tears, fears, frustrations, notes, long qualifying studying sessions, long weekends on Jackson problems, and

last but not least the love and passion for Physics; if I had to do it all over again I wouldn't change a thing.

Finally, I am eternally thankful to my family. My success would not have been possible without their love and support every step of the way. I thank my mother Dalgis Rosales and my father Ezequiel Lazo, for having the courage of leaving everything behind and starting life from zero in the United States. I owe so much to my late grandmother Isabel Leyva and late grandfather Armantino Rosales for taking care of me since I was a little girl, for all their wisdom, and for those sweet glasses of 'café con leche' my grandma always brought me to bed before school. I know that wherever you are you are proud of me and for that I thank you. I am grateful to my in-laws and all of Sean's family who has cheered for me all the way and who always have let me know how proud they are of all my accomplishments. There are no words to express how appreciative I am of all the love, patience, and support that my husband Sean Donovan always had for me through all these tough years full of long nights, stress, and many trips to Oak Ridge for experiments. He has given me the greatest gift of all—my two boys, Owen and Evan; they have been the inspiration and reason to keep going all the way.

Table of Contents

Acknowledgements.....	iii
List of Tables.....	vii
List of Figures.....	viii
Abstract.....	xi
Chapter 1. Introduction.....	1
1.1 Outline of the Work.....	1
1.2 Current Challenges in Solid-State Physics: The Case for Complexity.....	4
1.3 Mechanisms Responsible for the Strong Interplay in Transition-Metal Oxides...	8
1.3.1 Crystal Structure.....	9
1.3.2 Electronic Structure.....	9
1.3.3 Crystal Field Effect.....	10
1.3.4 Quenching of Orbital Angular Momentum and Spin-Orbit Coupling....	12
1.3.5 Spin States and Jahn-Teller Effect.....	14
1.4 Focus of this Thesis.....	15
1.4.1 Ruthenium Oxides.....	16
1.4.2 Manganese Oxides.....	21
1.5 Neutron Scattering as an Experimental Condensed Matter Physics Probe.....	27
1.5.1 Why Neutrons?	27
Chapter 2. Neutron Scattering	31
2.1 Basic Properties of Neutrons.....	31
2.2 Basic Principles of Neutron Scattering	33
2.2.1 Elastic Scattering	34
2.2.2 Inelastic Scattering	36
2.3 Mathematical Foundations of Neutron Scattering: Van Hove Formalism.....	37
2.3.1 Fermi's Golden Rule and the Born Approximation: The Master Formula	39
2.3.2 The Correlation Function.....	43
2.3.3 Coherent and Incoherent Scattering.....	44
2.3.4 Coherent Elastic Scattering: Nuclear and Magnetic.....	46
2.3.5 Inelastic Scattering: Phonons and Magnons	54
2.3.6 Diffuse and Quasielastic Magnetic Scattering.....	59
Chapter 3. Experimental	62
3.1 Neutron Production and Detection.....	62
3.2 Single Crystal Synthesis.....	65
3.3 Triple-Axis Spectrometers.....	65
3.4 Single Crystal Diffractometers.....	77

Chapter 4. Magnetic Structure of $\text{Sr}_3(\text{Ru}_{1-x}\text{Mn}_x)_2\text{O}_7$ ($x = 0.125, 0.16$).....	81
4.1 Introduction.....	81
4.2 Properties of $\text{Sr}_3(\text{Ru}_{1-x}\text{Mn}_x)_2\text{O}_7$ ($x = 0.16$).....	82
4.2.1 Experimental Details.....	84
4.2.2 Magnetic Structure.....	85
4.3 $\text{Sr}_3(\text{Ru}_{1-x}\text{Mn}_x)_2\text{O}_7$ ($x = 0.125$).....	92
4.3.1 Experimental Details.....	93
4.3.2 Magnetic Structure	94
4.4 Summary	98
 Chapter 5. A Study on the Doping Dependence of Phase Segregation in the Colossal Magnetoresistive Manganite $\text{Pr}_{1-x}\text{Ca}_x\text{MnO}_3$ ($x = 0.30, 0.35, \text{ and } 0.40$).....	100
5.1 Introduction.....	100
5.2 Properties of $\text{Pr}_{1-x}\text{Ca}_x\text{MnO}_3$ ($x = 0.30, 0.35, \text{ and } 0.40$).....	101
5.3 Experimental Details	103
5.4 Doping Dependence of Phase Segregation.....	106
5.5 Summary.....	113
 Chapter 6. A Preliminary Study on Spin-Lattice Coupling in the Colossal Magnetoresistive Manganite $\text{La}_{1-x}\text{Ca}_x\text{MnO}_3$ ($x = 0.20$).....	115
6.1 Properties of $\text{La}_{1-x}\text{Ca}_x\text{MnO}_3$ ($x = 0.20$).....	115
6.2 Experimental Details	120
6.3 Spin-Lattice Coupling.....	121
6.4 Summary.....	126
6.5 Future Work.....	126
 Chapter 7. Conclusions.....	129
 References.....	131
 Appendix: Letter of Permission	139
 Vita.....	140

List of Tables

TABLE 2.1	Basic Properties of Neutrons.....	31
TABLE 2.2	Standard Values for Thermal Neutrons.....	33
TABLE 5.1	The integrated intensity ratios of the magnetic diffuse and total (diffuse plus Bragg) scattering vs. doping in the ground state at 10 K	106

List of Figures

FIGURE 1.1	Phase diagrams of several representative transition-metal oxides	5
FIGURE 1.2	Schematic representation of the unit cell of a cubic perovskite of the form ABO_3	10
FIGURE 1.3	Angular distributions of the five d -orbitals resulting from the crystal field splitting.....	12
FIGURE 1.4	Schematic representation of the splitting of the d -levels under the crystal field for a hypothetical system with $3d^6$ configuration.....	15
FIGURE 1.5	Crystal structures of the Ruddlesden-Popper (RP) series of layered perovskites, $Sr_{n+1}Ru_nO_{3n+1}$ ($n = 1, 2, 3, \dots \infty$).....	17
FIGURE 1.6	Schematic representations of the energy levels of the $4d$ -orbitals.....	18
FIGURE 1.7	A schematic representation of the latest reported phase diagram for various substitution concentrations (x) of the $Sr_3(Ru_{1-x}Mn_x)_2O_7$ series...	20
FIGURE 1.8	Phase diagram as a function of temperature and Ca content and temperature dependence of the resistivity under various applied magnetic fields for the perovskite manganite $Pr_{1-x}Ca_xMnO_3$	24
FIGURE 1.9	Phase diagram as a function of temperature and Ca concentration and measurement of microscopic quantities for the perovskite manganite $La_{1-x}Ca_xMnO_3$	25
FIGURE 1.10	Schematic representation of the Double Exchange mechanism.....	26
FIGURE 1.11	Schematic representations of the energy levels of the $3d$ -orbitals in manganese oxide systems.....	26
FIGURE 2.1	The Ewald circle in two-dimensions representing the reciprocal space...	36
FIGURE 2.2	Geometry for scattering experiments.....	38
FIGURE 2.3	Coordinate system with the origin set at some arbitrary point in the scattering system.....	39
FIGURE 2.4	Neutron scattering profile in reciprocal (left) and real space (right) where the neutron scattering cross section's Fourier transform is the so called time dependent spin-spin correlation function.....	51

FIGURE 2.5	Anisotropic nature of magnetic scattering.....	53
FIGURE 2.6	Schematic representation of a spin wave.....	58
FIGURE 3.1	Schematic representation of the set up of a triple axis neutron scattering spectrometer.....	67
FIGURE 3.2	Schematic diagram of spin flip vs. non-spin flip processes in polarized neutron scattering.....	72
FIGURE 3.3	Non-spin flip (blue) and spin flip (red) of the spin wave excitation spectrum for the CMR manganite system $\text{La}_{0.70}\text{Ca}_{0.3}\text{MnO}_3$	72
FIGURE 3.4	Schematic diagram of the HB-2C US/Japan Wide-Angle Neutron Diffractometer located at the HFIR at ORNL.....	78
FIGURE 3.5	The HB-3A Four-Circle Diffractometer at the HFIR.....	79
FIGURE 4.1	A schematic representation of the latest reported phase diagram for various substitution concentrations (x) of the $\text{Sr}_3(\text{Ru}_{1-x}\text{Mn}_x)_2\text{O}_7$ series..	81
FIGURE 4.2	Physical property measurements of $\text{Sr}_3(\text{Ru}_{1-x}\text{Mn}_x)\text{O}_7$ ($0 < x < 0.7$).....	83
FIGURE 4.3	T -dependence of the integrated magnetic scattering intensity at chosen AFM Bragg peaks for the $\text{Sr}_3(\text{Ru}_{0.84}\text{Mn}_{0.16})_2\text{O}_7$ taken with the HB-1A triple-axis spectrometer.....	86
FIGURE 4.4	Neutron diffraction patterns of SRMO 16 in the $(H, K, 0)$ and $(H, 0, L)$ reciprocal planes for temperatures above and below T_N	87
FIGURE 4.5	Neutron diffraction profiles at magnetic Bragg peaks.....	90
FIGURE 4.6	Fit of the Bragg intensity, I_B , in arbitrary units vs. Temperature of the magnetic superlattice peak $(0.5, 0, 0)$ to the power law scaling function.....	91
FIGURE 4.7	Schematic E -type AFM spin configuration in the ground state of SRMO 16 resulting from a magnetic refinement.....	92
FIGURE 4.8	Neutron diffraction patterns of SRMO 12.5 in the $(H, K, 0)$ and $(H, 0, L)$ reciprocal planes for temperatures above and below T_N	95
FIGURE 4.9	Temperature dependence of the integrated magnetic scattering intensity for the $(0.5, 0, 0)$ AFM Bragg peaks.....	97

FIGURE 5.1	Schematic representation of the ab -plane of the CE-type structure with both orbital ($d_{3x^2-r^2}/d_{3y^2-r^2}$) and spin orderings.....	101
FIGURE 5.2	Schematic diagrams of the charge distribution scenarios in perovskite manganites with ground state near $x = 0.5$	102
FIGURE 5.3	Schematic representations of probed peak positions in reciprocal space and representative q -scan profiles for various doping concentrations.....	105
FIGURE 5.4	Representative q -scan profiles of the long- and short-range charge-ordered (CO), ferromagnetic (FM), and antiferromagnetic (AF) correlations in single crystals of PCMO30 and PCMO40.....	108
FIGURE 5.5	T -dependence of the FM diffuse component measured at $(0.96, 0, 0)$ ($\Delta q = 0.4$ r.l.u) for different Ca-concentrations of $\text{Pr}_{1-x}\text{Ca}_x\text{MnO}_3$ on cooling (solid symbols) and warming (open symbols).....	110
FIGURE 5.6	T -dependence of the intensity and extracted short-range correlation length of (top panel) FM at $(1, 0, 0)$ and (bottom panel) Mn^{4+} AF at $(0.5, 0, 0)$ diffuse scattering in PCMO30.....	111
FIGURE 5.7	T -dependence of order parameters for (a) charge-/orbital-ordering (CO) measured at $(2.25, 0.25, 0)$, (b) Mn^{3+} AF ordering at $(0.75, 0.25, 0)$, and (c) Mn^{4+} AF ordering at $(0.5, 0, 0)$, for three different Ca-concentrations of $\text{Pr}_{1-x}\text{Ca}_x\text{MnO}_3$	114
FIGURE 6.1	Schematic representation of the Super Exchange mechanism.....	118
FIGURE 6.2	Anomalous spin wave behavior and ferromagnetic domains (FM) with super-exchange (SE) couplings reported from neutron scattering experiments.....	119
FIGURE 6.3	Schematic diagram of probed peak positions and scan direction (denoted by the black arrow) in reciprocal space.....	121
FIGURE 6.4	Experimental results on the LCMO20 single crystal specimen.....	122
FIGURE 6.5	Spin wave dispersion relations of our experimental results and previously reported ones.....	125

Abstract

Complex correlated electron materials (CEMs), such as transition-metal oxides with exotic properties and novel functionalities, present immense opportunities and formidable challenges in condensed matter physics, materials science, and engineering. These systems are characterized by a multitude of competing ground states that result from the close coupling between charge, lattice, orbital, and spin degrees of freedom, which can be tuned by chemical substitution, strain induction, or by the application of external stimulus (e.g. pressure, temperature, electric, or magnetic fields). Interest in CEMs is fueled by the richness of their novel properties (e.g. Colossal Magnetoresistance (CMR), Quantum Criticality, and High Temperature Superconductivity), the complexity of the underlying physics, and the promise of technological applications. In this work, elastic and inelastic neutron scattering is used to study two prototypes of CEMs: ruthenates and manganites. Our work on ruthenates has revealed the magnetic structure and dimensionality of the order parameter in the bilayered ruthenate $\text{Sr}_3(\text{Ru}_{1-x}\text{Mn}_x)_2\text{O}_7$ for manganese (Mn) concentrations of 12.5 and 16%. Results indicate 1) an unusual *E-type* antiferromagnetic structure with moments aligned along the *c*-direction exhibiting only single-bilayer (5-6 Å) ferromagnetic correlations along the *c*-direction, and 2) that Mn concentration is responsible for the stabilization of the long-range *E-type* AFM ordering observed along the basal plane. The investigation on the evolution of long- and short-range charge-ordered (CO), ferromagnetic, and antiferromagnetic correlations in single crystals of $\text{Pr}_{1-x}\text{Ca}_x\text{MnO}_3$ for various hole-doping concentrations has 1) provided direct evidence of magnetic phase separation and 2) revealed a critical doping concentration close to ($x = 0.35$) that divides the inhomogeneous from homogenous CO state. Preliminary studies of spin and lattice excitations in the ferromagnetic insulating phase of $\text{La}_{1-x}\text{Ca}_x\text{MnO}_3$ indicate an anomalous softening and broadening of the

magnons near the zone boundary, where a longitudinal optical phonon is present, indicating that magnon-phonon coupling could play a critical role in the behavior of the spin wave dispersion of these systems. The work presented in this thesis should be a forward step towards the understanding of the nature of the competing interactions present in these CEMs, which result in the emergence of exotic phenomena and novel functionalities.

Chapter 1

Introduction

1.1 Outline of the Work

In this work, neutron scattering is used to investigate spin structure and local correlation in two prototypes of strongly correlated materials both belonging to the same perovskite structure family: manganese-substituted ruthenium oxides and hole-doped manganese oxides. The former, also referred to as ruthenates, belongs to the series of the layered perovskite type $\text{Sr}_{n+1}\text{Ru}_n\text{O}_{3n+1}$ ($n = 1, 2, 3, \dots \infty$). Manganese oxides, widely known as manganites, have the general formula $\text{R}_{1-x}\text{A}_x\text{MnO}_3$ where R and A are the trivalent rare and divalent alkaline earth ions, respectively.

Chapter 1 begins with an introduction of the complex behavior that characterizes the correlated electron systems featured in this investigation. The concept of complexity and its consequences for solid-state physics within the context of this work are also discussed. This chapter continues with an overview of the mechanisms responsible for the rich physics in these compounds and basic background information on the two types of transition metal oxides featured in this investigation. Finally, we state the main motivation for our work and provide a first glimpse into the experimental technique chosen to carry out this study.

The principles of neutron scattering are described in more detail in Chapter 2. The basic properties of neutrons are covered first. The rest of the chapter is devoted to a presentation of the mathematical foundations of the neutron scattering technique following the Van Hove formalism.

Chapter 3 contains the experimental details of the work. The beginning of the chapter briefly describes neutron production and detection, and provides an overview of the single crystal synthesis of the materials used in the study. The rest of the chapter is devoted to the description of the neutron instrumentation and consequently of the beam lines used in this investigation.

The next three chapters are the core of this thesis work. Each chapter is devoted to a specific study and as such each contains the current state of the research relevant to each topic/material investigated.

Experimental results on lattice and magnetic structure determination of 12.5 and 16% manganese (Mn)-substituted $\text{Sr}_3\text{Ru}_2\text{O}_7$ using elastic neutron scattering are presented and discussed in detail in Chapter 4. Our studies reveal an unusual *E*-type antiferromagnetic (AFM) structure in Mn-substituted $\text{Sr}_3\text{Ru}_2\text{O}_7$ ($x = 0.16$ and 0.125). Results on the 16 % concentration [1] indicate the existence of a quasi-two-dimensional (2D) antiferromagnet with in plane (*ab*) long-range ordering exhibiting only single-bilayer (5-6 Å) ferromagnetic (FM) correlations along the *c*-direction below the AFM transition temperature ($T_N = 78$ K). However, the critical behavior of the staggered magnetization, the AFM order parameter, does not reflect the expected behavior of a 2D magnetic phase transition. Such an unusual magnetic structure deviates from what would be expected from the conventional spin-lattice coupling scenario in this class of materials. Similarly, studies on the 12 % Mn-substituted $\text{Sr}_3\text{Ru}_2\text{O}_7$ confirm the short-range (single-bilayer) FM correlations out of plane. However, in sharp contrast to the 16 % Mn-substituted $\text{Sr}_3\text{Ru}_2\text{O}_7$ system, a finite correlation length of only a few unit cells characterizes the *E*-type AFM spin distribution along the basal plane. Thus, demonstrating that the amount of Mn-concentration in $\text{Sr}_3\text{Ru}_2\text{O}_7$ has a direct impact on the stabilization of the long-range *E*-type antiferromagnetic spin texture that characterizes this system at higher Mn concentrations. Reprinted abstract, figures and excerpts with permission from D. Mesa, F. Ye, S. Chi, J. A. Fernandez-Baca, W. Tian, B. Hu, R. Jin, E. W. Plummer, and J. Zhang, Physical Review B **85**, 180410(R) (2012) (<http://link.aps.org/abstract/PRB/v85/p180410>). Copyright (2012) by the American Physical Society.

In Chapter 5 we describe the elastic part of our work on manganese oxides: the evolution of long- and short-range charge-/orbital-ordered (CO-OO), ferromagnetic (FM), and antiferromagnetic (AF) correlations in $\text{Pr}_{1-x}\text{Ca}_x\text{MnO}_3$ ($x = 0.3, 0.35$ and 0.4) [2]. Our results indicate that the existence and population of spin clusters are found to drastically depend on the doping concentration (x). Populous spin clusters coexist with long-range canted AF order over a wide temperature range in $x = 0.3$ while they do not appear in $x = 0.4$ crystal. In contrast, both CO and AF order parameters in the $x = 0.35$ crystals show a precipitous decrease below 35K, which corresponds to the temperature at which spin clusters form. These results provide direct evidence of magnetic phase separation and indicate that there is a critical doping level x_{cr} (close to $x = 0.35$) that divides the inhomogeneous from homogeneous CO-OO ground state. Reprinted figures and excerpts with permission from H. Sha, F. Ye, P. Dai, J. Fernandez-Baca, D. Mesa, J. Lynn, Y. Tomioka, Y. Tokura, and J. Zhang, *Physical Review B* **78**, 052410 (2008) (<http://link.aps.org/abstract/PRB/v78/p052410>). Copyright (2008) by the American Physical Society.

Chapter 6, a preliminary inelastic neutron scattering investigation revealing a spin-lattice coupling in the colossal magnetoresistance manganite $\text{La}_{1-x}\text{Ca}_x\text{MnO}_3$ ($x = 0.20$) is presented. Dispersion relations for both phonons and spin waves along selected directions were obtained for temperatures of 5 and 225 K, respectively. At low temperatures, our results indicate an anomalous softening and broadening of the magnons near the zone boundary, especially near $E = 20$ meV, where a longitudinal optical phonon is present. Our results suggest that magnon-phonon coupling could be a driving force behind the anomalous behavior and gaps observed in the spin wave dispersion, which suggests that this correlation (i.e. that of spin and lattice) could play an

important role in the peculiar FM insulating phase ($x = 0.20$) of perovskite manganites. Finally, the present work is summarized in Chapter 7.

1.2 Current Challenges in Solid-State Physics: The Case for Complexity

Highly correlated electron materials (CEMs) are at the very forefront of condensed matter physics research. In these systems, the grand challenge is to accurately understand the electrical and magnetic properties for 10^{23} strongly interacting particles. Transition-metal oxides, such as the ones featured in this investigation, belong into the class of CEMs. These are materials in which the movement of one electron depends on the position and movement of its neighboring, and often next neighboring electrons as a result of the long-range Coulomb interaction. As a consequence, the electronic structure of these systems cannot be described from single-particle models (e.g. the Free electron Fermi gas, Fermi liquid, or Band Theory) found in an introductory solid-state physics course. In fact, what makes these materials so interesting is that such strong interaction between the electrons results in the emergence of systems with novel macroscopic collective behavior that cannot be understood by examining its single constituents. As a result, these materials are recognized in the scientific community as complex systems [3]. Figure 1.1 shows the multiple phases and rich physics that characterizes some representative complex systems that have been at the center of present-day interest in the solid-state physics community.

The bilayer perovskite $\text{Sr}_3\text{Ru}_2\text{O}_7$ shown in Figure 1.1a has generated a lot of interest in the past years after it was reported to exhibit a magnetic field-induced quantum critical point (QCP) [4].

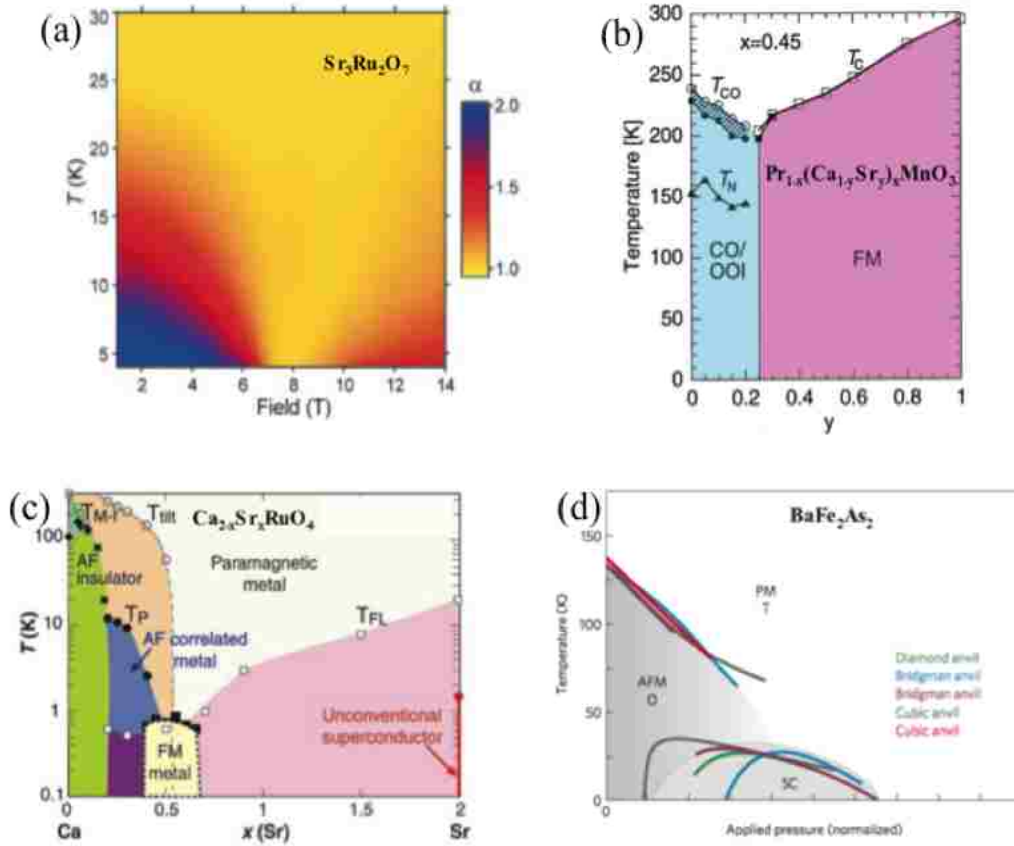


FIGURE 1.1 Phase diagrams of several representative transition-metal oxides. (a) Temperature-Applied Magnetic Field phase diagram of $\text{Sr}_3\text{Ru}_2\text{O}_7$ [4]. (b) Electronic phase diagram of $\text{Pr}_{1-x}(\text{Ca}_{1-y}\text{Sr}_y)_x\text{MnO}_3$ [5]. (c) Phase diagram as a function of doping concentration (x) for $\text{Ca}_{2-x}\text{Sr}_x\text{RuO}_4$ [6]. (d) Applied-pressure phase diagram for BaFe_2As_2 using different techniques [7]. Panels are adapted from cited references.

The high temperature resistivity phase diagram as a function of the applied magnetic field along the c direction shows evidence of the proximity to a metamagnetic QCP at a field of ~ 7.8 T as indicated by the exponent α . The data was analyzed from the general expression for resistivity $\rho(T) = \rho_{\text{res}} + AT^\alpha$, where ρ_{res} is the resistivity at $T = 0$ due to elastic scattering, A is related to the effective quasi-particle mass, and α contains information pertinent to the nature of the metallic state. In the color plot, there is a region where the power of α falls and maintains a power of 1 for temperatures as low as 4.5 K. This is indicative of new emergent behavior as a

value of $\alpha \neq 2$ falls outside the predictions of the Fermi liquid theory of correlated electron metals. Moreover, as the metamagnetic transition is eminent, the system is characterized by strong critical fluctuations and it is speculated that such can bring about the stabilization of a novel form of low-temperature order. In fact, there is reported evidence that an electronic-like nematic phase has been observed [8] after a further decrease in temperature. Thus, the discovery of this new form of QCP is not only interesting in its own right, but it provides researchers with perhaps a finer tuning parameter—magnetic field—besides hydrostatic pressure and chemical composition in order to induce QCP with the aim of stabilizing novel ground states. The complexity of the underlying physics and novel properties displayed by this particular class of transition-metal oxides will be discussed in more detail in Chapter 4.

Despite being a mature research area with thousands of publications in the last 30 years, manganites still remain at the forefront of condensed matter investigations because still to this date the details of the underlying physics behind the colossal magnetoresistance (CMR) effect (a large drop in resistivity upon magnetic field exposure) remain controversial [9]. Figure 1.1b shows the electronic phase diagram of $\text{Pr}_{1-x}(\text{Ca}_{1-y}\text{Sr}_y)_x\text{MnO}_3$ with $(0 \leq y \leq 1)$ and $x = 0.45$. Upon increasing doping concentration and changing the temperature, the system evolves from antiferromagnetic insulator to charge- and orbital-order insulator (CO/OO-I), and finally to a ferromagnetic (FM) metal. The Néel Temperature (antiferromagnetic (AF) transition temperature) T_N is indicated by the solid triangles while T_{CO} , and T_C are the charge order and Curie temperature (FM transition temperature), respectively. In addition to the phase coexistence and inhomogeneity that characterizes this systems, this compound has also been reported [10] to exhibit highly anisotropic spin texture similar to that of smectic phases predicted in doped Mott insulators and to show first evidence of an “electronically soft phase” in CMR manganites.

Figure 1.1c offers yet another example illustrating the intriguing and complex physics in a layered systems. It shows the phase diagram for the single-layer $\text{Ca}_{2-x}\text{Sr}_x\text{RuO}_4$ (CSRO), in which the Mott insulator Ca_2RuO_4 evolves into the spin triplet superconductor Sr_2RuO_4 [11]. The richness of the ground state in CSRO is attributed to the isovalent cation substitution of the smaller Ca^{2+} for the bigger Sr^{2+} ion. The latter induces a series of structural phase transitions characterized by rotations or tilts of the RuO_6 octahedra. As seen from the phase diagram, the system starts with a tetragonal structure for Sr_2RuO_4 , changes to a structure with RuO_6 rotational distortion up to $\text{Ca}_{1.5}\text{Sr}_{0.5}\text{RuO}_4$, and culminates with an orthorhombic structure for Ca_2RuO_4 [12]. These structural deformations have a direct impact on the electronic and magnetic properties; they give rise to an array of ground states starting from an unconventional superconducting state in Sr_2RuO_4 , to a quantum critical point at $x = x_c \sim 0.5$, and to a Mott insulating phase with antiferromagnetic order in Ca_2RuO_4 [12]. The 1st-order metal-insulator transition (MIT) character, the strong doping dependence of T_C , and other unusual electronic and magnetic properties indicate that both lattice and orbital degrees of freedom play important roles in MIT. Around $x = x_c \sim 0.5$, the quantum critical point is implied by a critical enhancement of low-temperature susceptibility but is concurrent with the tilt structural distortion. All of these clearly demonstrate the existence of strong spin-lattice-orbital correlations in CSRO, which are responsible for the complexity exhibited by these systems.

The applied-pressure phase diagram for BaFe_2As_2 (Ba based-122) as a function of external pressure applied under various levels of hydrostaticity is shown in Figure 1.1d. This Ba-based 122 system is currently one of the most studied out of the five families of Fe-based superconductors after the shocking report of Fe-based superconductivity at the 2008 American Physical Society meeting in New Orleans, LA [13]. In contrast to previous figures where applied

magnetic field and chemical substitution were used to induce novel ground states, this is a case where applied pressure is the external parameter. As the phase diagram shows, superconductivity arises as the AFM order is suppressed while lowering the temperature of the system induces a structural phase transition from tetragonal to orthorhombic [7].

The nature of the complexity that characterizes CEM stems from their soft electronic structure; their ground state is elegantly poised inside the interwoven fabric of charge, lattice, orbital, and spin degrees of freedom. New ground states emerge with minor changes in external parameters (e.g., chemical substitution, pressure, magnetic fields, and temperature). These new ground states, accompanied by complex collective behavior such as charge-/orbital ordering, cooperative Jahn-Teller distortions, magnetic exchange interactions, etc. give rise to exotic properties and novel functionalities such as quantum critical behavior, colossal magnetoresistance, and high temperature superconductivity.

The main motivation and current challenge behind the study of these systems lies in trying to search for answers to the most fundamental questions: How do the macroscopic properties of these systems evolve from the various ordering phenomena? How to successfully disentangle/understand couplings between different degrees of freedom in order to reveal lattice and spin structure? How to stabilize fluctuations with the aim of exploring new properties and functionalities?

1.3 Mechanisms Responsible for the Strong Interplay in Transition-Metal Oxides

It is out of the scope of this thesis work to provide a detail account of the main mechanisms responsible for the rich physics found in transition-metal oxides. Rather, this section presents the reader with a qualitative overview of the underlying physics of the complex systems treated in this investigation. The topics covered in this section are what we can consider part of the jargon

of condensed matter physics and thus for the sake of avoiding reference redundancy, the reader is urged to consult [14 - 19] if further clarification/detail is needed with these introductory topics.

1.3.1 Crystal Structure

The crystal structure of the CEMs featured in this investigation—manganese and ruthenium oxide—can be obtained from the ideal perovskite structure denoted by ABO_3 . A schematic diagram of the three-dimensional ideal cubic perovskite structure can be seen in Figure 1.2. Each transition-metal ion [B] (in red sphere) is surrounded by six oxygen ions [O] (blue dots), forming in this way an octahedron (which is the building block of these class of materials); where the larger metal cation [A] (yellow corner spheres) stabilizes the lattice. This simple cubic structure is rarely realized, instead the final structure results from the difference in the ionic radii of the A and B ions, which introduces tilts and rotations of the oxygen octahedra. As a result, distorted cubic perovskite structures of orthorhombic, and tetragonal settings are common in these types of transition-metal oxides. The pure compound $LaMnO_3$, is an example of such orthorhombic structure with space group $Pbnm$.

1.3.2 Electronic Structure

When describing the electronic structure of solids, two approaches are usually taken: the ionic models or the band structure models [20]. The latter are usually applied to metallic solids since extended electron states are calculated based on the wave function of an electron in a periodic potential. On the other hand, ionic models focus on the properties of individual atoms instead, thus providing a naïve but qualitatively rich picture of energy levels of both the ground and excited states of solids, and especially of insulators. Thus, for the purposes of this thesis and during the discussion of some of the mechanisms responsible for the strong interplay between the different degrees of freedom in these transition-metal oxides, we will assume that these d -

electron systems occupy well-localized, ionic states. That is, we are neglecting covalency¹ (and therefore are assigning each ion an integral charge which is given by its oxidation state) and are assuming that systems are essentially Mott Insulators that can be described by a purely ionic model.

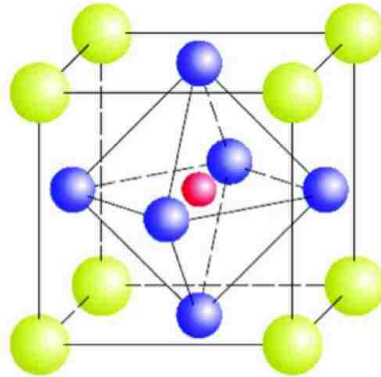


FIGURE 1.2 Schematic representation of the unit cell of a cubic perovskite of the form ABO_3 . The red sphere denotes the transition-metal ion (B) embedded in a cubic array of corner-sharing BO_6 octahedra with blue spheres as oxygen ions. The green spheres represent the di- or trivalent cation (A) which form the AO_2 planes that separate the BO_2 horizontal planes. Figure adapted from [17].

1.3.3 Crystal Field Effect

The existing oxygen octahedral environment surrounding the transition-metal ion, results in the so-called crystal field effect. The latter is insignificant for rare earth ions, since their partially filled $4f$ shells are buried under higher shells ($5s$ and $5p$). On the other hand, for the outermost electronic shells—the partially filled d -electron shells—the electrostatic potential created by the surrounding oxygen ions has profound consequences. It causes the splitting of the five-fold degeneracy of the transition-metal ion.

Group theory reveals that the crystal field effect lifts the five-fold degeneracy of the d -electron system into the two- and three-fold degenerate E and T_2 levels, commonly referred to as

¹ The symmetry analysis of orbitals is unaffected by this assumption.

the e_g and t_{2g} orbitals², respectively. In an environment where the d -electrons are exposed to the Coulomb repulsion of the negative charged ions, the quantum mechanical wave functions of an electron are given by the so-called tesseral harmonics, which are a combination of the spherical harmonics of general form $Y_l^m \pm Y_l^{-m}$. The general form of the E and T_2 levels are given by:

$$T_2 \begin{cases} xy \sim r^2(Y_2^2 - Y_2^{-2}) \\ xz \sim r^2(Y_2^1 - Y_2^{-1}) \\ yz \sim r^2(Y_2^1 + Y_2^{-1}) \end{cases} \quad (1.1)$$

and

$$E \begin{cases} x^2 - y^2 \sim r^2(Y_2^2 + Y_2^{-2}) \\ 3z^2 - r^2 \sim r^2 Y_2^0 \end{cases} \quad (1.2)$$

The order of the levels and the size of the splitting are analyzed using ligand field theory by going beyond the ionic model, thus taking into account the hybridization that occurs between then d - and p -orbitals of the transition-metal cation and the oxygen anions. Figure 1.3 shows the angular distribution of the five d -orbitals in the crystal field. The value of the splitting between the energy levels is usually expressed as $10 Dq$ (standard notation in ligand field theory, (see e.g. [21]) and results in a higher e_g orbital energy than that of the t_{2g} . This is evident from the orientation of the orbitals with respect to the oxygen environment. The wave functions of the e_g orbitals have lobes that extend along the direction of the bond between the transition-metal ion and the oxygen, being exposed in this way to a greater Coulomb repulsion from the negatively charged oxygen ions. On the other hand, the t_{2g} lobes point away from such bond and as a result occupy a lower energy level.

² This is standard notation used in group theory. Within this theory, the rotations of the octahedral group characterize the symmetry of the crystal field. The subscript g is from the German word *gerade*, which refers to the use of even functions.

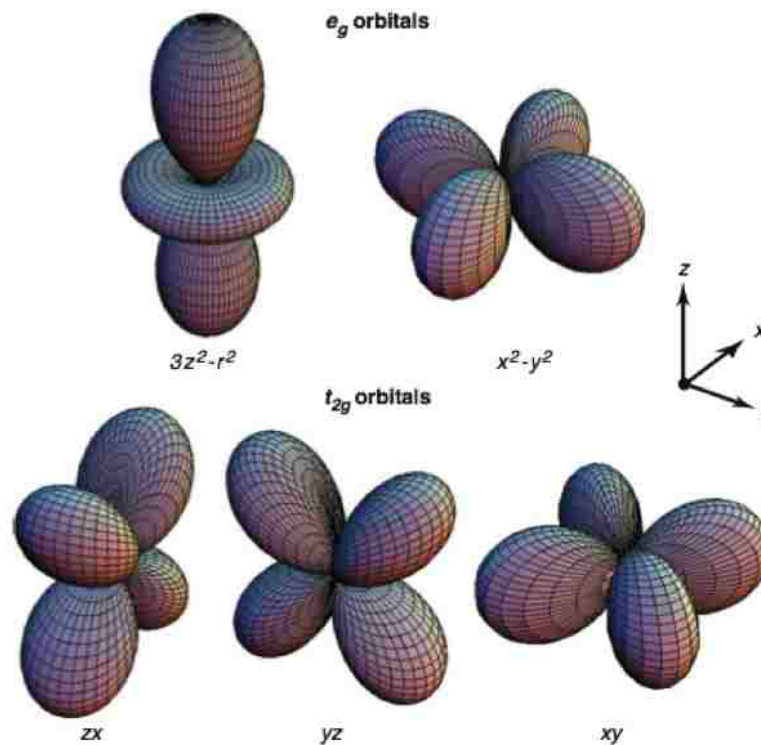


FIGURE 1.3 Angular distributions of the five d -orbitals resulting from the crystal field splitting. The fivefold degeneracy is lifted into the lower energy t_{2g} orbitals $[(zx), (yz), (xy)]$ and the higher energy $[(3z^2-r^2), (x^2-y^2)]$ e_g orbitals [22].

1.3.4 Quenching of Orbital Angular Momentum and Spin-Orbit Coupling

In addition to the lifting of the five-fold degeneracy, the exposure of the partially filled d -shells of transition-metal ions to the anisotropic field created by the oxygen environment also causes the so-called quenching of the orbital angular momentum (and of the corresponding magnetic moment).

The origin of the quenching of angular momentum can be understood from equations (1.1) and (1.2). The eigenfunctions of the E and T_2 levels all have combinations of Y_2^m and Y_2^{-m} in equal proportions. Since Y_l^m are eigenfunctions of L with fixed $L_z = m$ and none of these wave functions have a definite L_z (i.e. they have equal proportions of $+2, -2, +1, -1$, etc.), we can then

conclude that $\langle \psi | L_z | \psi \rangle = 0$. The latter is a property of real wave functions, which simply states that a measurable quantity (an observable) must be real. Thus, since the crystal field requires $|\psi\rangle$ to be real, then $\langle \psi | L_z | \psi \rangle$ must be vanishing.

From a classical perspective, the quenching of the orbital angular momentum is attributed to the fact that L vanishes ($J = S$) due to its precession in a crystal field (i.e. L does not have a definite value), such that L^2 may continue to be constant but its components average to zero.

Depending on the transition-metal oxide, the orbital angular momentum can be partially restored if the spin-orbit coupling is sufficiently strong; if it is comparable to or larger than the crystal field. If such is the case, the crystal field levels can rearrange themselves so as to partially invalidate Hund's Third Rule. In that case, equations (1.1) and (1.2) are no longer valid, since now only J (as opposed to L and S) is a good quantum number. Thus, angular momentum is not quenched because the wave functions cannot be described in terms of L anymore.

The partial restoring of the orbital angular momentum can be understood by recalling that the ground states of ions with partially filled shells (e.g. *d-shells*) are governed by Hund's Rules and Pauli's exclusion principle. Hund's First and Second Rule determine the values of the spin and orbital angular momenta, respectively, leaving $(2L + 1)(2S + 1)$ possible states. The latter degeneracy is lifted by the spin-orbit coupling, which introduces the total angular momentum J , to the set of quantum numbers necessary to describe the ground states of ions (Hund's Third Rule). As a result, the transition-metal ion in the oxygen environment is not only subject to the crystal field effect, but also to the spin-orbit coupling. The treatment of such system (i.e. how the electrons will fill the shells) now requires a modification to Hund's Third Rule by adding the crystal field as perturbation to the $(2L + 1)(2S + 1)$ -fold set of states. As we will see shortly, such

modification will have different consequences for $3d$ (manganese) and $4d$ (ruthenium) transition-metal oxides.

Spin-orbit coupling introduces important effects to these transition-metal oxides systems. One is magnetic anisotropy, since now the spin can sense the orientation of the crystal axis. Second, the so-called exchange anisotropy due to its effect on the spin-spin interaction causing magnetism and related phenomena.

1.3.5 Spin States and Jahn-Teller Effect

Another interesting feature of these complex oxide systems is that electrons in the partially filled d -shells can occupy orbitals not allowed by Hund's first rule. A hypothetical example of such system is one with a $3d^6$ configuration in which $S = 2$ (according to Hund's First Rule) with four electrons occupying the lower lying t_{2g} states and the remaining 2 in the e_g (i.e. commonly denoted as $t_{2g}^4 e_g^2$). However, occasionally this high-spin state is not realized and the electrons re-arrange themselves so that $S = 0$ with t_{2g}^6 in what is referred to as the low-spin state (see Figure 1.4) Which spin state occurs is solely dependent on the nature of the system studied and as we will see in sections 1.4.1 and 1.4.2, this choice has profound implications on the magnetism (and in other degrees of freedom due to coupling) of the system.

The undoped compound LaMnO_3 , is an example of a system in which a high-spin configuration is preferred. The Mn^{3+} ion in the crystal field has $4d$ -electrons that occupy the orbitals such that $S = 2$. From the previous section we know that this arrangement quenches the orbital angular momentum of the system ($L = 0$) but also introduces an orbital degree of freedom to the state; the ionic ground state is doubly degenerate. That is, the electron cannot decide which orbital ($3z^2 - r^2$) or $(x^2 - y^2)$ to occupy. In this scenario, the electronic and lattice degrees of freedom couple and undergo what is referred-to as the *Jahn-Teller effect*. In the latter, the local

octahedral environment undergoes a further splitting of the orbitals facilitated by a geometric distortion that lowers the symmetry and the total energy of the system.

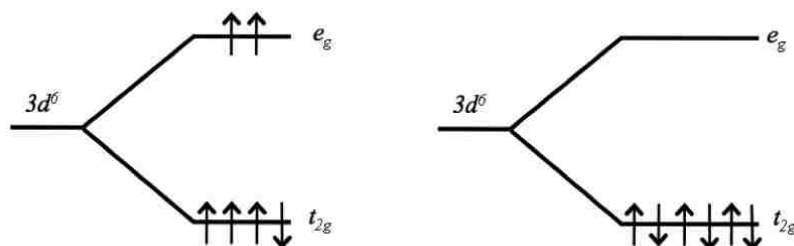


FIGURE 1.4 Schematic representation of the splitting of the d -levels under the crystal field for a hypothetical system with $3d^6$ configuration. Left: high-spin state with $S = 2$, right: low spin state with $S = 0$. Figure adapted from [15].

In fact, there is a plethora of correlated physics that owe its origin to the Jahn-Teller effect. In the well-studied LaMnO_3 system, there is a certain temperature at which it is favorable to order local distortions of the oxygen octahedron and thus minimize the interaction energy of the electrons. It is in this way that the system can undergo a structural phase transition through what is known as the cooperative Jahn-Teller effect. In addition, such localized Jahn-Teller distortions can become correlated as well, introducing in this way long range orbital order of the e_g electrons along the crystal.

1.4 Focus of this Thesis

The mechanisms presented in the previous section showcase the richness of the physics in these transition-metal oxide systems: the complex interplay between the structural-, orbital-, and spin-degrees of freedom. Here, we present the reader with a brief background necessary to understand the transition metal oxides featured in investigation as well as our motivation to study them.

1.4.1 Ruthenium Oxides

The crystal structures of the members of Ruddlesden-Popper (RP) series $\text{Sr}_{n+1}\text{Ru}_n\text{O}_{3n+1}$, ($n=1,2, \dots \infty$) are shown in Figure 1.5 [23, 24]. As previously stated, these crystal structures can be derived from the ideal perovskite structure denoted by ABO_3 . The main difference between those ruthenates and manganese oxides is that these are layered perovskite structures characterized by the number of RuO_6 octahedron interlinked by the sharing of apical oxygens between Sr-O planes.

This class of materials is known to display a vast array of physical phenomena such as metal-insulator transition (MIT), exotic superconductivity, metamagnetic transitions, and quantum criticality. For example, the $n = 1$ monolayer system Sr_2RuO_4 , is a strongly two-dimensional (2D) system that exhibits characteristics of both Fermi liquid behavior above 1.5 K and of unconventional spin-triplet superconductivity below 1.5 K [25, 26]. The three-dimensional (3D) compound, SrRuO_3 ($n = \infty$), is a pseudo-cubic itinerant ferromagnet with a Curie temperature (T_C) of 160 K [27], which displays characteristics of non-Fermi liquid behavior [28].

In order to understand the complexity of these systems, one has to keep in mind 1) the electronic structure, and 2) the fact that the Ru site is located inside the RuO_6 octahedron, thus exposed to the crystal field. The ruthenium ions are in a Ru^{4+} oxidation state with four electrons occupying the $4d$ orbitals. According to Hund's Rules, three of the electrons would be found in the lower lying t_{2g} orbitals while one in the e_g , thus corresponding to the high spin state. This is however not the case; the electron configuration results in the low-spin state with $S = 1$ and all four electrons occupying the lower lying t_{2g} orbitals. In contrast to the case of manganites, this resulting electron configuration is due to the large value of the crystal field in ruthenate systems

(~ 4 eV) which is able to easily overcome Hund's Rule coupling of (~ 1 eV). The structural distortion of the octahedral environment strongly affects the electronic structure of these materials; tilt, rotation, and elongation (or compression) will determine the energy splitting among the t_{2g} levels. Figure 1.6 (from left to right) depicts the splitting of energy levels of the $4d$ orbitals in the presence of a cubic crystal field, and a tetragonal crystal field with both elongated and contracted octahedron along the z -axis, respectively.

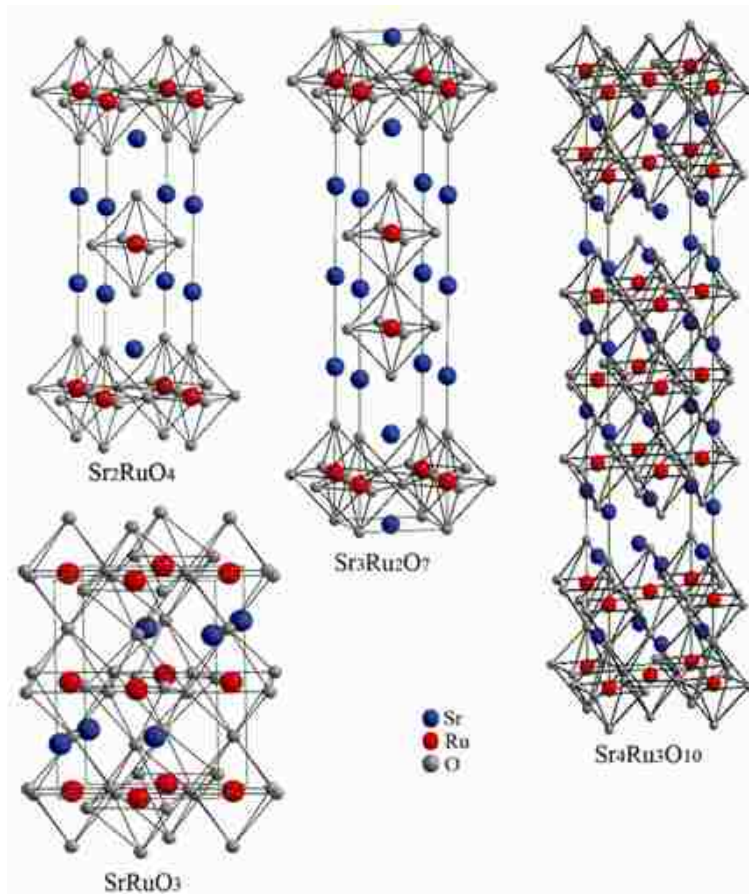


FIGURE 1.5 Crystal structures of the Ruddlesden-Popper (RP) series of layered perovskites, $\text{Sr}_{n+1}\text{Ru}_n\text{O}_{3n+1}$ ($n = 1, 2, 3, \dots \infty$). Along the diagonal from left to right the crystal structures are shown for the $n = 1, 2,$ and 3 members of the series. The $n = \infty$ member of the series, SrRuO_3 , is shown on the bottom left corner.

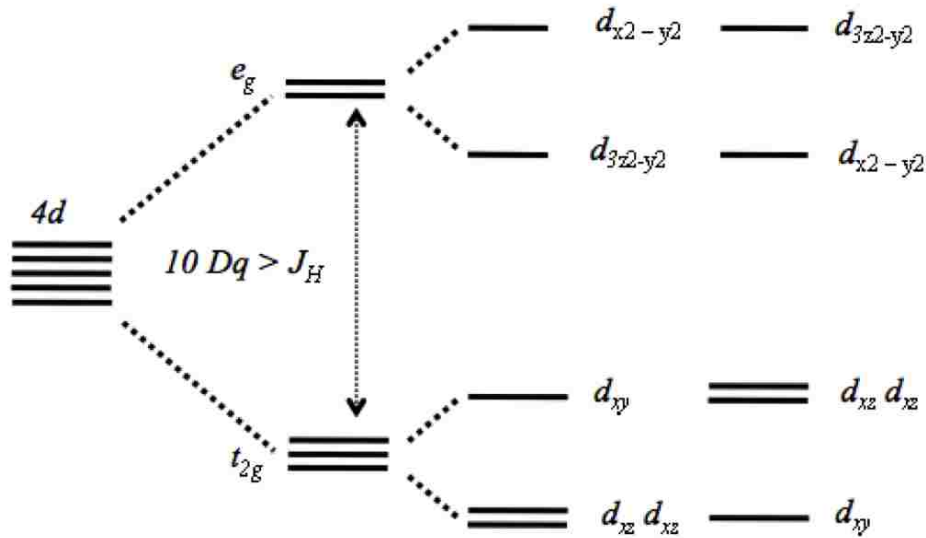


FIGURE 1.6 Schematic representations of the energy levels of the $4d$ -orbitals. From left to right: $4d$ orbital levels in the presence of a cubic crystal field, a tetragonal crystal field with elongated octahedron, and a tetragonal crystal field with contracted octahedron along the z -axis. Figure adapted from [15].

Properties of Pure and Mn-substituted $\text{Sr}_3\text{Ru}_2\text{O}_7$

During the last decade, the bilayered compound, $\text{Sr}_3\text{Ru}_2\text{O}_7$ ($n = 2$), has attracted quite a bit of attention due to the observation of a metamagnetic quantum critical end point [4]. In this system, several aspects of the metamagnetic transition are not clear; namely, the role of critical fluctuations and the splitting of the metamagnetic transition that is accompanied by an electronic nematic state. Most of the magnetic properties of this system are in qualitative agreement with the Stoner picture of itinerant electron magnetism [29 – 32]. As a result, they are tightly bound to the topology of the Fermi Surface (FS) sheets. In SRO 327, the electronic structure has been studied by ARPES [33]. Results show that all members of the series have Fermi surfaces that show a strong $4d_{xy}$ and $4d_{xz,yz}$ orbital character and evidence of O- $2p$ hybridization as well as a

$d_{x^2-y^2}$ character, which is indicative of e_g occupation. Typically, the $4d_{xy}$ is involved in the quasi two-dimensional sheet of the Fermi surface while the $4d_{yz}$ and $4d_{xz}$ are associated with the quasi one-dimensional sheet of FS. ARPES results indicate that the FS sheets that have a significant d_{xy} character might play a crucial role in the metamagnetic transition since they display a high density of states near the Fermi surface including van Hove singularities. This scenario depicting d_{xy} character is qualitatively similar to that given by Binz and Sigrist for the model of the metamagnetic transition [34]. $\text{Sr}_3\text{Ru}_2\text{O}_7$ has been found to exhibit metamagnetism when exposed to magnetic fields aligned along both ab and c planes for magnetic field values between 5 and 6 T and 7.8 T, respectively. Furthermore, critical fluctuations have also been reported for temperatures greater than 1.8 K [35]. In-depth studies of the low-temperature transport properties (for magnetic field orientations along c axis) [36, 37] show that below 1.2 K the metamagnetic transition splits into two first-order transitions, thus indicating the boundaries of a new phase that masks the quantum critical point. In this regime, a strong in-plane anisotropic resistivity has been found [8] with no evidence of structural phase transitions or magnetic domains. As a result this new phase has been referred to as an electronic nematic phase.

In the low temperature regime, $\text{Sr}_3\text{Ru}_2\text{O}_7$ is metallic and paramagnetic [38]. It also displays Fermi liquid behavior below 10 K [35, 39]. The understanding of magnetism in this SRO 327 system has been rather illusive. For example, triple-axis neutron diffraction measurements by Huang and collaborators [40] show no evidence of either long/short-range AFM or FM ordering in the range of temperatures from 1.4 to 125 K, with an upper limit of $0.05\mu_B/\text{Ru-atom}$ for any possible ordered moment. In addition, neutron diffraction [41, 42] and NMR measurements [43] have independently reported strong magnetic fluctuations of both FM and AFM character in this system. Furthermore, an enhancement of the AFM fluctuations has been observed near the

critical field. This is in contrast to what should be expected from the Stoner picture of itinerant magnetism, namely, that the relevant excitations near the quantum critical point should be of ferromagnetic character instead (see for example [44]).

For systems such as this one, characterized by strong magnetic fluctuations, chemical substitution is a very useful tool; it has the effect of stabilizing such fluctuations through the establishment of magnetic ordering. Thus allowing for a glimpse at the nature of the magnetic interactions in the parent compound.

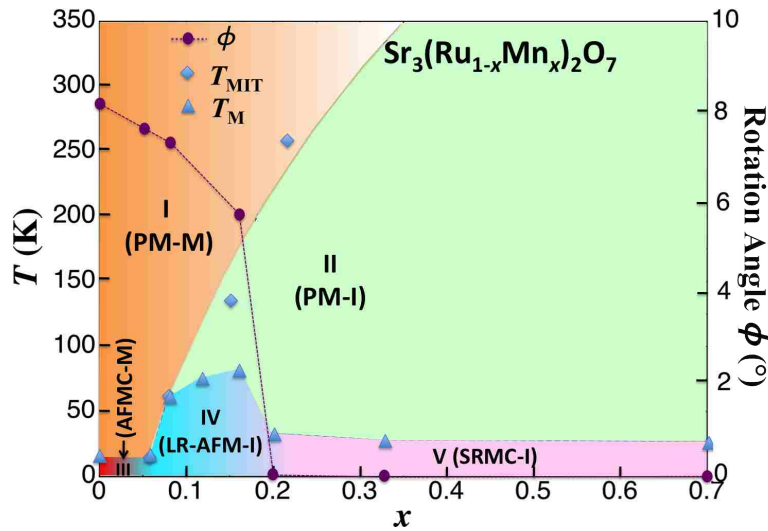


FIGURE 1.7 A schematic representation of the latest reported phase diagram for various substitution concentrations (x) of the $\text{Sr}_3(\text{Ru}_{1-x}\text{Mn}_x)_2\text{O}_7$ series. Region I is a paramagnetic metallic (PM-M) phase; II a paramagnetic insulating (PM-I) phase; III a metallic phase with AFM correlation (AFMC-M); and IV a long-range AFM insulating phase (LR-AFM-I). Region V is an insulating phase characterized by short-range magnetic correlations (SRMC-I). The right axis indicates the x dependence of the rotation angle ϕ of the (Ru/Mn) O_6 octahedron at 90 K [45].

Figure 1.7 displays the phase diagram of $\text{Sr}_3(\text{Ru}_{1-x}\text{Mn}_x)_2\text{O}_7$ constructed from measurements of macroscopic quantities such as the resistivity and magnetic susceptibility, reproduced from [45], with the right axis indicating the coupling dependence of the rotation of the (Ru/Mn) O_6 octahedron. It is clear from this phase diagram that there is a close connection between the

variation of electronic and magnetic properties and the change of the local structure in this compound, which is evident from the decrease in rotation angle of the (Ru/Mn)O₆ octahedra with increasing Mn concentration. It is interesting to see that a partial Mn substitution for Ru induces an insulating antiferromagnetic state above Mn concentrations as small as 5% [46]. Within this regime (i.e. the long range antiferromagnetic insulator ground state), many issues such as the nature of the metal-insulator transition and its interplay with magnetic correlations, and the complexity of the observed antiferromagnetic structure remain inconclusive [45, 47]. To this extend, the work on ruthenium oxides presented in this thesis encompasses a comprehensive neutron scattering study of the magnetic structure and dimensionality of the ordered parameter in the bilayered ruthenate Sr₃(Ru_{1-x}Mn_x)₂O₇ for Mn concentrations of 12.5 and 16%.

1.4.2 Manganese Oxides

Since the mid 1900s considerable attention has been directed to the mixed-valence manganese oxides R_{1-x}A_xMnO₃ (where *R* and *A* are rare- and alkaline-earth ions), known as manganites, after they were found to exhibit a dramatic decrease in electric resistance with the application of a magnetic field—referred to as the Colossal Magnetoresistance effect (CMR). This dramatic decrease in resistance in a magnetic field occurs at the Curie temperature, where there is also an insulator to metal transition at zero field. In these materials the effect of correlations among electrons play an important role and exhibits electronic complexity that arises from the strong interplay between charge, spin, and orbital degrees of freedom that results in a variety of competing ground states. This competition can lead to the emergence of novel phenomena like nano-scale phase separation, novel electronic soft phases, and colossal responses. The kinetic energy of the conduction electrons can be finely tuned in these perovskite manganite systems by judiciously adjusting their chemical composition. The latter is responsible for the richness of

their ground state; typical ground states include ferromagnetic (FM) metallic or insulators and antiferromagnetic (AF) charge-/spin-/ and orbitally-ordered (CO-SO-OO) insulators (for a review consult [16]).

Basic Properties, Phase Diagrams, and the Colossal Magnetoresistance Effect in Manganites

Figures 1.8 and 1.9 display the phase diagrams and physical properties of $\text{Pr}_{1-x}\text{Ca}_x\text{MnO}_3$ (PCMO) and $\text{La}_{1-x}\text{Ca}_x\text{MnO}_3$ (LCMO), respectively. The insulating behavior that dominates the composition range in these low-bandwidth (W) systems is typical due to the narrow bandwidth of the e_g electrons (note that for the truly low- W system PCMO, the sizes of Pr^{3+} and Ca^{2+} are almost identical ensuring in this way a negligible quenched disorder). This is in sharp contrast to $\text{La}_{1-x}\text{Sr}_x\text{MnO}_3$ (LSMO), a system that is considered to be truly large-bandwidth, whose phase diagram at higher dopant concentrations is characterized by a robust FM and AF metallic ground states [16].

As seen from the phase diagrams, these low- W systems are characterized by (CO-OO) phases over a wide range of doping concentrations that is stabilized near $x = 0.5$ hole doping. In fact, it is widely accepted today that the raw huge magnitude of the CMR effect in these compounds is the result of the strong competition between the FM metallic and CO-OO insulating states, mediated by the double-exchange (DE) interaction (see Figure 1.10), which promotes electric conduction and ferromagnetism in the FM metallic phase. This is a well-known mechanism (Figure 1.10 (a)), proposed originally by Zener in the 1950's and is characterized by the simultaneous movement of one electron from the O^{2-} to the Mn^{4+} ion and one from the left Mn^{3+} ion back to the O^{2-} [48]. Years later, it was shown by the work of Anderson and Hasegawa [49] that the effective electron hopping, between the p -oxygen and the

d -manganese orbital follows a cosine modulation given by $t_{pd} \propto \cos(\theta/2)$, where t denotes the hopping parameter and θ represents the angles between the spins of the nearest-neighbors (see Figure 1.10 (b) and (c)). The modulation of the hopping parameter, as described by the $\cos(\theta/2)$ yields a maximum hopping for cases of $\theta = 0$ while it vanishes for $\theta = \pi$, thus corresponding to FM and AF backgrounds, respectively.

In the phase diagram of PCMO (Figure 1.8 (a)), the CO-OO state is stabilized in a broad density region of dopant concentration ($0.3 < x < 0.75$); notice that an AF insulating ground state (instead of FM metallic as in the intermediate- W system LCMO (refer to Figure 1.9)) precedes this phase. In this system, the effect of an applied magnetic field leads to the highest drop in resistivity observed in perovskite manganites. Figure 1.9 (b) shows the temperature dependence of the resistivity under a relatively small-applied magnetic field of a few Teslas (small in typical electronic units).

Figure 1.9 (a) and (b) display the phase diagram and physical properties of the intermediate- W system LCMO. As in the case of PCMO, the phase diagram also displays a wide range of concentrations ($0.5 < x < 0.75$) in which the CO-OO state is stabilized. The ferromagnetic insulating (FI) ground state, however, is followed by a ferromagnetic metallic (FM) state. The magnetization, resistivity and magnetoresistance (MR) as a function of temperature are shown in Figure 1.9 (b). To note in the latter, is the dramatic decrease in resistivity upon the application of a magnetic field leading to a large MR effect $\sim 80\%$. All of which occur at the FM transition temperature shown in the magnetization plot.

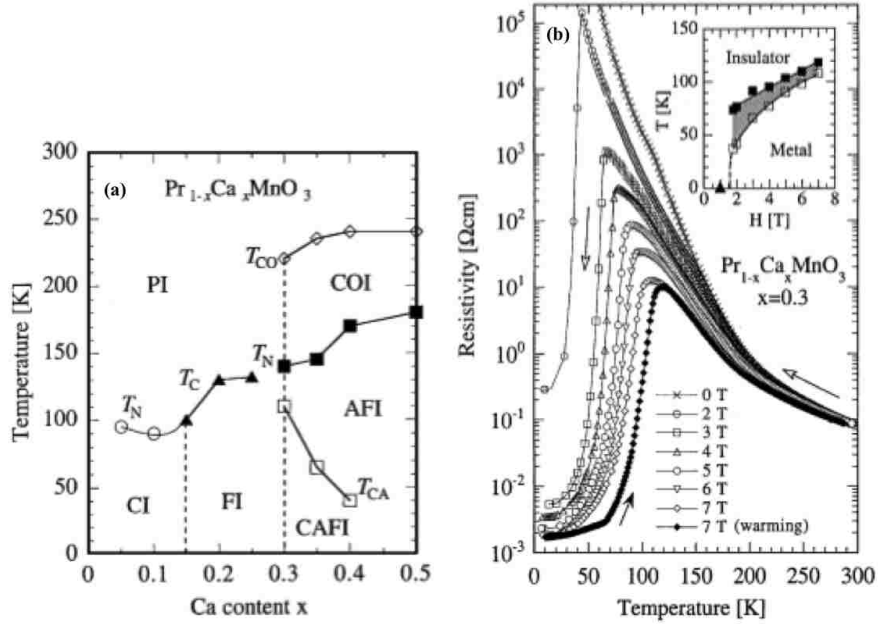


FIGURE 1.8 Phase diagram as a function of temperature and Ca content and temperature dependence of the resistivity under various applied magnetic fields for the perovskite manganite $\text{Pr}_{1-x}\text{Ca}_x\text{MnO}_3$. (a) In the phase diagram, starting from low- to high-hole doping concentrations: CI, PI, FI denote the canted insulating, paramagnetic insulating, and ferromagnetic insulating states, respectively. From Ca concentrations in the regime of 0.3-0.5 a coexistence of AFI (antiferromagnetic insulating state), COI (charge/orbital ordered insulating phase) and CAFI (canted antiferromagnetic insulating state) is observed. (b) Shows the temperature dependence of the resistivity at $x = 0.3$ under the application of magnetic fields with the inset showing a plot of the temperature vs. magnetic field displaying the shaded area as the hysteresis region [50].

As shown in Figure 1.11, the $3d$ transition-metal atom (Mn^{3+}) is exposed to the oxygen environment, which causes the splitting of the d -levels. In manganites, the strength of the crystal field splitting (~ 2 eV) is much smaller than Hund's rule coupling ($J_H = 4$ eV), thus the system adopts a high-spin configuration with three electrons occupying the t_{2g} orbitals and one the e_g orbital. The right side of the figure, depicts the lifting of the e_g degeneracy as a consequence of the Jahn-Teller effect, where the splitting of the e_g levels is in the range of 0.6 eV.

By increasing the hole doping concentration in the pure compound, ABO_3 , the physics becomes even more complex for the doped manganites systems studied in this investigation

since an additional degree of freedom—charge—is introduced by doping with divalent cations. Since the charge must remain neutral, manganese must now exist in two valence states: $\text{Mn}^{3+}/\text{Mn}^{4+}$. This lattice-distorting chemical doping procedure, establishes the presence of quenched disorder in these manganite systems, which is responsible for the existence of nanoscale mixture of phases, inhomogeneity, and unusual phase coexistence in the ground state of these systems [17, 19, 22, 53].

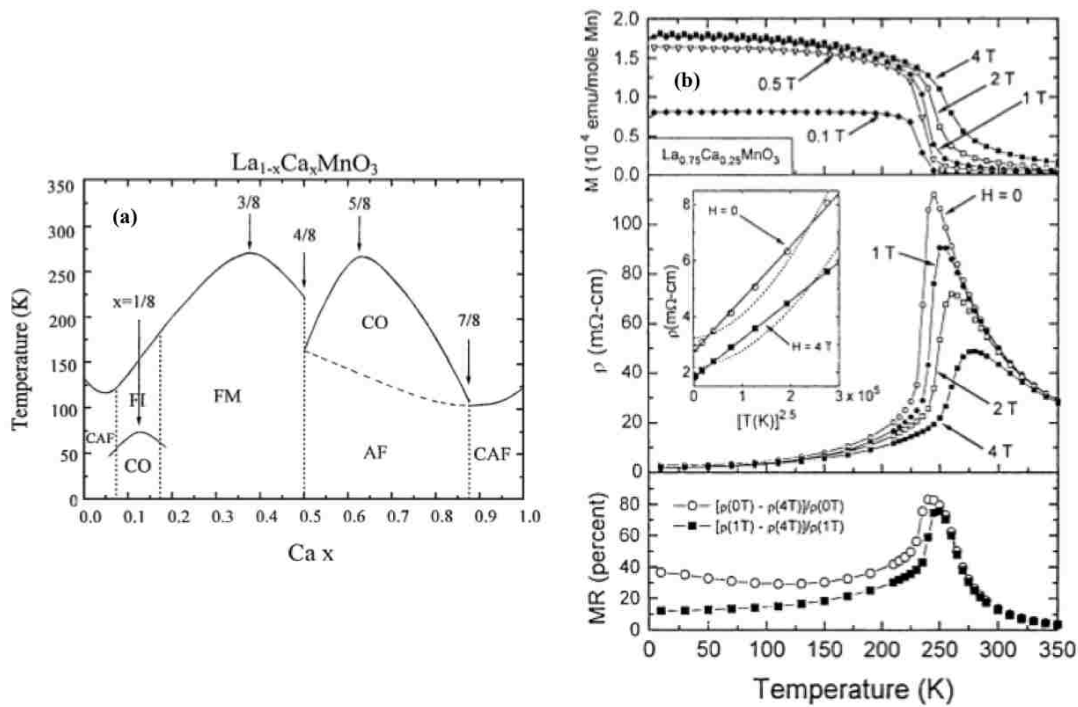


FIGURE 1.9 Phase diagram as a function of temperature and Ca concentration and measurement of microscopic quantities for the perovskite manganite $\text{La}_{1-x}\text{Ca}_x\text{MnO}_3$. (a) Shows the phase diagram of the CMR manganite $\text{La}_{1-x}\text{Ca}_x\text{MnO}_3$ constructed from physical macroscopic measurements [51]. Abbreviations for phases are given in diagram: FI (ferromagnetic insulator), FM (ferromagnetic metal), AF (antiferromagnetism), CO (charge/orbital ordering), CAF (canted antiferromagnetic). (b) From top to bottom: Magnetization, resistivity, and Magnetoresistance (MR) for $\text{La}_{0.75}\text{Ca}_{0.25}\text{MnO}_3$. The inset is resistivity, ρ at low- T . Taken from [52].

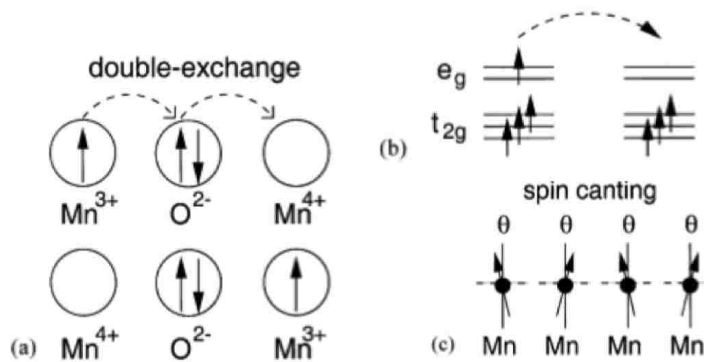


FIGURE 1.10 Schematic representation of the Double Exchange mechanism. (a) Diagram depicts the movement of electrons between the O²⁻ and the Mn⁴⁺ [see txt]. (b) The mobility for the e_g electrons is maximized for cases in which the localized spins are fully polarized. (c) A representation of spin-canted states, which are presumed to be a mixture of FM-AF states. Image adapted from [16].

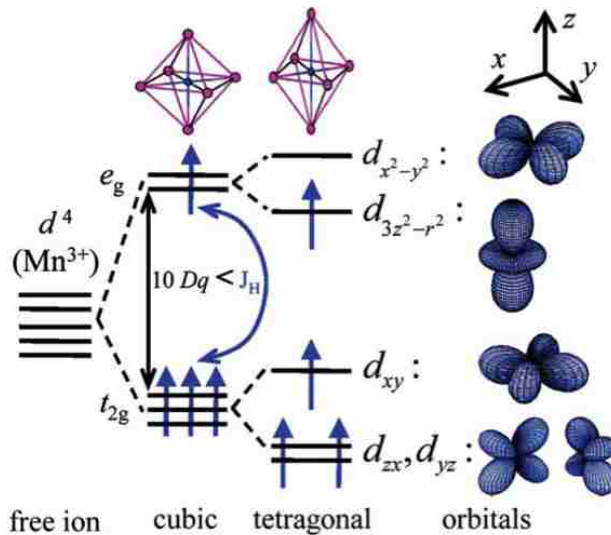


FIGURE 1.11 Schematic representations of the energy levels of the 3d-orbitals in manganese oxide systems. The left side depicts the high spin state for a free MnO³⁺ ion. In the cubic environment, the 3d levels of Mn split as shown with all the spins parallel and three electrons in the lower t_{2g} state and one in the e_g state. The system can lower its energy by removing the degeneracy of the e_g state and thus undergoing a geometric distortion of the octahedra known as the Jahn-Teller effect. The right side of the figure shows the atomic orbitals associated with each of the energy levels [19].

Despite many years of intensive studies, many aspects of the mixed-phase phenomenology that characterizes these complex manganite systems as well as the nature of the ground states and their role in the CMR effect remain inconclusive. The main motivation behind our investigation stems from the fact that manganites reveal a vast array of interesting physical phenomena that could potentially be critical to the understanding of other important systems (e.g. ruthenates). Thus, we believe the study of perovskite manganites deserves a special place in the physics of correlated electron systems. To this extent, the work on manganites presented in this investigation consists of 1) an elastic scattering study that investigates the phase-separation in the CO-OO state of $\text{Pr}_{1-x}\text{Ca}_x\text{MnO}_3$ for various hole-doping concentrations, and 2) an $\text{La}_{1-x}\text{Ca}_x\text{MnO}_3$ ($x=0.20$) inelastic neutron scattering investigation of the nature of the FM insulating ground state that precedes the FM metallic ground state in which CMR is observed.

1.5 Neutron Scattering as an Experimental Condensed Matter Physics Probe

How to study experimentally the various complex ordering phenomena discussed in previous sections? It is clear that we need a probe that 1) provides microscopic information on the structure and dynamics in solids and 2) interacts with unpaired spins in the system. It is in this context that neutrons have become a powerful probe of the structure and dynamics of materials.

1.5.1 Why Neutrons?

Their lack of electric charge allows neutrons not only to penetrate deeply into the target, but also to be at a close proximity to the nuclei (interacting mainly through the strong nuclear force: 1 fm = 10^{-15} meters) thus allowing for the study of the structural properties of solids. This is a crucial property that sets neutrons apart from other elastic scattering techniques such as X-Rays or electron diffraction, since these two interact with the electron cloud in solids; with electrons the

interaction is electrostatic and with X-Rays is electromagnetic. Both of these interactions are strong, thus preventing deep penetrations of the beam into the material, yielding low intensity diffraction peaks for very light atoms (e.g. Oxygen) as in the case of X-rays. This is in sharp contrast with the very short-range nuclear force which 1) allows the neutron to travel large distances inside the solids without being scattered or absorbed, since as far as the neutron is concerned, solids are not very dense and 2) facilitates the detection of light atoms in the presence of heavier ones since neutron scattering lengths are characterized by an irregular, element specific distribution unlike X-Rays, and 3) makes neutrons more suitable for precise determinations of atomic displacement parameters (e.g. temperature) since the diffracted intensity for X-Rays decreases rapidly for large scattering angles while for neutrons it is independent of the scattering angle due to the fact that the neutron's wavelength (1- 3 Å) is much larger than the nucleus and comparable to interatomic distances in solids [54, 55].

The neutron also has a magnetic moment ($\mu_n = 1.91 \mu_N$, in units of the nuclear magneton μ_N) that interacts with the spins of unpaired electrons through the magnetic dipole interaction. The latter reveals the periodicity of the magnetic unit cell (through additional peaks in the diffraction pattern) and both the magnitude and direction of the ordered magnetic moment. In fact, no other microscopic technique is able to provide such detailed microscopic information about magnetism in solids as magnetic neutron scattering does; physically speaking, the neutron is able to both establish and detect the response of a frequency- and wave vector-dependent magnetic field in the scattering sample [56].

The energy range (5-100 meV) of thermal neutrons is ideal for the study of the dynamics of materials; their energy is comparable to that of the order of the energy of excitations resulting from complex ordering of spin, charge, and orbital such as phonons and magnons, etc. Inelastic

neutron scattering is the most precise experimental technique that is able to measure the dispersion relations $\hbar\omega(\mathbf{q})$ of such excitations at any pre-determined point in reciprocal space (i.e. throughout the Brillouin zone), since it permits the controlled access to nearly any part of energy and momentum space [56].

There is however, one major disadvantage to the experimental technique of neutron scattering; it is a signal-limited technique. The latter results from a combination of the fact that 1) neutron is a weakly interacting particle with high penetrating power and thus is weakly scattered, and 2) that available neutron beams inherently have low fluxes ($\sim 10^7$ neutrons per second per square millimeter compared to 10^{18} photons per second per square millimeter at an X-ray synchrotron radiation for the same bandwidth of energy). As a consequence, rather large amounts of single crystal samples—in the order of grams—are usually required for scattering experiments. The latter might be a challenging obstacle to overcome, specially when investigating a newly synthesized material as have done in Chapter 4. Clever ways to align and mount many samples will be required in order to improve the signal. On the other hand, these shortcomings have been a major drive in the design of numerous neutron scattering instruments specifically devoted to a certain scattering process [54]. For instance, in this work we have used a total of 7 instruments that are categorized under two main types developed to tackle the specific scattering processes of diffraction and inelastic neutron scattering (see Chapter 3).

It is appropriate to mention as well—for those unfamiliar with the neutron scattering technique—that in spite of its unique advantages it is a technique that must be complemented by others if the aim is to provide full characterization of the system. For example, structure determination from polycrystalline materials is done by a simultaneous refinement of both neutron and x-ray powder diffraction spectra, since the contrast mechanisms differ for the two

probes. Other experimental techniques such as scanning tunneling spectroscopy (STM), transmission electron microscopy (TEM), photoemission, nuclear magnetic resonance (NMR) and muon spin relaxation provide complementary information on the specific physics being investigated.

Taking advantage of neutron's unique properties and instruments designed for specific scattering processes, elastic, inelastic, and polarized neutron scattering experiments can be conducted on a specimen in order to reveal its nuclear, magnetic, and dynamical properties. More specifically, elastic scattering (no energy analysis) can be used to determine the time-averaged nuclear and magnetic structures. Quasielastic diffuse scattering gives information on short-range correlations and fluctuations of nuclear and magnetic origin, while inelastic scattering yields information about the relevant interactions from which complex phenomena originate. In addition, polarized experiments are used to distinguish between the magnetic and nonmagnetic scattering. It is important to mention that neutron diffraction can also give information about charge and orbital order. These types of ordering cannot be directly measured with neutrons, but rather indirectly due to the changes they cause in the system. Charge order is detected through the changes in the transition metal-oxygen bond by the so-called *bond valence sum* while orbital order is 'seen' through the distortion it causes in the lattice.

Chapter 2

Neutron Scattering

This chapter is intended to familiarize the reader with the basic principles in experimental neutron scattering. It will briefly state basic properties of neutrons followed by the numerical values for velocity, energy, and wavelength of the neutron. The remainder of the chapter presents the reader with some of the most useful formulas for interpreting experimental measurements on crystalline solids. If further details are needed, the interested reader is urged to consult several excellent books for more rigorous derivations [55, 57 – 59].

2.1 Basic Properties of Neutrons

For neutron scattering experiments, only thermal neutrons ($5 \text{ meV} \leq E \leq 100 \text{ meV}$) are of interest.

Table 2.1 shows the basic properties of neutrons.

TABLE 2.1 Basic Properties of Neutrons

<i>Mass</i> $m = 1.675 \times 10^{-27} \text{ kg}$
<i>Charge</i> 0
<i>Spin</i> $\frac{1}{2}$
<i>Magnetic dipole moment</i> $\mu_n = -1.93 \mu_N$

For these range of energies, the velocity spectrum of thermal neutrons follows that of the Maxwellian speed distribution for a molecule of dilute gas in thermal equilibrium

$$\phi(v) \propto v^3 e^{-\frac{1}{2} m v^2 / k_B T}, \quad (2.1)$$

where $\phi(v)dv$ is the number of neutrons through a unit area per second with velocities of $v + dv$, m is the mass of the neutron, T is the temperature of the neutrons emerging from the moderator, and $k_B = 1.381 \times 10^{-23} \text{ J/K}$ is the Boltzmann constant. Recall that the energy of the neutrons, at a given temperature, T , is conventionally expressed as

$$E = k_B T = \frac{1}{2} m v^2, \quad (2.2)$$

while the de Broglie wavelength of a neutron with velocity v is given by

$$\lambda = \frac{h}{m v}, \quad (2.3)$$

with $h = 6.626 \times 10^{-34} \text{ J s}$ the Plank constant ($\hbar = h/2\pi$). Furthermore, the magnitude of the wavevector \mathbf{k} in the direction of v and the momentum of the neutron are defined as

$$k = \frac{2\pi}{\lambda}, \quad (2.4)$$

and

$$\mathbf{p} = \hbar \mathbf{k}. \quad (2.5)$$

We can now combine equations (2.2) – (2.5) into (2.2) and obtain the well known expression for energy:

$$E = k_B T = \frac{1}{2} m v^2 = \frac{\hbar^2}{2m\lambda} = \frac{\hbar^2 k^2}{2m}. \quad (2.6)$$

If we now insert the values of all the elementary constants in the above expression for energy, we arrive at the following useful relations between the energy (meV), wavelength (Å), wavevector (Å⁻¹), velocity (km/s), and temperature (Kelvin) for thermal neutrons with units of:

$$E = 0.08617 \cdot T = 5.227 \cdot v^2 = 81.81 \cdot \frac{1}{\lambda^2} = 2.072 \cdot k^2. \quad (2.7)$$

For the purpose of completeness we also provide useful conversions between the units of energy used in neutron scattering (meV) and those used in other spectroscopic techniques such as wavenumbers in cm⁻¹ and tetrahertz (THz):

$$1\text{meV} = 0.242\text{ THz} = 8.07\text{ cm}^{-1} = 11.6\text{ K} = 17.3\text{ T}, \quad (2.8)$$

where the last two conversions to temperature (kelvin) and magnetic field (T = Tesla) have been provided as well. The standard value taken for velocity for thermal neutrons is that of $v = 2.20\text{ km s}^{-1}$. Using the above relations, we can then obtain the standard values for the energy, wavelength, absorption cross-section ($1/v$), temperature and magnitude of the wavevector. These are shown in Table 2.2.

TABLE 2.2 Standard Values for Thermal Neutrons

$v = 2.20 \frac{\text{km}}{\text{s}}$	$\frac{1}{v} = 455 \frac{\mu\text{s}}{\text{m}}$
$E = 25.3\text{meV}$	$T = 293\text{K}$
$\lambda = 1.798\text{ \AA}$	$k = 3.49 * 10^{10}\text{ m}^{-1}$

2.2 Basic Principles of Neutron Scattering

The aim of a neutron scattering experiment is the determination of the probability that an incident neutron on a sample with initial wave vector \mathbf{k} is scattered into a final state with wave vector \mathbf{k}' . As with any scattering process, the intensity of the scattered neutrons is a function of the momentum transfer

$$\hbar\mathbf{Q} = \hbar(\mathbf{k} - \mathbf{k}') = \hbar\boldsymbol{\tau}, \quad (2.9)$$

where \mathbf{Q} and $\boldsymbol{\tau}$ are defined as the scattering and reciprocal lattice vectors³, respectively. Thus, the magnitude of \mathbf{Q} and corresponding energy transfer are given by

$$|\mathbf{Q}| = k^2 + k'^2 - 2kk' \cos \theta, \quad (2.10)$$

and

$$\hbar\omega = \frac{\hbar^2}{2m}(k^2 - k'^2). \quad (2.11)$$

Just like in any scattering process, both the momentum and energy are the conserved quantities. Thus, equations (2.9) and (2.11) are used in the scattering experiment to infer the momentum and energy transferred to the sample by measuring the properties of the incident and final neutron beams.

2.2.1 Elastic Scattering

In order to understand both diffraction and the scattering process, a representation of reciprocal space is required. Figure 2.1 shows the schematic representation of the reciprocal lattice for a two-dimensional crystalline solid. The circle is commonly referred to as the Ewald circle in which the dots represent the crystal lattice.

Coherent elastic scattering (i.e. $|\mathbf{k}| = |\mathbf{k}'| = k$ and $\hbar\omega = 0$) or Bragg diffraction occurs when the Bragg condition is satisfied. Such is the case depicted in Figure 2.1 with the circle of radius k that passes through two points, with one of these points being at the origin of the reciprocal space where

³ Note also that the symbol \mathbf{G} , depending on the reference being consulted, sometimes denotes the reciprocal lattice vector such that one might also find expression (2.9) written as $\hbar\mathbf{Q} = \hbar(\mathbf{k} - \mathbf{k}') = \hbar\mathbf{G}$.

$$\mathbf{Q} = \boldsymbol{\tau} = \mathbf{k} - \mathbf{k}', \quad (2.12)$$

where \hbar has been dropped for simplicity. From the above equation, we can derive Bragg's law by making use of equation (2.10), thus obtaining

$$|\mathbf{Q}| = |\boldsymbol{\tau}| = 2|\mathbf{k}|\sin\theta_S, \quad (2.13)$$

where $2\theta_S$ is defined as the Bragg angle, or as that one between the incident and final neutron beam. Recalling that the magnitude of the reciprocal lattice vector is that of $|\boldsymbol{\tau}| = 2\pi/d$, where d is used to denote the inter-planar spacing in crystalline solids, we arrive at the more common expression for Bragg's law:

$$\lambda = 2d\sin\theta_S. \quad (2.14)$$

In a typical neutron diffraction experiment any point in reciprocal space can be measured—as long as the instrument allows it—by choosing the appropriate values of \mathbf{k} , $2\theta_S$, and the orientation of the sample relative to the initial wavevector \mathbf{k} . Adjusting the angle $2\theta_S$ between the initial and final wavevectors and rotating the sample control both the magnitude and orientation of \mathbf{Q} within the reciprocal lattice, respectively.

In addition to the interaction of neutrons with atomic nuclei, there is also another one that results from the fact that a neutron has a magnetic moment. Thus, the magnetically ordered spins in a sample gives rise to Bragg diffraction of neutrons in the same manner as the nuclear interaction described above. Thus, the neutron experiences a force of magnetic origin as it approaches a fellow magnetic particle. This magnetic interaction, however, has a dipolar nature (much like that of two bar magnets when brought close together). In fact for the case of ferromagnets, both types of Bragg peaks occur at the same value of \mathbf{Q} . In the case of antiferromagnets the nuclear and magnetic Bragg peaks are usually at different values of \mathbf{Q} ,

reflecting in this way the differences between the nuclear lattice and the antiferromagnetic sub lattice.

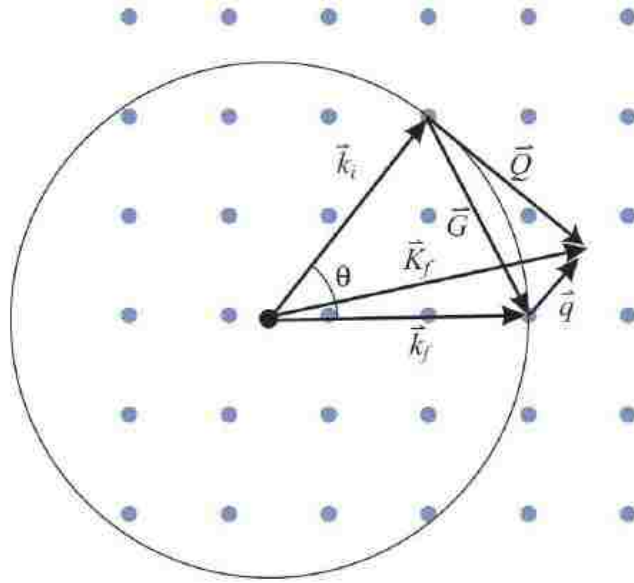


FIGURE 2.1 The Ewald circle in two-dimensions representing the reciprocal space. The gray dots represent the reciprocal lattice for a two-dimensional crystalline solid while the vector representation depicts the elastic and inelastic scattering process. \mathbf{G} denotes the reciprocal lattice vector while \mathbf{q} represents the momentum transfer within the first Brillouin zone [57].

2.2.2 Inelastic Scattering

In the case of inelastic neutron scattering, we have $|\mathbf{k}| \neq |\mathbf{k}'|$ because in this case energy is either being transferred to or from the sample. From Figure 2.1 we can see that we can further decompose the scattering vector into

$$\mathbf{Q} = \boldsymbol{\tau} + \mathbf{q}. \quad (2.15)$$

That is, into a form where the scattering vector does not coincide with the reciprocal lattice vector as such was the condition for elastic scattering. In an experiment this can be accomplished by fixing the value of \mathbf{k} and allowing \mathbf{k}' to vary. This set up allows for \mathbf{Q} and \mathbf{q} to be kept constant while both the scattering angle and the relative orientation of the crystal with respect to

\mathbf{k} are changed. In instances for which $\mathbf{k} < \mathbf{k}'$ and $\hbar\omega < 0$, the sample gives up quantum energy to the emerging neutron beam. This is referred to as anti-Stokes scattering in which an excitation is annihilated, resulting in a gain of neutron energy. On the other hand, for cases in which $\mathbf{k} > \mathbf{k}'$ and $\hbar\omega > 0$ energy is transferred to the sample (Stokes scattering) and an excitation is created. In equation (2.15), \mathbf{q} represents the wavevector of the specific elementary excitation. Phonons are an example of such excitations resulting from an exchange of energy between neutrons and the lattice, which causes a superposition of waves to move through the lattice. The magnetic analogue of phonons—referred to as magnons—result from an exchange of energy between neutrons and the magnetic moments in the sample. However, because the magnetic interaction is dipolar in nature, the resulting scattering is not isotropic as in the nuclear case—i.e. only the component of the sample's magnetization that is perpendicular to \mathbf{Q} will scatter neutrons. This is the basic principle behind polarization analysis (see Chapter 3), a technique that is used to help determine the directions of electronic moments as well as to distinguish between phonons and magnons.

2.3 Mathematical Foundations of Neutron Scattering: Van Hove Formalism

The majority of neutron spectroscopic techniques can be reduced to a measurement of the *partial differential scattering cross section*, given by

$$d^2\sigma/d\Omega dE', \quad (2.16)$$

which is defined to be the total number of neutrons scattered per second by the sample into a unit of solid angle $d\Omega$ in the direction θ and ϕ with a final energy between E' and $E' + dE'$. It is normalized by the neutron flux incident on the sample Φ_0 (with units of neutrons/sec/cm²) such that the final units are of area/(solid angle)/energy. Figure 2.2 places all of the above quantities

in perspective; it depicts the cross section $d^2\sigma/d\Omega dE'$ for a specific transition of the scattering system from one of its quantum states to another. Such expression contains all the details of the individuals and collective motions of the atoms, molecules, and/or of any atomic magnetic moment that comprises the sample.

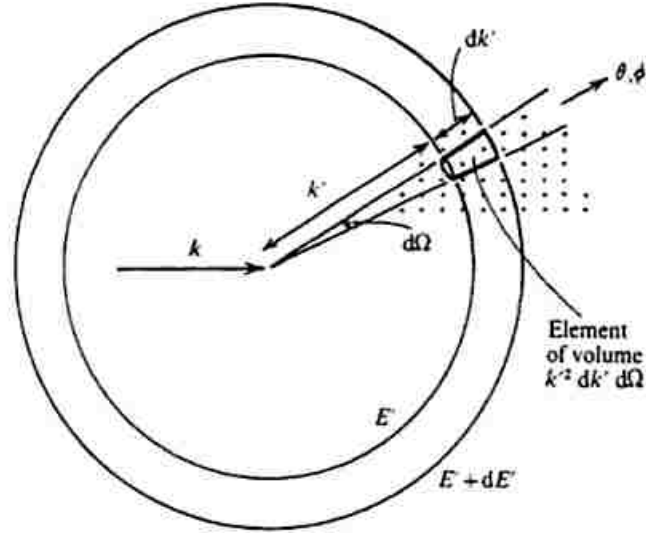


FIGURE 2.2 Geometry for scattering experiments. The components involved in the measurement of the partial differential scattering cross section in a neutron scattering experiment are shown, see text for detailed description [57].

Going back to equation 2.16, we see that by integrating over all the energies, one obtains the *differential cross-section*, represented by.

$$d\sigma/d\Omega. \tag{2.17}$$

This is what is measured in a diffraction experiment thus it yields the time-averaged (equilibrium) position of all the nuclei in the sample. Integrating once more over the solid angle (all directions) we obtain the *total scattering cross section*,

$$\sigma_{tot}, \tag{2.18}$$

which gives the scattering strength of the sample (units: 1 barn = 10^{-28} m²) and thus represents the unnormalized probability that an incident neutron will be scattered.

2.3.1 Fermi's Golden Rule and the Born Approximation: The Master Formula

We continue here from the above section and arrive at the final expression for the *partial differential scattering cross section*. For an in-depth derivation of this result the reader can consult, for example, reference [57] while a more general derivation can be found on references [56, 60].

It is appropriate to now define a coordinate system (see Figure 2.3) in which the number of nuclei in the scattering sample is denoted by N and the position vector of the j^{th} nucleus and the neutron are defined by \mathbf{R}_j ($j = 1 \dots N$) and \mathbf{r} , respectively.

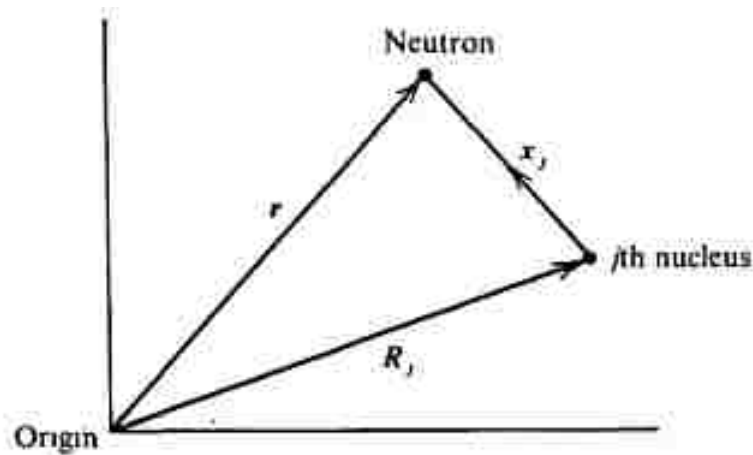


FIGURE 2.3 Coordinate system with the origin set at some arbitrary point in the scattering system. Shown are the position vector of the neutron and that of the j^{th} nucleus [57].

In order to derive a general expression for the observed intensity measured in a neutron scattering experiment Van Hove used a fundamental result in quantum mechanics known as

Fermi's Golden rule. The latter simply uses Fermi's observation that the interaction between neutron and nucleus could be replaced by an effective (much weaker) potential. This pseudo-potential allows the neutron to act as a very weak perturbation to the system, making it a perfect candidate for the perturbation expansion derived by Max Born. Thus while the scattered neutron causes a transition from one quantum state to another, it does not modify the nature of the states themselves. Thus, starting from 2.17 and using Fermi's golden rule, we have

$$\left(\frac{d\sigma}{d\Omega}\right)_{\lambda\rightarrow\lambda'} = \frac{1}{\Phi} \frac{1}{d\Omega} \sum_{\mathbf{k}' \text{ in } d\Omega} W_{\mathbf{k},\lambda\rightarrow\mathbf{k}',\lambda'}, \quad (2.19)$$

where the sum for a specific transition from one initial quantum state to another is defined as:

$$\sum_{\mathbf{k}' \text{ in } d\Omega} W_{\mathbf{k},\lambda\rightarrow\mathbf{k}',\lambda'} = \frac{2\pi}{\hbar} \rho_{\mathbf{k}'} |\langle \mathbf{k}' \lambda' | V | \mathbf{k} \lambda \rangle|^2. \quad (2.20)$$

In (2.19) and (2.20) the sum is taken over all values of the final neutron wavevector that lie inside the solid angle $d\Omega$ in the direction of θ, ϕ . With $W_{\mathbf{k},\lambda\rightarrow\mathbf{k}',\lambda'}$ (see Figure 2.2), representing the number of transitions per second from an initial state denoted by \mathbf{k}, λ to a final state \mathbf{k}', λ' . All normalized by the flux Φ of incident neutrons. In expression (2.20), the value of $\rho_{\mathbf{k}}$ (see Figure 2.2) is the number of momentum states in $d\Omega$ per unit energy range (between E' and $E' + dE'$) for neutrons with a final wavevector of \mathbf{k}' . Initially (for simplicity, can be easily generalized to magnetism see, for example, [57]) the state of the neutron is solely dependent on its momentum, thus an incoming neutron is defined with a wavevector \mathbf{k} and characterized by a specific λ . Let the wave function of the neutron and that of the scattering system be represented by $\psi_{\mathbf{k}}$ and $\chi_{\mathbf{k}}$, respectively. Furthermore, suppose the system interacts with a potential V and is scattered with a

characteristic wavevector of \mathbf{k}' , where the final state of the scattering system is denoted by λ' .

Thus, we are now in a position to write explicitly the matrix element in (2.20):

$$\langle \mathbf{k}'\lambda' | V | \mathbf{k}\lambda \rangle = \int \psi_{\mathbf{k}'}^* \chi_{\lambda'}^* V \psi_{\mathbf{k}} \chi_{\lambda} d\mathbf{R} d\mathbf{r}. \quad (2.21)$$

The integral is taken over all space for each of the $N+1$ variables that compose the scattering systems. Recall that number of nuclei in the scattering sample is denoted by N and the position vector of the j^{th} nucleus and the neutron are defined by $\mathbf{R}_j (j=1 \dots N)$ and \mathbf{r} , respectively. Thus $d\mathbf{R} = d\mathbf{R}_1 \dots d\mathbf{R}_N$ represents an element of volume for the j^{th} nucleus while $d\mathbf{r}$ is that of the neutron.

Inserting the appropriate values for $\rho_{\mathbf{k}}$, Φ , the neutron wave function $e^{i\mathbf{k}\cdot\mathbf{r}}$ (see, for example [57]) into (2.19) and (2.20), and finally including energy conservation in the form of a delta function), we are now ready to write down the general expression for the *partial differential scattering cross section* in a neutron scattering experiment (neglecting for the moment spin states), which is also known as the *master formula*:

$$\left(\frac{d^2\sigma}{d\Omega dE'} \right)_{\lambda \rightarrow \lambda'} = \frac{k'}{k} \left(\frac{m}{2\pi\hbar^2} \right)^2 |\langle \mathbf{k}'\lambda' | V | \mathbf{k}\lambda \rangle|^2 \delta(E_{\lambda'} - E_{\lambda} + E - E'). \quad (2.22)$$

The challenge lies, of course, in determining theoretical expressions for the different scattering processes. The matrix element, which represents the interaction operator between the neutron and sample, is specific to the scattering process. That is, it will take different forms when taking into account magnetic or nuclear interactions.

Example: Scattering of Neutrons by a Single Fixed Nucleus

As an example, let's consider neutron scattering from a nuclei at fixed position \mathbf{R}_l from the origin (see Figure 2.3). This is well approximated by the Fermi pseudo-potential

$$V(\mathbf{r}) = \frac{2\pi\hbar^2}{m} \sum_l b_l \delta(\mathbf{r} - \mathbf{R}_l). \quad (2.23)$$

In (2.23), b_l is the scattering length with magnitude on the order of 10^{-12} cm. For the case of the nuclear scattering cross section (2.22) the units amount to about 10^{-24} cm² or 1 barn. For the purposes of the neutron scattering experiments performed in this investigation, we will only consider the real part of the scattering length, which describes the energy-independent scattering. The imaginary part of b_l deals with the absorption of the neutron by the sample that occurs if the energy of the compound nucleus (neutron + nucleus) is of the same order of an excited nuclear state. The latter is rarely encountered in neutrons scattering, thus we will safely ignore it in our derivations.

Because the effective neutron-nucleus interaction is weak, we evaluate the matrix element in (2.22) using the Born approximation. Treating the incident and scattering neutrons both as plane waves, the matrix element becomes:

$$\langle \mathbf{k}' \lambda' | V | \mathbf{k} \lambda \rangle = \left\langle \lambda' \left| \int d\mathbf{r} V(\mathbf{r}) e^{i\mathbf{Q}\cdot\mathbf{r}} \right| \lambda \right\rangle, \quad (2.24)$$

where the integral is to be taken over the entire volume of the scattering sample. It is relatively easy to show (consult [56]) that upon substituting (2.23) and (2.24) into (2.22) and using a couple of standard tricks Van Hove was able to show that the scattering law—that is, *the partial differential scattering cross-section*—for nuclear scattering has the following form:

$$\left(\frac{d^2\sigma}{d\Omega dE'} \right) = \frac{k'}{k} \frac{1}{2\pi\hbar N} \sum_{ll'} b_l b_{l'} \int_{-\infty}^{\infty} dt \langle e^{-i\mathbf{Q}\cdot\mathbf{r}_{l'}(0)} e^{i\mathbf{Q}\cdot\mathbf{r}_l(t)} \rangle e^{-i\omega t}, \quad (2.25)$$

thus arriving to the final form of the scattering law defined by Van Hove denoted as

$$S(\mathbf{Q}, \omega) = \frac{1}{2\pi\hbar N} \sum_{ll'} b_l b_{l'} \int_{-\infty}^{\infty} dt \langle e^{-i\mathbf{Q}\cdot\mathbf{r}_{l'}(0)} e^{i\mathbf{Q}\cdot\mathbf{r}_l(t)} \rangle e^{-i\omega t}. \quad (2.26)$$

In the above expression, \mathbf{Q} is defined as the scattering vector and ω is the energy of the scattered neutrons. N is the number of nuclei, t is time and the angular brackets $\langle \dots \rangle$ are used to denote the average over all the possible thermodynamic states of the sample.

2.3.2 The Correlation Function

From (2.25) we can see that the goal of most neutron scattering experiments is to measure $S(\mathbf{Q}, \omega)$. In order to understand how the microscopic properties of the system are contained in this expression let's consider the operator in equation (2.26), which is referred to as the intermediate pair correlation function or the intermediate scattering function:

$$I(\mathbf{Q}, t) = \frac{1}{N} \sum_{ll'} \langle e^{-i\mathbf{Q} \cdot \mathbf{r}_{l'}(0)} e^{i\mathbf{Q} \cdot \mathbf{r}_l(t)} \rangle. \quad (2.27)$$

For the moment, we have let the scattering lengths of all the atoms in our sample be equal. That is, $b_l = b_{l'} = b$. This assumption allowed us to remove the scattering lengths from the summation in (2.26) and thus define (2.27). The above definition also allows us to rewrite the expression for the scattering law as

$$S(\mathbf{Q}, \omega) = \frac{1}{2\pi\hbar N} \int I(\mathbf{Q}, t) e^{-i\omega t} dt. \quad (2.28)$$

$S(\mathbf{Q}, \omega)$ is also referred to as the dynamical structure factor, and since it is directly related to the partial differential scattering cross section, it contains information on both the position and motions of all the atoms in the sample. Fourier transforming equation (2.28) with respect to \mathbf{Q} and t , we obtain the so called *time dependent pair correlation function* introduced by Van Hove.

$$G(\mathbf{r}, t) = \frac{1}{2\pi^3} \int I(\mathbf{Q}, t) e^{-i\mathbf{Q} \cdot \mathbf{r}} d\mathbf{Q}. \quad (2.29)$$

Furthermore, the sum of the atomic sites in (2.27) and consequently (2.29) can be re-written using the delta function, such that $G(\mathbf{r}, t)$ describes the probability of having two atoms l and l' in a well-defined temporal and spacial correlation. Equation (2.29) owes its name to the fact that

it describes how the correlation between two particles evolves with time. That is, it describes the correlation between the atom l' at time $t = 0$ at the position \mathbf{r}' and the atom l at time t at another position $\mathbf{r}' + \mathbf{r}$:

$$G(\mathbf{r}, t) = \frac{1}{N} \sum_{ll'} \int \langle \delta(\mathbf{r}' - \mathbf{r}_{l'}(0)) \delta(\mathbf{r}' + \mathbf{r} - \mathbf{r}_l(t)) \rangle d\mathbf{r}'. \quad (2.30)$$

Thus, $G(\mathbf{r}, t)$, could be considered as the most borad description of the statics and dynamics of the system on an atomic scale. To conclude, we are now in a position to re-write an expression for the scattering law or the dynamical structure factor given by equation (2.26)

$$S(Q, w) = \frac{Nb^2}{2\pi\hbar} \int_{-\infty}^{\infty} G(\mathbf{r}, t) e^{-i\mathbf{Q}\cdot\mathbf{r}} e^{-i\omega t} d\mathbf{Q} dt. \quad (2.31)$$

And for the sake of completeness, we also re-write an expression for the final cross-section formula given by (2.25)

$$\left(\frac{d^2\sigma}{d\Omega dE'} \right) = \frac{k'}{k} \frac{Nb^2}{2\pi\hbar} \int_{-\infty}^{\infty} G(\mathbf{r}, t) e^{-i\mathbf{Q}\cdot\mathbf{r}} e^{-i\omega t} d\mathbf{Q} dt. \quad (2.32)$$

Summarized in these functions is the power of neutron scattering as an experimental technique: what is measured in a neutron scattering experiment is simply the space and time Fourier transform of a function that gives the probability of finding two atoms a certain distance apart.

2.3.3 Coherent and Incoherent Scattering

It is convenient to express total scattering cross section given by (2.22) as a sum of the coherent and incoherent parts:

$$\left(\frac{d^2\sigma}{d\Omega dE'} \right)_{TOT} = \left(\frac{d^2\sigma}{d\Omega dE'} \right)_{coh} + \left(\frac{d^2\sigma}{d\Omega dE'} \right)_{inc}. \quad (2.33)$$

The need to make such distinction arises from the fact that even for an element containing a single isotope, not all the scattering lengths will be equal. This is a result of the fact that the scattering length of a nucleus depends on its spin state; that is, the magnitude of b varies depending on whether the spins of the nucleus and neutron are parallel or antiparallel. The sum

in equation (2.26) can be averaged over the total volume of the sample since there is no correlation between the scattering lengths of different atoms in the sample b_l and $b_{l'}$. Thus, we have two cases, one in which $l = l'$, which yields an average of:

$$\langle b_l b_{l'} \rangle = \langle b^2_l \rangle = \langle b^2 \rangle, \quad (2.34)$$

while that of $l \neq l'$ can be written as

$$\langle b_l b_{l'} \rangle = \langle b_l \rangle \langle b_{l'} \rangle = \langle b \rangle^2. \quad (2.35)$$

Recalling that the average coherent cross-section per atom is given by

$$\sigma_{coh} = 4\pi \langle b \rangle^2, \quad (2.36)$$

while the total scattering cross section can be represented by

$$\sigma_{tot} = 4\pi \langle b^2 \rangle. \quad (2.37)$$

Now, using $\sigma_{inc} = \sigma_{tot} - \sigma_{coh}$ we can finally define the coherent and incoherent scattering lengths as

$$b_{coh} = \langle b \rangle \text{ and } b_{inc} = \sqrt{\langle b^2 \rangle - \langle b \rangle^2}. \quad (2.38)$$

Using (2.38), we can rewrite the individual components of equation (2.33) so as to include the actual quantity measured in a neutron experiment, namely, the dynamical structure factor. We thus have,

$$\left(\frac{d^2\sigma}{d\Omega dE'} \right)_{coh} = N \frac{k'}{k} \langle b \rangle^2 S_{coh}(\mathbf{Q}, \omega), \text{ and} \quad (2.39)$$

$$\left(\frac{d^2\sigma}{d\Omega dE'} \right)_{inc} = N \frac{k'}{k} [\langle b^2 \rangle - \langle b \rangle^2] S_{inc}(\mathbf{Q}, \omega). \quad (2.40)$$

Physically, coherent scattering describes interference between waves that are produced as a result of a neutron scattering from all the nuclei in the sample. Consequently, the intensity of the signal observed varies strongly with the scattering angle. On the other hand, in the case of incoherent scattering, the scattered waves from different nuclei do not interfere with each other

since it measures self-correlations of atoms at different times. Thus, incoherent scattering yields information about the diffusion of atoms in a system. In general, in the scattering process, the interference between the different scattered waves is normally neither complete nor completely absent. Usually, incoherent scattering is mostly isotropic (specially in the case of small Q and low temperatures), and it is characterized by a decrease in intensity as both the values of Q and T increase. However, there is the special case of Quasielastic Neutron Scattering (QENS) (covered in section 2.3.5) in which a Doppler-like broadening of otherwise elastically scattered neutrons—characterized by a Lorentzian line shape—is observed due to reorientational or diffuse motions of atoms in the target.

There are a few prominent examples for which a large incoherent scattering is useful for neutron scattering experiments. Regarding the case of single atomic species, one of the most important incoherent scatterers is Hydrogen with $\sigma_{inc} = 80.3$ barns/atom while only a value of $\sigma_{coh} = 1.76$ barns/atom. Thus, in samples containing large amount of Hydrogen coherent scattering is usually neglected. Vanadium metal is another example, and it is often used as a standard for calibrating the neutron flux at the sample position of a spectrometer.

Since QENS will be covered at the end of this chapter, for the remainder of the discussion of the *partial differential scattering cross-sections* for the various scattering processes (i.e. elastic and inelastic scattering) we will drop the subscript *coh* with the understanding that we will be referring to the coherent part of the wave function.

2.3.4 Coherent Elastic Scattering: Nuclear and Magnetic

Nuclear Scattering

The scattering law for diffraction (Bragg scattering) is one of the most important applications of Van Hove's scattering law $S(\mathbf{Q}, \omega)$ given by (2.26). Recall from (2.17) that in a diffraction

experiment, what is measured is the differential cross-section, which gives the time-averaged (equilibrium) position of all the nuclei in the sample. It is then necessary to integrate (2.26) over the range of energies w , which results in a Dirac delta function $\delta(t)$. As result, the pair correlation function, $G(\mathbf{r}, t)$, [see equation (2.30)] must be evaluated at $t = 0$ for the case of diffraction.

First, in order to write down $S(\mathbf{Q}, \omega)$, we make use of the elegant definition of the so-called atomic density operator introduced by Van Hove:

$$\rho_Q(t) = \sum_l e^{i\mathbf{Q}\cdot\mathbf{r}_l(t)}. \quad (2.41)$$

The general expression for coherent, elastic neutron scattering is the time average of $\rho_Q(t)$, so that

$$S(\mathbf{Q}, \omega) = \delta(\hbar\omega) \frac{1}{N} \langle \sum_{ll'} e^{i\mathbf{Q}\cdot(\mathbf{r}_l - \mathbf{r}_{l'})} \rangle. \quad (2.42)$$

For the case of a Bravais lattice, with one atom per unit cell the Bragg condition requires that $\mathbf{Q} = \mathbf{G} = \mathbf{k} - \mathbf{k}'$, such that the scattering law takes the following form:

$$S(\mathbf{Q}, \omega) = \delta(\hbar\omega) \frac{(2\pi^3)}{v_0} \sum_{\mathbf{G}} \delta(\mathbf{Q} - \mathbf{G}), \quad (2.43)$$

with v_0 and the vectors \mathbf{G} representing the unit cell volume and reciprocal lattice vectors, respectively. Thus, the differential cross-section for a perfectly rigid lattice (notice that we have removed the thermodynamic averaging brackets from (2.42)) can be written as:

$$\frac{d\sigma}{d\Omega} = N \frac{(2\pi^3)}{v_0} \langle b \rangle^2 \sum_{\mathbf{G}} \delta(\mathbf{Q} - \mathbf{G}). \quad (2.44)$$

In reality, however, atoms are not fixed, but rather they oscillate about the equilibrium position. As temperature increases the thermal motion also increases, thus causing a decrease in Bragg peak intensities. This decrease is parametrized by a term denoted as the Debye-Waller factor, which gets introduced into the final expression for $d\sigma/d\Omega$ as a consequence of averaging

the phase factor $e^{-i\mathbf{Q}\cdot\mathbf{r}}$ in (2.42). Thus, we have that for a non-Bravais lattice, the *coherent elastic differential cross-section* takes the general form

$$\frac{d\sigma}{d\Omega} = N \frac{(2\pi^3)}{v_0} \sum_{\mathbf{G}} \delta(\mathbf{Q} - \mathbf{G}) |F_N(\mathbf{G})|^2, \quad (2.45)$$

where

$$|F_N(\mathbf{G})| = \sum_j \langle b_j \rangle e^{i\mathbf{G}\cdot\mathbf{d}_j} e^{-W_j(\mathbf{Q}, T)}. \quad (2.46)$$

In the above expressions, the static nuclear structure factor, $F_N(\mathbf{G}) = F_N(hkl)$, is evaluated at the j^{th} atom within the unit cell that sits at position \mathbf{d}_j and also contains information on the thermal atomic displacements $\langle \mathbf{u}_j^2(T) \rangle$. The latter comes from the Debye-Waller factor, $W_j(\mathbf{Q}, T)$, where for small displacements of an atom from its equilibrium position \mathbf{r} , it is given by:

$$W_j(\mathbf{Q}, T) = \frac{1}{2} \langle (\mathbf{Q} \cdot \mathbf{u}_j(T))^2 \rangle. \quad (2.47)$$

In a diffraction experiment, $|F_N(\mathbf{G})|^2$, can be obtained by integrating the intensity of observed through a scan of the Bragg peak. Thus, it is dependent on the resolution function of the particular instrument used. By measuring the structure factor for a large number of Bragg reflections within a given sample, a model for the atomic parameters can be constructed.

Magnetic Scattering

The master formula, equation (2.22) can be generalized now for the case of magnetic scattering. Let V_m represent the magnetic interaction for unpolarized neutrons and $\boldsymbol{\sigma}$ and $\boldsymbol{\sigma}'$ denote the spin states of the incoming and scattered neutrons, respectively. Then, the partial differential scattering cross-section for magnetic interaction can be represented as

$$\left(\frac{d^2\sigma}{d\Omega dE'} \right)_{\boldsymbol{\sigma} \rightarrow \boldsymbol{\sigma}'} = \frac{k'}{k} \left(\frac{m_n}{2\pi\hbar^2} \right)^2 |\langle \mathbf{k}' \boldsymbol{\sigma}' | V_m | \mathbf{k} \boldsymbol{\sigma} \rangle|^2 \delta(E_\lambda - E_{\lambda'} + E - E'), \quad (2.48)$$

with the interaction between the neutron and unpaired electron in the sample is given by,

$$V_m(\mathbf{r}) = -\boldsymbol{\mu}_n \cdot \mathbf{B}(\mathbf{r}). \quad (2.49)$$

From (2.46) we have that $\boldsymbol{\mu}_n = -\gamma\mu_N\boldsymbol{\sigma}$ is the magnetic dipole moment of the neutron, where γ (=1.913) is the gyromagnetic ratio, μ_N is the nuclear magneton, and $\boldsymbol{\sigma}$ is the spin operator. $\mathbf{B}(\mathbf{r})$ represents the magnetic field that is generated from the spin of the electron and its orbital motion

$$\mathbf{B}(\mathbf{r}) = \nabla \times \mathbf{A} = \nabla \times \left(\frac{\boldsymbol{\mu}_e \times \mathbf{r}}{|\mathbf{r}|^3} \right) - \frac{e}{c} \frac{v_e \times \mathbf{r}}{|\mathbf{r}|^3}. \quad (2.50)$$

In the above equation, first term represents the magnetic vector potential with \mathbf{r} as the distance from the electron to the point where the magnetic field is measured and $\boldsymbol{\mu}_e = -2\mu_B\boldsymbol{\sigma}$ is the magnetic moment of an electron where $\mu_B = 9.27402 \cdot 10^{-24} \text{J/T}$ is the Bohr magneton and $\boldsymbol{\sigma}$ is the spin operator of the electron. The second term arises from the orbital motion of the electron with v_e , e , and c denoting the velocity of the electron, the elementary charge and the speed of light, respectively.

Just like we outlined in the section for nuclear scattering, the matrix element in equation (2.48) is required to arrive at a final expression for the cross section. The details of such derivation are not relevant in this discussion, the reader can see for example Appendix D of [56]. Thus, suffice it to say that upon substituting the above expressions into the matrix element of the master formula given above, the magnetic neutron cross-section for unpolarized neutrons, identical magnetic ions with localized electron spins, and spin-only scattering is given by:

$$\left(\frac{d^2\sigma}{d\Omega dE'} \right)_{\sigma \rightarrow \sigma'} = \frac{k'}{k} \left(\frac{m_n}{2\pi\hbar^2} \right)^2 p^2 F(\mathbf{Q})^2 e^{-2W(\mathbf{Q})} \sum_{\alpha,\beta} \left(\delta_{\alpha,\beta} - \frac{Q_\alpha Q_\beta}{Q^2} \right) S^{\alpha,\beta}(\mathbf{Q}, \omega), \quad (2.51)$$

where $p = \frac{\gamma e^2}{2m_e c^2}$, $F(\mathbf{Q})$ is the dimensionless magnetic form factor defined as the Fourier transform of the normalized spin density associated with the magnetic ions, with $\alpha, \beta = x, y, z$,

and with the term $e^{-2W(\mathbf{Q})}$ denoting the Debye-Waller factor. As in the discussion with nuclear scattering, the main goal is to be able to write an expression for the scattering law, in this case, $S^{\alpha,\beta}(\mathbf{Q}, \omega)$. Such expression takes the following form:

$$S^{\alpha,\beta}(\mathbf{Q}, \omega) = \frac{1}{2\pi} \int_{-\infty}^{\infty} dt e^{-i\omega t} \sum_l e^{i\mathbf{Q}\cdot\mathbf{r}_l} \langle S_0^\alpha(0) S_l^\beta(t) \rangle, \quad (2.52)$$

where the angle brackets denote the average over configurations. In the above equation, the term $\langle S_0^\alpha(0) S_l^\beta(t) \rangle$ is the magnetic analog of the expression (2.30) obtained in previous section for the time dependent pair correlation function $G(\mathbf{r}, t)$. Thus, it is referred to as the *time dependent spin-spin correlation function*. Furthermore, we are able to reach here the same conclusion as we did for the case of nuclear scattering, namely that the partial differential scattering cross-section given by (2.51) is the Fourier transform in space and time of the spin-spin correlation function. As a result, magnetic elastic scattering probes static ordered moments while the inelastic counterpart probes dynamic (fluctuating) moments. Shown in Figure 2.4 is a schematic representation of the relationship between the measured magnetic neutron scattering cross section and the time dependent spin-spin correlation function for \mathbf{Q} and energy scans. The top panel shows how the relaxation rate Γ measured at half width at half maximum (HWHM) in energy of $S(\mathbf{Q}, \omega)$ is inversely proportional to the lifetime of the excitation τ . In a neutron experiment, such energy dependence of $S(\mathbf{Q}, \omega)$ is useful in determining information specific to the magnetic moment in the system. For example, a limited $\hbar\omega$ -resolution in the scattering function $S(\mathbf{Q}, \omega)$, indicates a long-range order for the magnetic moments. On the other hand, if $S(\mathbf{Q}, \omega)$ is much broader than the instrumental $\hbar\omega$ -resolution, we could conclude that the lifetime of the excitations are small in time. Similarly, the linewidth κ is the HWHM in momentum transfer of $S(\mathbf{Q}, \omega)$, and thus is inversely proportional to the correlation length denoted by ξ . Then by looking at the bottom panel where we have a Q -dependence of $S(\mathbf{Q}, \omega)$,

we are able to determine information on the spatial dependence of the spin correlations. For instance, for cases in which $S(\mathbf{Q}, \omega)$ is Q -resolution limited, we would have long-range spatial correlations. Conversely, if the opposite is true, that is, if our peak is much broader than the instrumental Q -resolution, such correlations are said to be short-range.

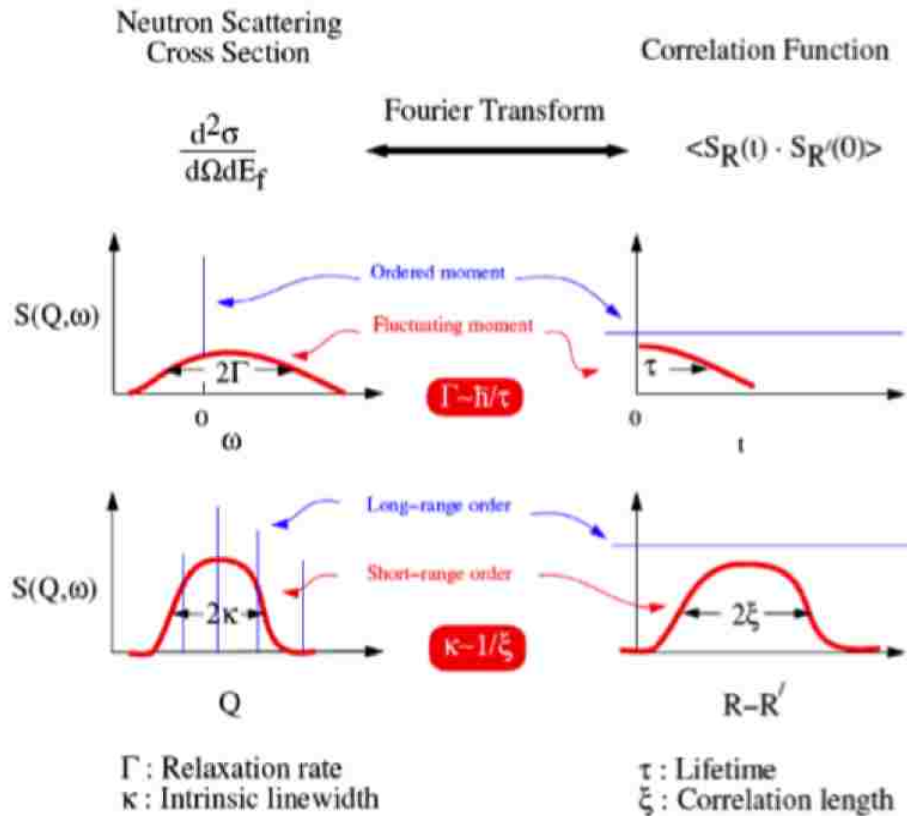


FIGURE 2.4 Neutron scattering profile in reciprocal (left) and real space (right) where the neutron scattering cross section's Fourier transform is the so called time dependent spin-spin correlation function. Elastic signal (top left blue) in reciprocal space represents an ordered moment in real space while the relaxation rate (Γ) of a fluctuating moment (top left red) is proportional to the lifetime of the excitation (τ) in real space. Similarly, the intensity profile on lower left blue (lower left red, showing an intrinsic linewidth κ) corresponds to long-range order (a finite correlation length ξ) in real space (Adapted from [19]).

The magnetic analog of equations (2.45) and (2.46), that is, the coherent elastic differential cross section for a magnetic ordered crystal are given by:

$$\frac{d\sigma}{d\Omega} = N_M \frac{(2\pi^3)}{v_M} \sum_{\mathbf{G}_M} \delta(\mathbf{Q} - \mathbf{G}_M) |F_M(\mathbf{G}_M)|^2, \quad (2.53)$$

where $F_M(\mathbf{G}_M)$, the static magnetic structure factor, is given by

$$|F_M(\mathbf{G}_M)| = \sum_j p_j \mathbf{S}_{\perp j} e^{i\mathbf{G}_M \cdot \mathbf{d}_j} e^{W_j}. \quad (2.54)$$

The subscript M denotes the magnetic origin, both N_M and v_M refer to the volume and number of magnetic unit cells in the sample; similarly \mathbf{G}_M denotes the reciprocal lattice vector of the magnetic unit cell while the factor $p_j \mathbf{S}_{\perp j}$ is the magnetic scattering amplitude of the j^{th} ion with the subscript \perp is used to indicate that only the component of \mathbf{S} perpendicular to \mathbf{Q} contributes to the scattering amplitude (see discussion at the end of this section). Notice that equations (2.53) and (2.54) are equivalent to their nuclear scattering counterparts given earlier by (2.45) and (2.46), from which we have carried all terms, with the understanding that we are considering their magnetic analogue.

Similarly to the case of elastic neutron scattering, the area under the magnetic Bragg peak (integrated intensity) is directly proportional to $|F_M(\mathbf{G}_M)|^2$. Thus, by measuring a large number of magnetic Bragg diffraction peaks, one can determine a model of the magnetic spin structure (i.e. amplitude and orientation of spins) for the sample in question.

Nuclear vs. Magnetic Scattering

There are two significant differences between the theories of nuclear and magnetic scattering. One is the fact that the cross-section for nuclear scattering is a scalar quantity, whereas that of magnetic has a vectorial component dependent on the magnetic field; if the neutron spin is perpendicular to \mathbf{Q} , it can change its state by precessing in the field. That is, magnetic scattering is characterized by a dipolar nature (see Figure 2.5). The term responsible for this is the

polarization factor $\left(\delta_{\alpha,\beta} - \frac{Q_\alpha Q_\beta}{Q^2}\right)$ in equation (2.51). These spin-dependent terms in the scattering cross-section can be used to provide additional details about the scattering systems. Polarized neutrons (refer to Chapter 3 for a brief comment on the polarized neutron scattering technique) have a crucial place in neutron scattering as they can 1) unambiguously determine moment directions, and 2) distinguish between collective excitations (i.e. isolate contributions from phonons to the magnon spectra) and single-particle excitations (i.e. between coherent and incoherent scattering).

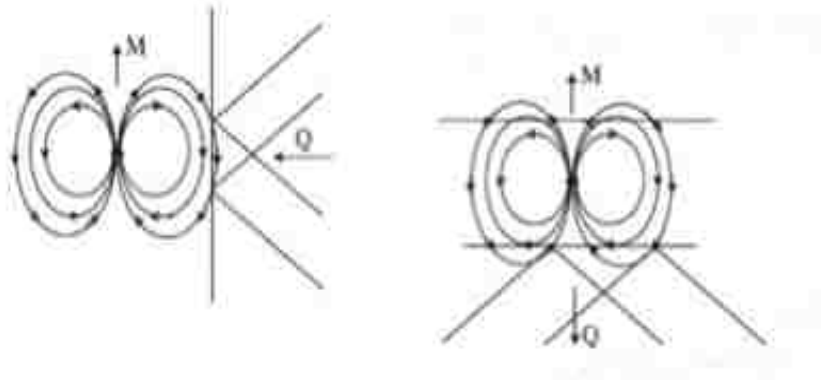


FIGURE 2.5 Anisotropic nature of magnetic scattering. Only the component of the sample magnetization (\mathbf{M}) that is perpendicular to (\mathbf{Q}) will scatter neutrons. Left: the magnetic field amplitudes of the dipole field are shown for $\mathbf{M} \perp \mathbf{Q}$ (constructive interference) and $\mathbf{M} \parallel \mathbf{Q}$ (destructive interference). Figure adapted from [19].

The second difference is marked by the form factors for each of the scattering processes. In the case of nuclear scattering, $F_N(\mathbf{Q})$ remains constant because the scattering is isotropic in nature, which means that the neutron always sees nucleus/scattering center as a point. On the other hand, the combined amplitudes in the form factor for magnetic scattering, $F_M(\mathbf{G}_M)$, develop a phase difference as the scattering angle, 2θ , increases. The latter is due to the fact that the dimensions of the electronic cloud become comparable to that of the neutron wavelength as the scattering angle increases. Thus, in a neutron scattering experiment increasing the wavevector \mathbf{Q} will cause

the intensity of magnetic Bragg peaks to decrease. These provide a unique opportunity to distinguish magnetic from nuclear scattering without the use of polarization analysis; that is, we can usually select an appropriate Brillouin zone suited for the type of scattering we are looking for.

2.3.5 Inelastic Scattering: Phonons and Magnons

In order to begin this discussion, it is standard to first introduce the Principle of Detailed Balance and the Fluctuation Dissipation Theorem. This allows us to express the dynamical structure factor $S(\mathbf{Q}, \omega)$ for phonons and magnons in a much simpler and intuitive form. Because of the complexity that arises as we consider inelastic scattering processes, only general cases will be discussed in this section. That is, detailed expressions for the specific cross-sections and dynamical structure factors will not be presented. This section is more of a qualitative nature aimed at a quick introduction to collective excitations in neutron scattering.

Principle of Detailed Balance

So far we have only dealt with elastic scattering. Consider now, the scattering law or dynamical structure factor $S(\mathbf{Q}, \omega)$, from which we have subtracted all the elastic contributions (Bragg scattering). As a result, $S(\mathbf{Q}, \omega)$ will only contain information about fluctuations in the sample. Recall that for inelastic scattering processes (section 2.2.2) there is either energy lost or gained by sample from the neutrons.

Consider now a thermodynamic system in equilibrium in which there are two states separated by an energy $\hbar\omega$, the principle of detailed balance accounts for the fact that the probability that the system is in the lower energy state is greater by a factor of $e^{\hbar\omega/k_B T}$ than the probability of finding the system in a higher energy state. Thus, the system satisfies the so-called detailed balance relationship expressed as:

$$S(-\mathbf{Q}, -\omega) = e^{\left(\frac{-\hbar\omega}{k_B T}\right)} S(\mathbf{Q}, \omega). \quad (2.55)$$

From the above expression we can see that the principle of detailed balance relates the response function for the neutron energy gain and energy loss processes with equal but opposite wavevectors.

Fluctuation Dissipation Theorem

This theorem relates the scattering function $S(\mathbf{Q}, \omega)$ and the imaginary part of the dynamical susceptibility, $\chi''(\mathbf{Q}, \omega)$, via the following relation:

$$S(\mathbf{Q}, \omega) = \frac{\hbar}{\pi} (n(E) + 1) \chi''(\mathbf{Q}, \omega). \quad (2.56)$$

In the above, the factor $n(E)$ is the Bose-Einstein population factor given by

$$n(E) = \frac{1}{e^{\left(\frac{\hbar\omega}{k_B T}\right)} - 1}, \quad (2.57)$$

which determines the number of collective excitations (e.g. spin waves) that are thermally populated at each energy, which is directly proportional to the intensity of the inelastic signal observed. For example, a neutron can create a spin wave in the system while losing energy. The probability of this occurring is $1 + n(E)$. On the other hand, the probability of neutron gaining energy from the system (annihilating a spin wave excitation) is proportional to $n(E)$ at the corresponding spin wave energy E .

Equation (2.56) is actually more important than it might seem at first glance; it directly relates the dynamical structure factor—a term directly extracted from the measured partial differential scattering cross-section—to a quantity that is easily calculated by theorists— $\chi''(\mathbf{Q}, \omega)$.

The generalized susceptibility $\chi(\mathbf{Q}, \omega)$, is a complex function with both real and imaginary parts. The former is referred to as the dynamical susceptibility $\chi'(\mathbf{Q}, \omega)$ and is a measure of how

the system responds to external stimuli. The imaginary part, given by $\chi''(\mathbf{Q}, \omega)$, deals with how energy is dissipated by the system. Thus, the power of equation (2.56) is that it allows for a direct test of theoretical models to the obtained experimental data.

Furthermore, if we make use of the Kramers-Kronig relation we can relate the real and imaginary parts of the susceptibility by:

$$\chi'(\mathbf{Q}, \omega) = \frac{1}{\pi} \int_{-\infty}^{\infty} d\omega' \frac{\chi''(\mathbf{Q}, \omega')}{\omega - \omega'}. \quad (2.58)$$

By letting $\omega = 0$, we obtain an expression for the static susceptibility of the following form

$$\chi'(\mathbf{Q}, 0) = \frac{1}{\pi} \int_{-\infty}^{\infty} d\omega' \frac{\chi''(\mathbf{Q}, \omega')}{\omega'}. \quad (2.59)$$

Furthermore, in the limit of small \mathbf{Q} (let $\mathbf{Q} \rightarrow 0$), the real part of the generalized susceptibility now becomes the bulk (uniform) susceptibility usually denoted by χ_b (i.e $\chi'(0,0) = \chi_b$). The latter is the same bulk susceptibility that is obtained by using a dc magnetometer or a magnetic resonance technique. Thus, again we see the connection between a measurement of the partial differential scattering cross-section from neutron experiments and the imaginary part of the susceptibility.

Phonons

Collective excitations of the lattice, phonons, are superposition of waves used to describe the coherent thermal motion of the atoms about their lattice sites. If we consider a lattice with n atoms in a unit cell, we have a total of $3n$ phonon branches with different frequencies. Let the phonon frequencies, be denoted by $\omega_{\mathbf{q}s}$ where \mathbf{q} is the wavevector of the excitation and s is used to differentiate between the different modes. We then make use of (2.56) to relate the imaginary part of the dynamical susceptibility for a single phonon (see, for example [57]) to the measured quantity in a neutron scattering experiment, $S(\mathbf{Q}, \omega)$. It can be shown that for the case of a

neutron either creating or destroying a single phonon, the integrated intensity for a constant- \mathbf{Q} scan is given by:

$$I = A \frac{1}{w_{qs}} |F(\mathbf{Q})|^2 \times (n_{qs} + 1) \quad (2.60)$$

for the case of neutron energy loss, and

$$I = A \frac{1}{w_{qs}} |F(\mathbf{Q})|^2 \times n_{qs} \quad (2.61)$$

for that of energy gain. Recall that n_{qs} is the Bose-Einstein factor given by equation (2.57).

Some useful limiting cases of the latter are $(n_{qs} + 1) = 1$ for cases in which $\hbar\omega_{qs} \gg k_B T$ and in

the low temperature limit, $\hbar\omega_{qs} \ll k_B T$, $(n_{qs} + 1) = \frac{k_B T}{\hbar\omega_{qs}}$. Above, $F(\mathbf{Q})$ is the dynamic

structure factor (not given explicitly here) that contains terms such as the Debye-Waller factor

and a polarization vector for a particular mode s . There is no simple way to determine what the

polarization for a particular vector \mathbf{Q} will be. Nonetheless, there are specific cases such as that of

acoustic phonons which yield a much simplified expression for the dynamical structure factor.

Magnons

Spin waves are the analogue of the normal modes of nuclear displacements. They are caused by

the coherent fluctuations of the individual magnetic moments, which are coupled to one another

by exchange interactions (e.g. direct overlap of atomic wave functions, superexchange, or

RKKY). Their energy is quantized, with $E = \hbar\omega$, relative to its ground state. The term magnon

refers to the quanta of energy, which can either be absorbed or emitted by a neutron as it scatters

from a magnetic system, resulting in the absorption or emission of magnons. Classically, if we

allow the spins to precess about their axes, a spin wave can be visualized as a constant phase

difference between the precession rates of neighboring spins (see Figure 2.6).

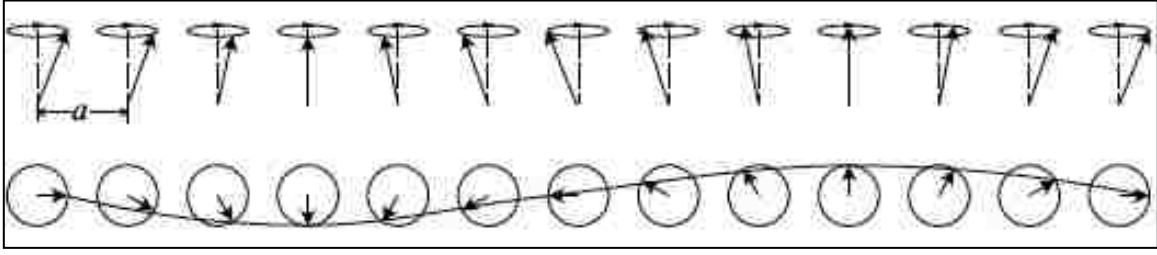


FIGURE 2.6 Schematic representation of a spin wave. Top panel shows precession of spins about their axis. Bottom panel is the top view of such precession, with one wavelength shown. Figure adapted from [14].

In order to obtain the partial differential scattering cross-section for magnons, the starting point would be equation (2.51). The dipolar nature of the magnetic interaction only allows spin wave displacements in the directions perpendicular to the average spin direction. Thus, we can conveniently choose the average spin direction to be along z ; taking only the relevant terms from (2.51), that is, the polarization factor and the dynamical structure factor, we have:

$$\sum_{\alpha,\beta} \left(\delta_{\alpha,\beta} - \frac{\mathbf{Q}_\alpha \mathbf{Q}_\beta}{Q^2} \right) S^{\alpha,\beta}(\mathbf{Q}, \omega) = \frac{1}{2} (1 + Q_z^2) S_{SW}(\mathbf{Q}, \omega). \quad (2.62)$$

The goal is to be able to find an expression for $S_{SW}(\mathbf{Q}, \omega)$. Such task is specific to the magnetic orientations of spins in the sample such that the dynamical structure factor will be different for the case of antiferromagnets and ferromagnets. Because of the mathematical complexity involved in this process, the derivation of such expression for these cases falls outside of the scope of this thesis work. Nonetheless, the approach is the same as outlined in this section: we make use of $S(\mathbf{Q}, \omega) = \frac{\hbar}{\pi} (n(E) + 1) \chi''(\mathbf{Q}, \omega)$ and find an expression for the imaginary part of the dynamical susceptibility. However, for the sake of a qualitative understanding of phonon and magnon dispersions, it is appropriate here to give a brief overview of each of the spin wave dispersion relations.

For the case of Heisenberg ferromagnet with only nearest neighbor interactions, the spin wave dispersion (at small \mathbf{q}) is given by:

$$\hbar\omega_{\mathbf{q}} = Dq^2, \quad (2.63)$$

where spin wave stiffness constant is given by

$$D = 2JSa^2. \quad (2.64)$$

The term J is the exchange energy, S denotes value of the spin, and a is the lattice constant. The quantitative value of the spin wave stiffness constant can be extracted from a fit to the dispersion relation and thus it contains information concerning the interaction and nature of magnetism.

On the other hand, in an antiferromagnet the spin wave intensity peaks near an antiferromagnetic superlattice peak instead of near a Bragg peak as in the case of ferromagnets. Thus the spin wave dispersion for a Heisenberg antiferromagnet (at small \mathbf{q}) with only nearest-neighbor interactions is represented as:

$$\hbar\omega_{\mathbf{q}} = \hbar c q, \quad (2.65)$$

where the spin wave velocity c is given by

$$c = zJS \frac{a}{\hbar}. \quad (2.66)$$

The constant z is the number of nearest neighbors, and as before J is the superexchange energy.

2.3.6 Diffuse and Quasielastic Magnetic Scattering

Recall from section 2.3.3 that elastic, coherent scattering is restricted to Bragg peaks. However, real crystals do show additional scattering peaks near and around Bragg peaks. The elastic part of this scattering is referred to as diffuse scattering. The latter is attributed to imperfections in the crystal (e.g. vacancies and substitutional atoms), referred to as point defects. Such defects in crystals usually have considerable consequences for magnetism, since they may affect the local

structure of the compound. As we will see in Chapter 5, this type of scattering, contains information on short-range correlations. Furthermore, they can also give rise to resonant and local modes, thus affecting the dynamical properties of the system (refer to [56] for a more involved discussion of point defects). It is in this way that diffuse scattering also reveals information on fluctuations of nuclear and magnetic origin. In this thesis work, we present results (see Chapter 5) from diffuse magnetic scattering. Thus, the present section concentrates on the magnetic diffuse scattering case.

As done in previous section, the use of the dynamic susceptibility is useful in the treatment of diffuse scattering as well. Recall that from section 2.3.5, equation (2.59) states that the dynamical susceptibility equals the bulk susceptibility in the appropriate limit

$$\chi'(0,0) = \chi_b. \quad (2.67)$$

Thus, it follows that from (2.59), that it is always possible to choose a general form for $\chi''(\mathbf{Q}, 0)$ that ensures the following relation is satisfied (hence the convenience of discussing the scattering in terms of the dynamic susceptibility, rather than in terms of $S(\mathbf{Q}, \omega)$):

$$\chi''(\mathbf{Q}, \omega) = \chi'(\mathbf{Q}, \omega)\omega F(\mathbf{Q}, \omega). \quad (2.68)$$

Above, $F(\mathbf{Q}, \omega)$, is called the spectral weight function and is an even function of ω satisfying the normalization condition:

$$\int_{-\infty}^{\infty} F(\mathbf{Q}, \omega)d\omega = 1. \quad (2.69)$$

Quasielastic Scattering

In mixed-valence and heavy fermion compounds sometimes the localized moments interact with the delocalized conduction electrons. The latter results in a scattering mainly dependent on the magnetic form factor (lack of spatial correlation results in a susceptibility independent of \mathbf{Q}). If

the spin excitations are damped exponentially in time, then the spectral weight function takes the form of a Lorentzian

$$F(\mathbf{Q}, \omega) = \frac{1}{\pi} \frac{\Gamma}{\omega^2 + \Gamma^2}. \quad (2.70)$$

As a result, the imaginary part of the susceptibility from equation (2.68) becomes

$$\chi''(\mathbf{Q}, \omega) = \frac{\chi'(\mathbf{0}, \omega)}{\pi} \frac{\omega \Gamma}{\omega^2 + \Gamma^2}. \quad (2.71)$$

In (2.71) Γ denotes the linewidth of the excitation, and it is in cases for which its value is comparable to the energy resolution (i.e. relatively small) that the scattering becomes “quasielastic”.

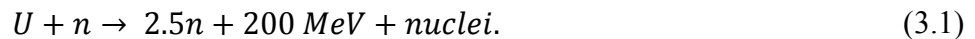
Chapter 3

Experimental

This chapter is intended to familiarize the reader with the experimental tools used in this investigation. For in depth coverage and details regarding neutron production and detection the reader can consult [56] and [60]. An excellent book that covers the triple-axis basic techniques and instrumentation details has been written by Gen Shirane, Saphiro, and Tranquada is cited here [55]. Instrument specifications with complete descriptions can be found online on the instrument section of both Oak Ridge National Laboratory and the National Institute of Standards and Technology website. Because of the wide range of instruments used, specific details of pertaining to the instrumental set-up and configurations employed for each study will be provided in the appropriate chapters.

3.1 Neutron Production and Detection

Today the two most commonly used neutron production reactions are those by thermal nuclear fission and spallation by protons. In the former, neutrons are generated with nuclear reactors by the fissioning of atoms in the reactor fuel. The choice for the reactor fuel is Uranium 235, which undergoes the following reaction after a slow neutron capture,



This exothermal reaction can be made self-sustaining because it releases more neutrons per fission process that are needed to initiate the process; these excess neutrons are the ones used in scattering experiments. The main advantage of a fission reactor source is that they produce a high flux of neutrons at a steady rate.

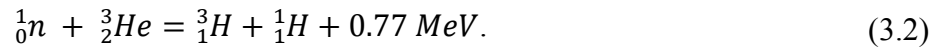
The other method of generating neutrons is by making an energetic beam of ions (generally protons) strike a heavy metal target thus knocking neutrons from the intra-nuclear cascade created as a result of highly energetic particles leaving the nucleus; these neutrons are referred to as spallation neutrons. Just like in the fission process, the excited nucleus left behind will start to evaporate neutrons, thus the low-energy part of the spectrum of both spallation and reactor sources are comparable. However, because of the resulting intra-nuclear cascade the energy spectrum of spallation sources extends up to that of the incident particles (1 GeV).

These two different methods of neutron production come each with their set of pros and cons. In the case of thermal nuclear fission, neutrons emerge from a reactor in a continuous stream. Thus, for scattering experiments a monochromatic beam must be obtained by using Bragg reflection from a single crystal. On the other hand, in spallation sources the neutrons arrive in pulses, eliminating the need to use a monochromator and allowing all the neutrons to be used. The latter is accomplished by measuring the time it takes a neutron to travel from the source to the detector—time of flight—providing in this way a measure of the neutron's velocity and energy. Another difference between these two types of neutron production methods is the amount of energy deposited in the target. For spallation sources, the energy deposited by the protons in the target is only of about 27 MeV/neutron compared to four or five times more for the case of nuclear fission. However, the cost of producing high energy protons for spallation sources is very high.

From both processes high energy neutrons with energies up to hundreds of mega-electron volts (MeV) are produced. However, as explained in Chapter 2, only neutrons with an energy range of meV are suited for our condensed matter experiments. Thus, these are slowed down in a moderator by multiple collisions until they approach thermal equilibrium. To achieve this energy

shift of several orders of magnitude, moderators made of light atoms such as D₂O and H₂O are commonly used. Neutrons thermalized in moderators at low temperature (e.g. by using liquid H₂O) are referred to as ‘cold neutrons’ while those at equilibrium at room temperature are ‘thermal neutrons’.

Because thermal neutrons have both small energies and lack electric charge, the detection of neutrons is possible only through the detection of ionizing radiation or particles that emerge from nuclear reactions with target atoms. The most common neutron detectors used are ³He gas tube detectors, which generate the following reaction with the incoming neutron:



In the ³He gas tube set up, the cathode consists of a steel tube that is filled with Helium 3 with a pressure ranging from 5-10 bar. Electrons generated by the ionizing particles resulting from the nuclear reactions with the incoming neutron, are accelerated through a high voltage of about 1800 Volts towards the anode, which runs along the cylinder axis. This causes even more ionizing particles that together with a gain factor of about 10⁵ produce an avalanche effect allowing for the signal to be detected. These types of detectors are commonly referred to as Geiger counters. Usually the same Helium 3 detector tube, but with a much lower pressure, is also used in order to measure the incident neutron flux.

The work presented in this thesis was conducted at the High Flux Isotope Reactor (HFIR) at Oak Ridge National Laboratory in Oak Ridge, TN; and at the National Institute of Standards and Technology in Gaithersburg, MD where neutrons are generated by thermal nuclear fission.

3.2 Single Crystal Synthesis

Prior to the neutron scattering experiments, the single crystals investigated in this thesis were synthesized and fully characterized by our collaborators. Elastic and inelastic studies of the structural and magnetic properties of 11 and 6 % Mn-doped Ruthenates were conducted using various single crystals specimens grown and characterized at Dr. Rongying Jin's laboratory at Louisiana State University by Dr. Biao Hu. Details on the growth and conditions can be found by consulting the following reference [45]. Elastic neutron scattering experiments on the doping dependence of phase segregation on PCMO 30, 35, and 40 systems, were conducted on single crystals synthesized and characterized at the Joint Research Center for Atom Technology (JRCAT) in Tsukuba, Japan by Dr. Y. Tomioka in Dr. Y. Tokura's group [61]. In addition, Dr. Tomioka and Tokura also provided the single crystals used for the inelastic neutron scattering investigation of spin-lattice coupling in LCMO 20 [62].

3.3 Triple-Axis Spectrometers

The bulk of the experiments, that is, elastic and inelastic measurements on 11 and 16% Mn substituted $\text{Sr}_3\text{Ru}_2\text{O}_7$, doping-dependence of phase segregation in $\text{Pr}_{1-x}\text{Ca}_x\text{MnO}_3$ ($x = 30, 35, 40$) using elastic neutron scattering and collective excitations for the spin-lattice coupling study in $\text{La}_{0.80}\text{Ca}_{0.20}\text{MnO}_3$ were all carried out at triple axis beam lines. Because of the tremendous versatility of this instrument, elastic, quasi-elastic, inelastic, and polarized experiments can all be performed on such instrument. The Triple-Axis Spectrometer (TAS) system is specially suited for inelastic neutron scattering experiments, due to the fact that they allow controlled access to the momentum \mathbf{Q} and energy ($\hbar\omega$) found in the scattering law $S(\mathbf{Q}, \omega)$. Triple-axis spectrometers at the High Flux Isotope Reactor (HFIR) at Oak Ridge National Laboratories in Oak Ridge, TN are operated and controlled through the Spectrometer Instrument Control

Environment (SPICE), which is a LabVIEW based program. Initial data treatment (i.e. browsing scans, combination of data sets, angle calculations, spurious check, etc.) was carried out using the Graffiti program within SPICE. DAVE is an integrated environment for the reduction, visualization, and analysis of inelastic neutron scattering data used for TAS at the National Institute of Standards and Technology (NIST) in Washington, DC [63].

Triple-Axis Spectrometer Components

In the triple-axis spectrometer (TAS), as the name implies, neutrons interact with three crystals on their way from the reactor to the detector, with each crystal being able to rotate about a vertical axes passing through their centers. The first crystal is the monochromator, whose job is to select a single monochromatic component from the whole neutron beam. The sample constitutes the second crystal and the third one is the analyzer. The latter analyzes the energy spectrum of the neutron beam as it scatters from the sample. Finally, the signal output is sent to a detector. The initial and final neutron energies are determined by exploiting the process of Bragg diffraction

$$n\lambda = 2d\sin\theta_S, \quad (3.3)$$

from the monochromator and analyzer single crystals. As can be seen in the triple-axis schematic diagram shown in Figure 3.1, the incoming neutron beam first strikes the monochromator, which results in a beam scattered through an angle denoted by $2\theta_M$. Thus, in order for the beam to be able to hit the sample and reach both the analyzer crystal and finally the detector, each component must be rotated by the associated crystal Bragg angle θ , and scattering angle 2θ . Thus, at each setting of the spectrometer—corresponding to specific angles at the monochromator, sample, and analyzer—a single measurement is made for a scattering vector and energy transfer.

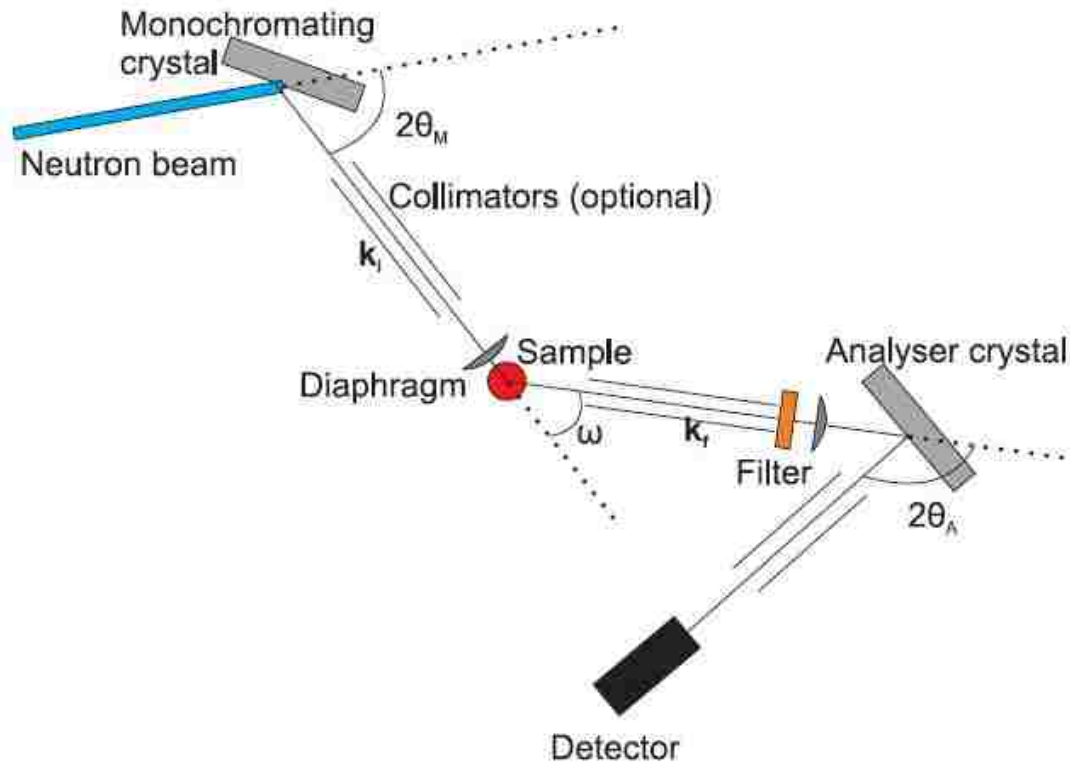


FIGURE 3.1 Schematic representation of the set up of a triple axis neutron scattering spectrometer. Reference adapted from [19].

In order to preserve the neutron flux at the desired $n = 1$ fundamental wavelength (where n represents an integer in the Bragg diffraction law) filters are placed in the path of the beam. This has the effect of removing the higher order harmonic content (i.e. noise usually referred to as $\lambda/2$, $\lambda/3$...etc.) of the diffracted neutron beam, otherwise spurious detectors counts would appear in the intensity profile. As can be seen from Figure 3.1 the filter can be placed either along the incident beam path or the scattered beam (after the sample). In the case of thermal neutrons, the most common filter used is the so-called highly oriented pyrolytic graphite, commonly

abbreviated as HOPG or simply PG for $k_i < 2.66 \text{ \AA}$ or 4.10 \AA . It is a special form of graphite (pure carbon) that acts as a single crystal along the [001] direction in reciprocal space. It is ideal to use for neutron energies of 13.7, 14.7, 30.5, and 41 meV since neutrons of other energies ($n > 1$) are mostly scattered out of the beam. Because of the very high reflectivity over a large energy range, its negligible coherent scattering and absorption cross section, and the fact that gamma ray scattering is very small due to its low atomic number, PG (usually the (002) reflection with an interplanar d spacing of 3.354 \AA) is often the single crystal of choice for both monochromators and analyzers in a TAS system. However, it is also common to find other materials such as Germanium, Copper, and Silicon used for both the monochromator and analyzer depending on the specifics of each instrument.

The next TAS component along the neutron beam is the sample. Recall from Chapter 2 that we can have different types of scattering; that is, the neutron can either lose or gain energy, in which case $E_f \neq E_i$ (inelastic scattering) or the analyzer can be set to only detect $E_f = E_i$ (elastic scattering). Thus the resulting energy transfer and the magnitude of the momentum transfer between the neutron and sample are given by

$$\hbar\omega = E - E' = \frac{\hbar^2}{8m} \left(\frac{1}{d_M^2 \sin^2 \theta_M} - \frac{1}{d_A^2 \sin^2 \theta_A} \right) \quad (3.4)$$

and

$$Q = \sqrt{k^2 + k'^2 - 2kk' \cos 2\theta}, \quad (3.5)$$

where d_M and d_A are the corresponding d -spacings of the monochromator and analyzer crystals and the magnitude of the momentum transfer is calculated by expressing the vector dot product of $\mathbf{Q} = \mathbf{k} - \mathbf{k}'$ with itself. Notice that $|\mathbf{Q}|$, is independent of the Bragg angle θ_S in equation (3.4), instead it only depends on the sample's scattering angle 2θ . It becomes clear now, that there are

two fundamental types of scans in a triple-axis experiment. One is termed as a constant- \mathbf{Q} scan, in which the momentum transfer is kept constant. If the monochromator Bragg angle is fixed, the system is in an E_i -fixed configuration. Similarly, allowing the analyzer Bragg angle to remain constant results in a E_f -fixed configuration. Typically only one of these set-ups is chosen, since the wavelength filter must be placed either before or after the sample. The flexibility of the TAS system, allows the user to be able to choose either set-up depending on the specific problem under study. On the other hand, one can perform what is referred to as a constant- E scan, for which the energy instead of the momentum transfer is held constant. The choice for each type of scan depends on the particular aspects of the physics phenomenon under investigation. However, it is very common to use the set-up with a fixed E_f . One of the advantages of such configuration is that it typically allows access to a much broader energy range and wave vector transfer within the geometric constraints of the spectrometer. Nonetheless, a combination of both scans is typically used to map out dispersion relations for both phonons and magnons.

Recall from Chapter 2 that the scattering function $S_{coh}(\mathbf{Q}, \omega)$ contains delta function of both momentum and energy. Thus in principle, once the delta function condition is met, one would expect an infinite intensity and zero intensity everywhere else. However, in real experiments, instrumental components such as the analyzer and monochromator, and even the sample itself will add experimental uncertainties to the measurement. This results in an intensity profile characterized by a finite width. The energy spread caused by the monochromator and analyzer, is due to their mosaic, which are small angular misorientations of the Bragg planes. This significantly increases the scattered intensity measured at the detector, causing both a spread in neutron energy as well as a spread in its direction. This is the reason why collimators are a necessary component of the triple-axis instrument; they improve/control the divergence of the

neutron beam, often referred to as collimation. Typically, as can be seen in Figure 3.1, collimators are placed between each of the component of the TAS, along the flight path of the neutron beam. They consist of sets of thin parallel blades coated with a strongly neutron absorbing material such as Gd_2O_3 or Cd. Just like with all of the triple axis components, the choice of what collimation to use is entirely dependent on the physics. A fine collimation, will improve the Q -resolution of the instrument, that is the full-width at half-maximum of the characteristic Gaussian peak of the crystal mosaic will be smaller in width, but will reduce the neutron count at the detector. On the other hand, a coarse collimator will have the opposite effect; it will increase the intensity of the profile at the expense of a poor Q -resolution. Thus, in order to find the right combination of collimation, a rule of thumb is to be able to match the Q -resolution of the instrument with that of the scattering under study. In addition to the use of collimators, diaphragms are also placed along the neutron beam path before the analyzer and detector in order to improve the signal-to-noise ratio that results from having a neutron beam much wider than the sample used.

Polarized Neutron Scattering Instrument Components

In systems characterized by complex interactions and coupling of the different degrees of freedom, having more than one type of neutron interaction (i.e. nuclear and magnetic) with the sample imposes a challenge when trying to isolate and characterize a single interaction. For these cases, it is important to consider that one of the main differences between nuclear and magnetic scattering is that the latter is not isotropic due to its dipolar nature (see Figure 2.6). This means that one can sort out the contributions of spin waves and phonons to the excitation spectrum (if the need ever arises) as well as separate nuclear and magnetic Bragg peaks by using a technique known as polarized neutron scattering. The latter is a variation on the basic TAS, which works

on the same principles and with the same components but has a few modifications that allow the spins of the neutron beam to be controlled.

This technique requires the use of polarizers in order to align the neutron's moments in the same direction and guide fields in order to maintain the direction of the spin and the polarization of the neutron beam. Bragg diffraction from magnetized crystals, transmission through polarized ^3He , and reflection from CoFe magnetized mirrors are some of the ways in which neutron beams are polarized; each of these aligns the neutron's moments parallel or anti-parallel to an external magnetic field. Following this logic, if the neutron's moments are parallel to the field, they are referred to as 'up' neutrons (the same idea follows for 'down' neutrons). In most cases, flippers—a device that changes the spin of the neutron from up to down and vice versa—are the common choice in order to perform polarization analysis experiments. Using this device, several combinations of 'up' to 'down', 'down' to 'up', etc., can be realized. Using the concept that the spin direction of a neutron can flip when the origin of the scattering is magnetic, i.e., if the magnetization of the sample is perpendicular to the guide field used to maintain the neutron's polarization, flippers can be inserted on either side of the sample along with polarizers in order to measure all the neutron scattering possibilities simply by turning the flipper on or off (see Figure 3.2). Thus, from spectra showing the same measurement for both neutron spin-flip and non-spin-flip, one is able to determine which peaks have a magnetic origin. Refer to Figure 3.3 for an example of such spectra taken using a polarized neutron beam incident on the sample and analyzing the final polarization state of the scattered neutrons [64]. In the non-spin-flip profile (blue curve) the quasi-elastic peaks are due to spin diffusion while the elastic peak has both nuclear and magnetic contributions. On the other hand, the difference in intensity in the spin-flip data (red curve) indicates that the inelastic signal is the result of spin wave scattering.

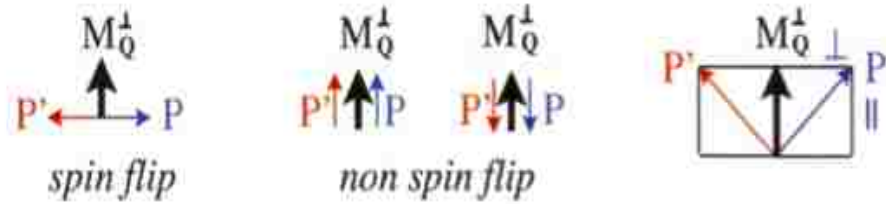


FIGURE 3.2 Schematic diagram of spin flip vs. non-spin flip processes in polarized neutron scattering. Shown are the interaction between the sample's magnetization (M) and the neutron's polarization (P); the spin direction of a neutron and not its magnitude can be flipped or (not) depending whether the magnetization of the sample is \perp or \parallel to the guide field used to maintain the neutron's polarization. Image adapted from [19].

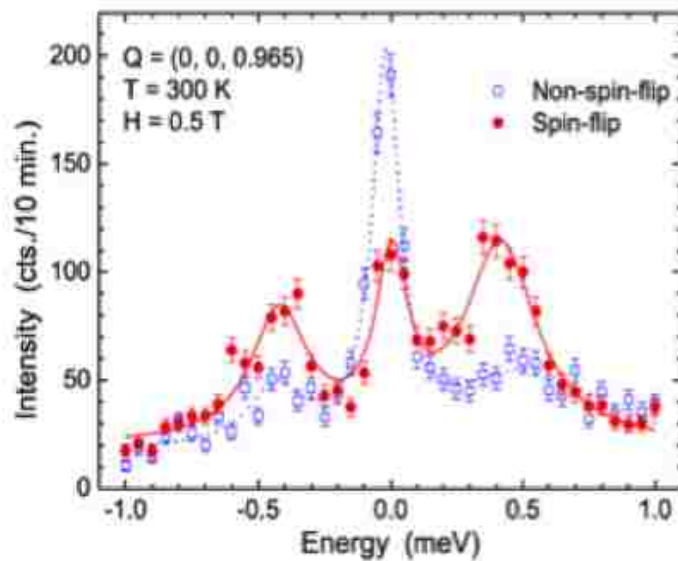


FIGURE 3.3 Non-spin flip (blue) and spin flip (red) of the spin wave excitation spectrum for the CMR manganite system $\text{La}_{0.70}\text{Ca}_{0.3}\text{MnO}_3$. Figure was adapted from [64].

Resolution Functions in Triple-Axis Spectroscopy

For a given configuration of a triple-axis instrument, the instrumental resolution is usually expressed as a four-dimensional function of both energy $\hbar\omega$ and momentum transfer \mathbf{Q} , denoted by $R(Q - Q_0, \omega - \omega_0)$ [65] and is always calculated by computer. Since the surface of constant probability has a different length for each of the dimensional axis, the resolution function is often referred to as the resolution ellipsoid. Typically, unless one is wanting a direct comparison between the measured and theoretical scattering function $S(\mathbf{Q}, \omega)$, there is no need to account for the effects of the finite instrumental resolution right away while performing a measurement. Nonetheless, the intensity at the detector is well described by a convolution of the resolution function with the scattering function. To place the instrumental resolution in context, a TAS with a configuration consisting of a PG monochromator and analyzer, a fixed final energy of 14.7 meV, has typical values of the instrumental resolution given by $\Delta Q \sim 0.002 \text{ \AA}^{-1}$ and $\Delta E \sim 1 \text{ meV}$ for the wave vector and energy, respectively. These practical considerations are important to consider since they affect the scientific interpretation of the data. For example, the energy resolution value given above indicates that any process with a lifetime $\tau > 7 \text{ ps}$ (from Heisenberg uncertainty principle) appears to be static. Similarly, as a consequence of the finite instrumental resolution for ΔQ , any length scale/ correlation length $\xi > 500 \text{ \AA}$ will appear to be infinite/long range.

HB-1A Fixed-Incident Energy Triple-Axis Spectrometer

This spectrometer is a fixed-incident energy (14.6 meV) TAS located at the HFIR at ORNL. It is designed to use a double PG graphite monochromator system. The first one being vertically focused while the second one has the option of being adjusted to be either vertically or horizontally focused. Filters of PG are also used after each monochromator in order to reduce

higher order $\lambda/2$ contamination. This particular arrangement of filters and double monochromator system makes this instrument one of the cleanest in terms of higher order contamination at the HFIR and also provides an essential gain of neutron flux and a very low background that proved to be crucial for our Mn-substituted Ruthenium oxide experiments. Thus, HB-1A is ideal for the measurement of weak magnetic scattering of very small single crystals with masses $m > 2$ mg, and also of thin film samples. This instrument set-up also allows the use of an extensive array of collimations (FWHM) from the premonochromator, monochromator-to-sample, sample-to-analyzer, and analyzer-to-detector that can be tuned to match the Q resolution of the physics investigated. It has various choices for the single crystal analyzers; the PG (002) allows for an energy resolution of ~ 1 meV while the choice of Be (101) reduces the energy resolution width to ~ 0.5 meV. The detector is that of a single ^3He gas counter and the momentum range that can be probed in reciprocal space in the elastic configuration ranges from 0.2 to 4.9 \AA^{-1} .

HB-1 Polarized Triple-Axis Spectrometer

The HB-1 Polarized Triple-Axis Spectrometer located at the HFIR at ORNL is optimized specifically for inelastic scattering at intermediate energies. That is, for the investigation of spin waves in ordered magnetic materials as well as for spin and lattice excitations in high-temperature superconductivity, colossal magnetoresistance materials, and multiferroic systems. The HB-1 features vertical beam focusing and a high time-averaged flux, which makes it ideal for studies of small samples and weak scattering. Thus, we used this instrument for elastic measurements of the CMR manganite PCMO 30, 35, and 40 as well as well as for the inelastic investigation of spin-lattice coupling in the LCMO 20 system. The HB-1 monochromator provides only PG (002) single crystal choice in the unpolarized fixed vertical focus monochromator while giving three choices (PG (002), Be (101), and Si (111)) for the

unpolarized fixed vertical focusing configuration of the analyzer. All experiments were carried out on a fixed-final energy configuration with neutrons detected through a single ^3He gas counter with an elastic resolution of about 5-10% of E_i . Several combinations of collimation were used in order to adjust the instrumental resolution. Although not used for the work presented on this thesis, the main advantage of this TAS is the capability of performing polarized neutron scattering experiments for studies of excitations, phase transitions, etc.

HB-3 Triple-Axis Spectrometer

This Triple-Axis Spectrometer located at the end of the beam tube at the HIFR at ORNL has very similar features and applications as that of the HB-1 described above, excluding the capability to perform polarization analysis. Thus, this instrument was also chosen for the elastic experiments of the doping dependence of phase segregation in the PCMO 30, 35, and 40 systems. Specifically, it is designed for inelastic measurements on single crystals over a wide range of energies (up to 100 meV) and momentum transfers. There are three crystal choices for both the monochromator and analyzer in the fixed-vertical focusing configuration: PG (002), Be (002), and Si (111). Out of these monochromator choices, PG (002) is used for experiments in which a higher neutron intensity is desired while Be (002) is used for better energy resolution at higher energy transfers. As in the case of the HB-1 TAS, all experiments were carried out on a fixed-final energy configuration with neutrons detected through a single ^3He gas counter with an elastic resolution of about 5-10% of E_i adjustable through the use of collimators.

BT-7 Double-Focusing Triple-Axis Spectrometer

The BT-7 Double-Focusing Triple-Axis Spectrometer system at the NIST center for Neutron Research in Washington, DC was used for complimentary elastic measurements of PCMO 30, 35, and 40. In order to allow for the tuning of the resolution and intensity of the beam, BT-7 has the

choice of either Cu (220) or PG (002) doubly focusing monochromator crystals as well as a PG filter in reactor beam remotely insertable and tunable. This set-up allows for energies in the range of 5 – 500 meV and as far as much as an order-of-magnitude gain of neutron flux compared to spectrometers at the HFIR at ORNL, that is, well into the 10^8 n/cm²/s range. The instrument is equipped with ³He cells, built-in guide fields, and insertable spin rotators for polarized neutron analysis. The analyzer system can be operated in two different configurations, one with a multi-strip of PG (002) in a horizontally focused mode or instead one in which the PG analyzer is flat with a linear position sensitive ³He detector or with conventional Söller collimators of 10', 25', 50', and open at each position [66].

BT-9 The Multi-Axis Crystal Spectrometer

The Multi-Axis Crystal Spectrometer at the NIST Center for Neutron Research is a third generation cold neutron spectrometer that provides ultra high sensitivity access to dynamic correlations in condensed matter on length scales ranging from 0.1 nm to 50 nm and energy scales from 2.2 meV to 20 meV. The instrument is equipped with a large doubly focusing monochromator that provides a high neutron flux of 5×10^8 n/cm²/s at the sample location (area of 2cm x 4 cm). A focusing super-mirror guide placed between the monochromator and sample, further enhances the flux (~ 20%) at the sample location. The energy resolution varies from 0.02 to 1.4 meV (FWHM), depending on the radial collimator used. The choices for the analyzers are vertically focusing PG (002) (the highest detection efficiency) Cooled Be, BeO, and HOPG filters, and 90' collimators before the analyzers. Forty ³He detectors (20 spectroscopic and 20 diffraction), detect the scattered neutrons. What sets apart this TAS instrument from others is that it is characterized by a detection efficiency gain higher than an order of magnitude from that of other conventional triple-axis spectrometers.

3.4 Single Crystal Diffractometers

Two single crystals diffractometers were used to acquire diffraction patterns over a wide range of scattering angles permitting the refinement of the magnetic structure and the calculation of the average ordered moment using the Rietveld refinement package *FullProf* [67 - 70]. The magnetic refinement process was one that included several steps. First, the integrated magnetic intensities of the observed reflections were calculated by subtracting the background and later corrected by the Lorentz factor. Subsequently, absorption effects were taken into account and the intensities of symmetrically equivalent reflections were averaged. These steps yielded a set of structure factors, which were later used to perform a least square refinement of the symmetry allowed magnetic structure. Experiments were conducted on the Mn-doped Ruthenates (SRMO 11 and 16 %) single crystals on the US/Japan Wide-Angle Neutron Diffractometer (WAND) with complimentary measurements taken at the Four Circle-Diffractometer. Both instruments are located at the High Flux Isotope Reactor (HFIR) at Oak Ridge National Laboratory (ORNL) on the horizontal beam lines (HB)-2C and HB-3A, respectively. In terms of Instrument components, the main difference between the TAS and single crystal diffractometers is that the latter lacks the energy analyzer, which permits the measurement of the neutron's energy change during the scattering process.

HB-2C US/Japan Wide-Angle Neutron Diffractometer

Figure 3.4 shows the schematic diagram of HB-2C WAND at the HFIR at ORNL. Thermal neutrons needed for this instrument are produced in the reactor and moderated by H₂O. An arrangement of several Germanium crystals is used for monochromating the white beam. The fixed wavelength for this diffractometer ($\lambda = 1.48 \text{ \AA}$) is selected from the (111) Bragg reflection of the Ge monochromator crystals. The monochromator angle is fixed and has a value of

$2\theta_M = 52.0^\circ$. The single crystal samples were enclosed in a cylindrical vanadium can and subsequently mounted inside a standard orange HFIR-cryostat and a cryofurnace used for regulating the temperature in-between 5- 150K. The neutrons diffracted by the sample were collected with a curved, one dimensional ^3He position-sensitive detector covering 125° of the scattering angle with a focal distance of 71 cm.

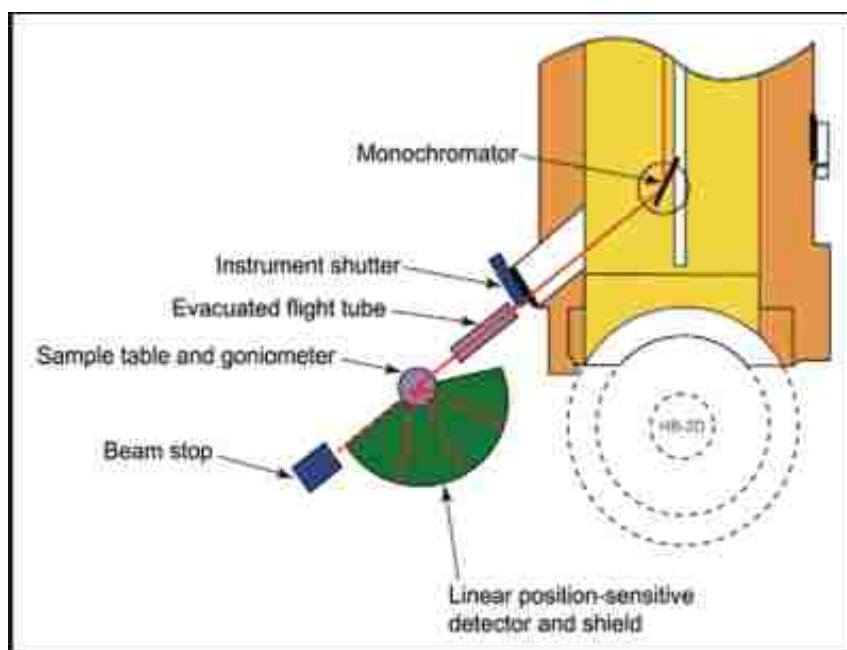


FIGURE 3.4 Schematic diagram of the HB-2C US/Japan Wide-Angle Neutron Diffractometer located at the HFIR at ORNL.

One of the advantages of this instrument is that it offers the possibility of tilting both the sample and detector into a flat-cone geometry mode, which allows for the fast measurements of single crystal diffraction patterns over a wide range of reciprocal space. The WAND detector (ORDELA 1410N) is a multi-anode type consisting of a total of 624 anodes, separated by 0.2° . It is a custom designed ^3He gas counter with an intrinsic angular resolution of 0.25° and a maximum counting rate per anode of 10^4 counts/sec. This particular instrument configuration

only allows the use of coarse collimators before the detector. For the case of SRMO 16 and 11% due to the small size of the crystal, coarse collimation was convenient since it increased the intensity of the profile facilitating the detection of weak magnetic peaks.

HB-3A Four-Circle Diffractometer

Complimentary studies were performed on the Four-Circle Diffractometer HB-3A located at the HFIR at ORNL. Figure 3.5 (left) shows the set-up of the four-circle diffractometer, where the labels for the shutter, goniometer, detector, and beam stop are added for clarity. This diffractometer was used for high-resolution measurements of the antiferromagnetic peaks in Mn-substituted SRO 327, which was possible through the tuning of the horizontal bending of the monochromator.

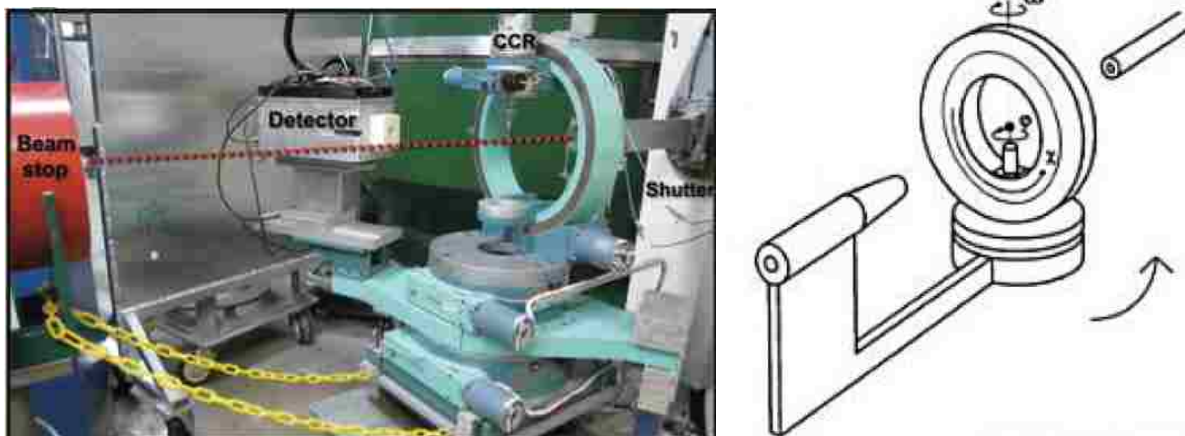


FIGURE 3.5 The HB-3A Four-Circle Diffractometer at the HFIR. (Left) Actual set up of the Four-Circle Diffractometer on HB-3A at the HFIR at ORNL. (Right) Schematic sketch of the Eulerian cradle that carries the single crystal in the diffractometer showing the motion along χ and ϕ . Adapted from [19].

The geometry of this instrument consists of a monochromator, a centric Eulerian cradle that orients the crystal relative to the neutron beam, and a ^3He detector with a 7-anode array in a honeycomb pattern. The fixed-monochromator of 48° is a horizontal focusing Silicon-(220)

crystal, selecting an incident neutron wavelength of $\lambda = 1.536 \text{ \AA}$. As can be seen in the picture, the detector can be moved independently to the Eulerian cradle (for clarity, a schematic diagram of the cradle is shown on Figure 3.5 (right)) along the horizontal direction. Thus, defining the scattering angle for a range $2\theta < 155^\circ$. The incident flux on the sample is up to $2.2 \times 10^7 \text{ n/cm}^2/\text{s}$, allowing for a crystal size requirement greater than 1 mm^2 , which is exposed to a beam size of $5 \times 5 \text{ mm}^2$. The single crystal sample is mounted on the goniometer, which has a full χ circle with a 4K-closed cycle helium refrigerator for temperature measurements ranging from 5 – 100 K. In order to orient the crystal in any direction, two motions are available: the χ motion along the vertical circle and the ϕ motion about the axis of the crystal support itself. Full control of the Eulerian cradle is given by the ω -rotation, which is the motion about the axis of the entire cradle itself. These four angles (2θ , χ , ϕ , and ω) are sufficient to align the sample along any particular reciprocal point in space. Data acquisition and diffractometer control is all provided by a user-friendly PC interface.

Chapter 4

Magnetic Structure of $\text{Sr}_3(\text{Ru}_{1-x}\text{Mn}_x)_2\text{O}_7$ ($x = 0.125, 0.16$)

4.1 Introduction

Pioneering work on $\text{Sr}_3(\text{Ru}_{1-x}\text{Mn}_x)\text{O}_7$ by Mathieu and colleagues [46] has shown that partial substitution of Mn for Ru at the B-site in $\text{Sr}_3\text{Ru}_2\text{O}_7$ (SRO327) induces a complex AFM order with concentrations of Mn starting as low as 5%. Shown in Figure 4.1 is the latest reported phase diagram from Biao Hu *et. al.* . Within this unique regime in the phase diagram (i.e. the long-range antiferromagnetic insulating (LR-AFM-I) ground state), the nature of the induced magnetic order and its relevance to the magnetic properties in the parent compound are yet to be elucidated [45, 71].

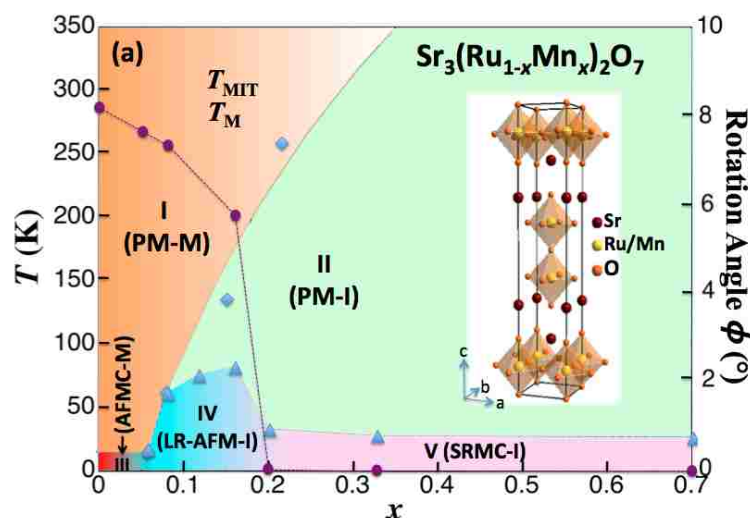


FIGURE 4.1 A schematic representation of the latest reported phase diagram for various substitution concentrations (x) of the $\text{Sr}_3(\text{Ru}_{1-x}\text{Mn}_x)_2\text{O}_7$ series. Region I is a paramagnetic metallic (PM-M) phase; II a paramagnetic insulating (PM-I) phase; III a metallic phase with AFM correlation (AFMC-M); and IV a long-range AFM insulating phase (LR-AFM-I). Region V is an insulating phase characterized by short-range magnetic correlations (SRMC-I). The right axis indicates the x dependence of the rotation angle ϕ of the (Ru/Mn) O_6 octahedron at 90 K. The schematic diagram of the unit cell representation of $\text{Sr}_{n+1}\text{Ru}_n\text{O}_{3n+1}$ in an $I4/mmm$ configuration is shown in the inset. Both figures adapted from [1].

Motivated by these studies cited above, we report in this study a comprehensive single-crystal elastic neutron scattering investigation of the magnetism in Mn-substituted $\text{Sr}_3(\text{Ru}_{1-x}\text{Mn}_x)\text{O}_7$ ($x = 0.125$ and 0.16) (SRMO16) (SRMO12.5). Our main goal and objective for this work was to provide detailed insight into the complex AFM phase reported at low- T by fully characterizing the magnetic structure in the ground state and its evolution as a function of temperature.

4.2 Properties of $\text{Sr}_3(\text{Ru}_{1-x}\text{Mn}_x)_2\text{O}_7$ ($x = 0.16$)

To begin our studies, the 16 % concentration of Mn was chosen since it is on the borderline between quite different regions of the phase diagram, lying in a unique regime where a long-range antiferromagnetic insulator ground state had been previously reported in the phase diagram. To begin, notice that on the right axis of the phase diagram in Figure 4.1, the rotational distortion of the RuO_6 octahedra present in the parent compound gradually diminishes with Mn substitution and drops suddenly to zero for $x > 0.16$. These structural changes coupled to the fact that the Ru/Mn sites are located inside the oxygen octahedra (thus subject to the crystal field effect) greatly alter the electronic and magnetic structure of these materials, as it was discussed in Chapter 1. In addition, unique features of this particular doping concentration can be found on Figure 4.2, where the physical property measurements of $\text{Sr}_3(\text{Ru}_{1-x}\text{Mn}_x)\text{O}_7$ ($0 < x < 0.7$) reported in the work of Biao Hu and collaborators [45] are displayed. Starting from the top panel, we see evidence indicating that the onset of magnetic ordering is accompanied by a dramatic increase of the in-plane resistivity, $\rho_{ab}(T)$, (Figure 4.2 (a)) indicating that the insulating behavior is enhanced by the development of magnetism. The derived Curie-Weiss temperature shows a cross over from AFM to FM ordering at $x \sim 0.16$ for the in-plane susceptibility (shown in Figure 4.2 (b)), while the c -axis susceptibility still favors AFM (not shown on this plot).

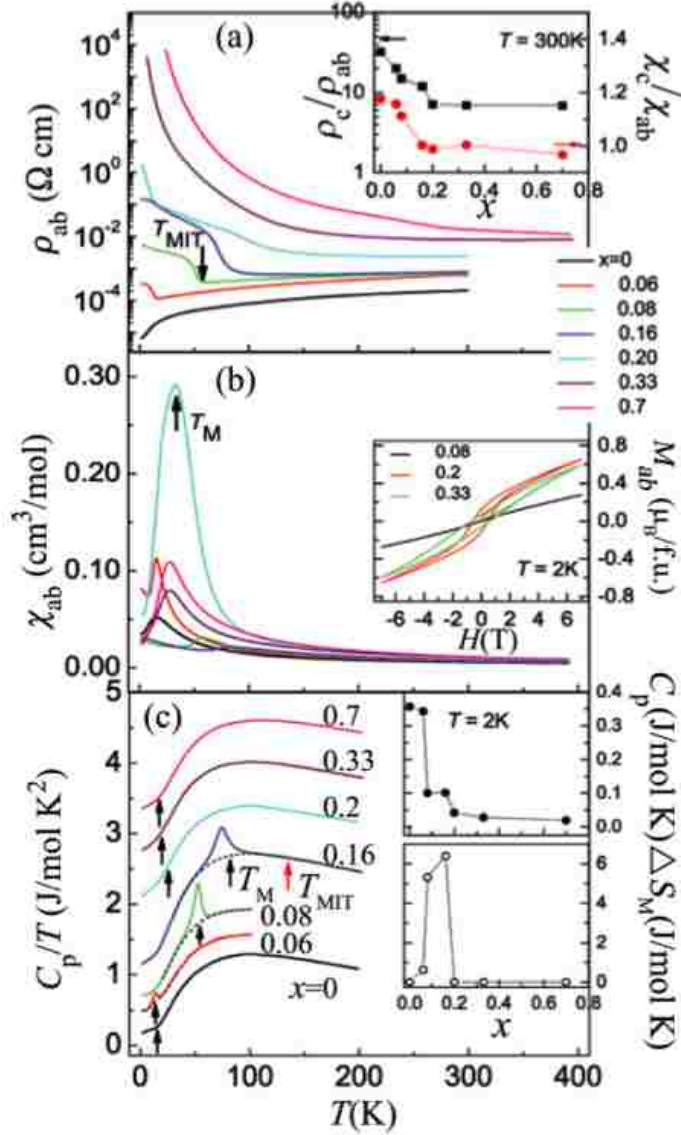


FIGURE 4.2 Physical property measurements of $\text{Sr}_3(\text{Ru}_{1-x}\text{Mn}_x)\text{O}_7$ ($0 < x < 0.7$). (a) Temperature dependence of the $\rho_{ab}(T)$ as a function of doping concentration. The arrow indicates the metal-to-insulator transition temperature for $x = 0.08$. The inset shows the plot of the ratio of both $\rho_{ab}(T)/\rho_c(T)$ and $\chi_{ab}(T)/\chi_c(T)$ at 300 K as a function of x . (b) shows the in-plane magnetic susceptibility $\chi_{ab}(T)$ measurements for all doping concentrations while the inset reports the behavior of (M_{ab}) vs. field (H). (c) shows the dependence of the specific heat normalized by the T , $C_p(T)/T$ vs T , where the black arrows indicate the ordering temperature for each concentration while the dashed line represents the polynomial background fit. The insets of (c) show $C_p(T)$ and ΔS_M as a function of x , respectively [45].

The FM character for $x > 0.16$ is depicted by the in-plane magnetization (M_{ab}) vs. field (H) plot in the insert of Figure 4.2 (b)). Panel (c) shows evidence that at this Mn concentration 1) the transition temperature (T_M) for AFM ordering reaches a maximum value, 2) there is a distinctive anomaly in the specific-heat measurements, which indicates that this is a true second-order phase transition, and 3) a maximum value for the extracted entropy ΔS_M is obtained. Thus, it is evident that 16% Mn substituted SRO327 is on the borderline between quite different regions of the phase diagram. Indeed, the data presented here shows that these circumstances lead to an unusual in-plane E -type AFM spin configuration with moments ferromagnetically aligned along the c axis and with only one single bilayer ordering in the c direction.

4.2.1 Experimental Details

Single crystals of SRMO16 were grown by the floating zone method and subsequently characterized by single-crystal X-ray diffraction and physical property measurements (ppms) [45]. All single crystals used have mosaics spreads of about 1° and masses up to 1.63 grams. The schematic crystal structure shown in the inset of Figure 4.1 (displayed in space group $I4/mmm$ for simplicity purposes) of the $n = 2$ member of this layered perovskite series consists of two layers of RuO_6 corner-sharing octahedra separated by SrO planes. The resulting crystal structure of this system has been analyzed using neutron powder diffraction [40] and it has been shown to be consistent with that of space group Pbn with lattice parameters $a = b = 5.50(1) \text{ \AA}$ and $c = 20.72(1) \text{ \AA}$. In this setting, all atoms retain an $I4/mmm$ configuration [72], with the exception of the oxygen atoms that form the RuO_2 layers. The resulting crystal structure is characterized by an alternating rotation ($\sim 7^\circ$) of the neighboring-corner sharing RuO_6 octahedra with respect to each other around the crystallographic c -axis.

Neutron diffraction experiments on SRMO16 were carried out at the High Flux Isotope Reactor (HFIR) at Oak Ridge National Laboratory. The single crystal samples were enclosed in a cylindrical vanadium can and subsequently mounted inside a standard orange HFIR-cryostat and a cryofurnace was used for regulating the temperature. The triple-axis spectrometer on HB-1A was configured with a PG (002) analyzer for both the monochromator and analyzer with a fixed incident neutron wavelength of 2.359 \AA ($E_i = 14.62 \text{ meV}$). Collimations of $48'48' - \text{sample} - 40'60'$ were used prior to the monochromator, between the monochromator and sample, sample and analyzer, and analyzer and detector, respectively. Measurements on the US/Japan Wide Angle Neutron Diffractometer (WAND) installed at the beam port HB-2C at HFIR were taken with collimations of $48'40' - \text{sample} - 40'120'$ and a Ge (111) single crystal for the monochromator was used to produce an incident neutron with a wavelength of 1.48 \AA . And finally, the fixed wavelength ($\lambda = 1.536 \text{ \AA}$) for the HB-3A Four-Circle Diffractometer measurements was selected from the (220) reflection of Silicon. The chosen collimations for this particular diffractometer set up were those of $48'40' - \text{sample} - 40'120'$. We index all diffraction peaks following the orthorhombic unit cell notation. The wave vector $\mathbf{Q} = (Q_x, Q_y, Q_z)$ is in units of \AA^{-1} and $(H, K, L) = (Q_x a / 2\pi, Q_y a / 2\pi, Q_z a / 2\pi)$ is in reciprocal-lattice units (r.l.u).

4.2.2 Magnetic Structure

Our measurements show that magnetic order in SRMO16 has a characteristic wave vector given by $\mathbf{Q}_M = (0.5, 0, 0)$, in agreement with that previously reported for 5 % from powder neutron diffraction experiments [46]. The Bragg intensity (I_B) of the observed magnetic superlattice peak $(0.5, 0, 0)$ is a measure of the square of the staggered magnetization of the system (M)², which serves as the order parameter. The T -dependence of the order parameter is illustrated in Figure

4.4 and inset; this plot indicates that the AFM transition temperature (T_N) \sim 78 K, which is consistent with magnetic susceptibility measurements [45].

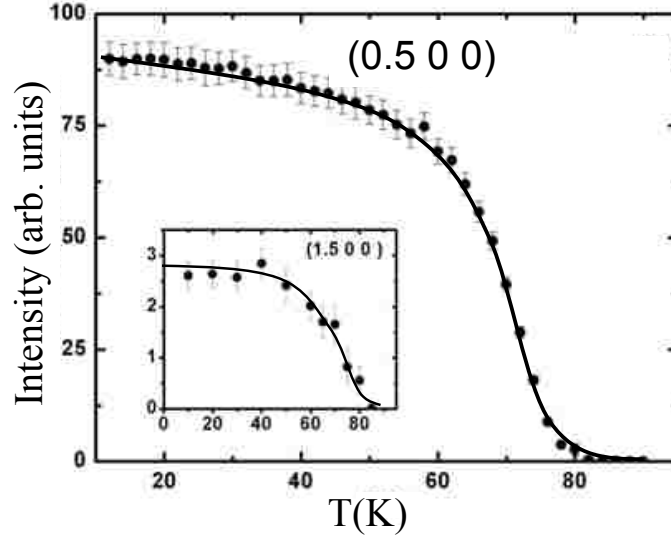


FIGURE 4.3 T -dependence of the integrated magnetic scattering intensity at chosen AFM Bragg peaks for the $\text{Sr}_3(\text{Ru}_{0.84}\text{Mn}_{0.16})_2\text{O}_7$ taken with the HB-1A triple-axis spectrometer. Adapted from [1].

In order to determine the spin configuration, neutron diffraction profiles on single crystals of SRMO16 were taken with the WAND; they are presented in Figure 4.4. Figures 4.4(a) and 4.4(b) show the contour plot of diffraction patterns (intensities in logarithmic scale) for $T = 100$ K and 10 K in the $(H, K, 0)$ scattering plane, respectively. Figure 4.4(a) displays the diffraction pattern at $T > T_N$. The nuclear Bragg peaks appear at the reciprocal lattice positions $(hk0)$ that satisfy the $h + k = 2n$ (n integer) diffraction condition for this symmetry. The less intense peaks present in the diffraction pattern not satisfying the higher $I4/mmm$ space group conditions indicates the lowering of the symmetry to Pbn space group which originates from the rotations of the RuO_6 octahedra about the c axis [40, 41, 73]. The diffraction pattern shown in Figure 4.4(b), which was taken at the base temperature ($T = 10$ K), includes both nuclear and magnetic scattering. The

magnetic peaks at \mathbf{Q}_M and equivalent positions are present in the low-Q region at $T = 10$ K. Since our sample is 90° twinned in the ab plane, magnetic reflections at $\mathbf{Q} = (0, 0.5, 0)$ and equivalent positions are also present in the diffraction pattern.

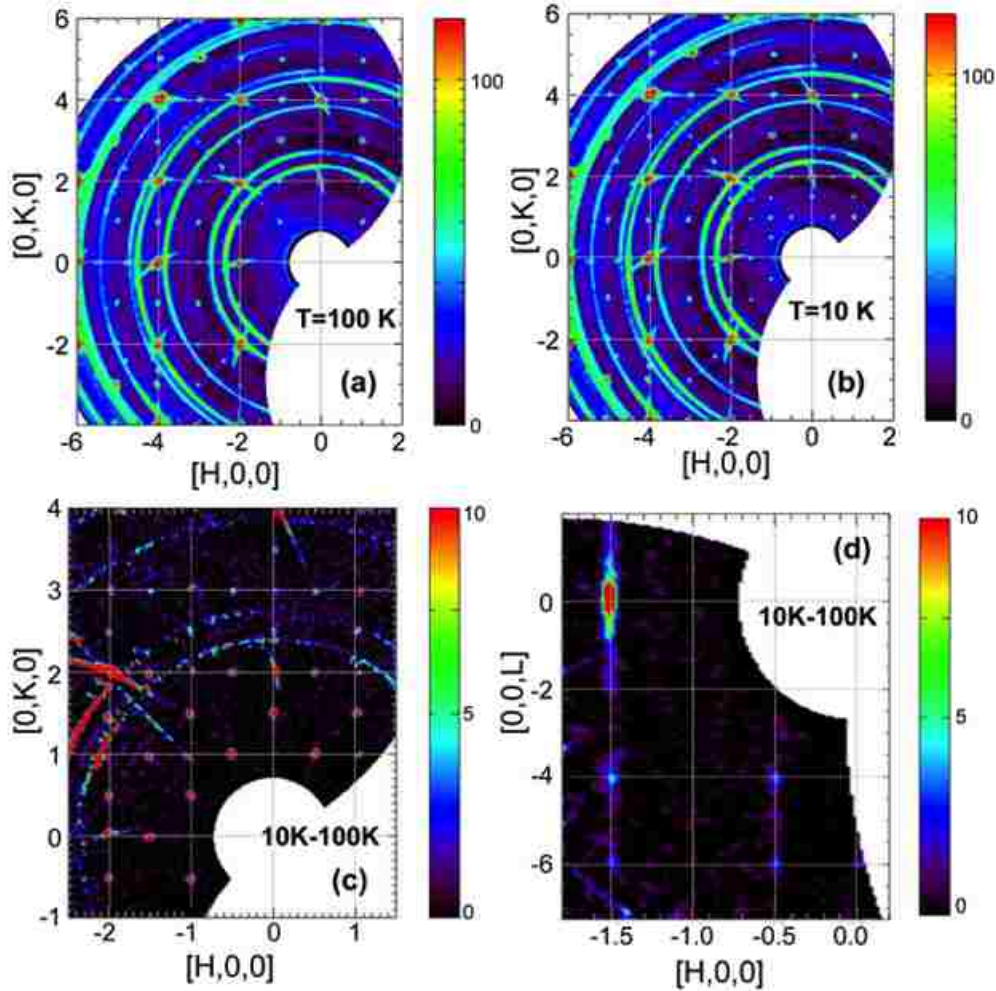


FIGURE 4.4 Neutron diffraction patterns of SRMO 16 in the $(H, K, 0)$ and $(H, 0, L)$ reciprocal planes for temperatures above and below T_N . The color bars represent the intensities in counts per 5 mins and the powder rings observed are those of the Aluminum. The raw data reported on the top panel (on a logarithmic scale) show (a) the structural peaks at $T > T_N$ and (b) the combination of both structural and magnetic peaks at $T < T_N$. Peaks are indexed using the orthorhombic notation (see text). The differential diffraction patterns at $T = 10$ K from $T = 100$ K is shown in (c) and (d) where the studied magnetic Bragg peaks observed at the base T are zoomed in for clarity [1].

The exact structure of the spin order in the low- T AFM phase can be unambiguously identified from these single-crystal diffraction results. Figure 4.4(c) shows the expanded difference scattering pattern (intensity image in linear scale) between low- T AFM phase [Figure 4.4(b)] and PM phase at 100 K [Figure 4.4(a)], displaying only the magnetic diffraction peaks. Constrained by the orthorhombic symmetry of the lattice structure, there are only two high-symmetry AFM spin structures which can be used to describe the observed low- T magnetic diffraction patterns in the ab plane: the so-called CE - and E -type AFM structures. Our analysis indicates that the absence of the $(0.5, 0.5, 0)$ -type magnetic diffraction peaks excludes the CE -type AFM ordering. Furthermore, the magnetic propagation wave vector \mathbf{Q}_M indicates the doubling of the chemical unit cell along either a - or b -axis direction, which is suggestive of the zigzag chains of the E -type structure. Extensive data collection along high symmetry scattering planes has excluded the possibility of other spin ordering patterns. While neutron powder diffraction [46] and recent resonant elastic soft X-ray scattering [47] studies have proposed the E -type AFM order in the ground state, neither of the previous work provided a clear conclusion and both stated the need for a thorough diffraction study, like the one presented here.

Having identified the spin texture in the ground state of the system, the question remains as to what are the orientation and the dimensionality of the spins. In this context, Figure 4.4(d) yields the first clue regarding the spin orientation; it displays the differential magnetic diffraction pattern in the $(H, 0, L)$ plane, showing the much stronger intensity for $(1.5, 0, l \sim 0)$ diffraction peak compared to that of the $(0.5, 0, l)$ peaks. This drastic difference in intensity indicates that magnetic moments are not aligned along the ab -plane but are parallel to the c -axis, since neutrons can only couple to magnetic moments perpendicular to \mathbf{Q} . Otherwise, one should expect zero intensity at $(1.5, 0, 0)$ Bragg point in Fig. 2(d) since the magnetic scattering intensity is

proportional to $\mathbf{Q} \times (\mathbf{S} \times \mathbf{Q})$ where \mathbf{S} is the moment and \mathbf{Q} is the wave vector transfer. Figure 4.4(d) also yields relevant information regarding the dimensionality of the ground state of this system. To understand this, recall that the integrated intensity for a magnetic Bragg reflection with moments aligned along the c -axis is given by [58]:

$$I \propto |F_M(\mathbf{Q})|^2 \left[1 - \left(\frac{L}{Q}\right)^2 |M_c|^2 \right] \cos^2(\pi zL), \quad (4.1)$$

where $|F_M(\mathbf{Q})|^2$ represents the Ru form factor and $z \sim 0.2$ is the reduced distance between the RuO₂ planes in the bilayer. The term enclosed in parenthesis is the polarization factor that unambiguously allows us to detect the direction of the moments, which as explained previously its only term is the out-of-plane magnetic component since the moments are aligned along the c -direction. The cosine squared modulation term is not only responsible for the observed Bragg peaks at even values of L for peaks $(1.5, 0, l=2n)$, but also for the variation of the intensity of such peaks, where the next strong peak that appears in Figure 4.4(d) is at $L=4$. Therefore, the scattering pattern presented in Figure 4.4(d) shows that there is some modulation along the c -direction, which is an indication of the layered nature of the magnetic structure in the ground state of this system.

In order to further investigate the dimensionality of the spin order in SRMO16, we systematically characterized both the in plane $(H, K, 0)$ and out-of-plane $(H, 0, L)$ magnetic correlations from T -dependent line profiles of superlattice peaks. Figure 4.5(a) displays the representative H scans across the $(0.5, 0, 0)$ magnetic peak in reciprocal space at various temperatures. Similarly, Figure 4.5(b) presents L scans across the $(1.5, 0, 0)$ peak shown in Figure 4.4(d). The narrow (resolution limited) linewidth of the H scans across the $(0.5, 0, 0)$ peak at low temperatures is indicative of long-range AFM ordering in the basal plane. The L scans across the $(1.5, 0, 0)$ magnetic peak on the other hand exhibit very broad Lorentzian-profiles [see

Figure 4.5(b)] even at low temperatures, indicating short-range AFM correlations along the c -axis. The extracted c -axis magnetic correlation length $\zeta(T)$ shown in the insert of Figure 4.5(d) shows only a maximum value of $\zeta \sim 5\text{-}6 \text{ \AA}$ bellow T_N . Given that the average value of the Ru-O apical distance is 2.021 \AA [40, 45], this is a clear indication that the magnetic correlation along the c -axis is exclusively restricted to the bilayered-block of the RuO_6 octahedra, which as Figure 4.1 shows, is only half of the unit cell. Thus, the ground state in this bilayered perovskite system is characterized by a single sheet of spins antiferromagnetically ordered in a zigzag chain pattern along the ab -plane. This is similar to the case of $\text{Sr}_3(\text{Ru}_{1-x}\text{Ti}_x)_2\text{O}_7$ ($x=0.4$) in which the Ti-induced incommensurate spin-density wave ordering cannot be considered to be three-dimensional due to the finite correlation length along the c -direction [74].

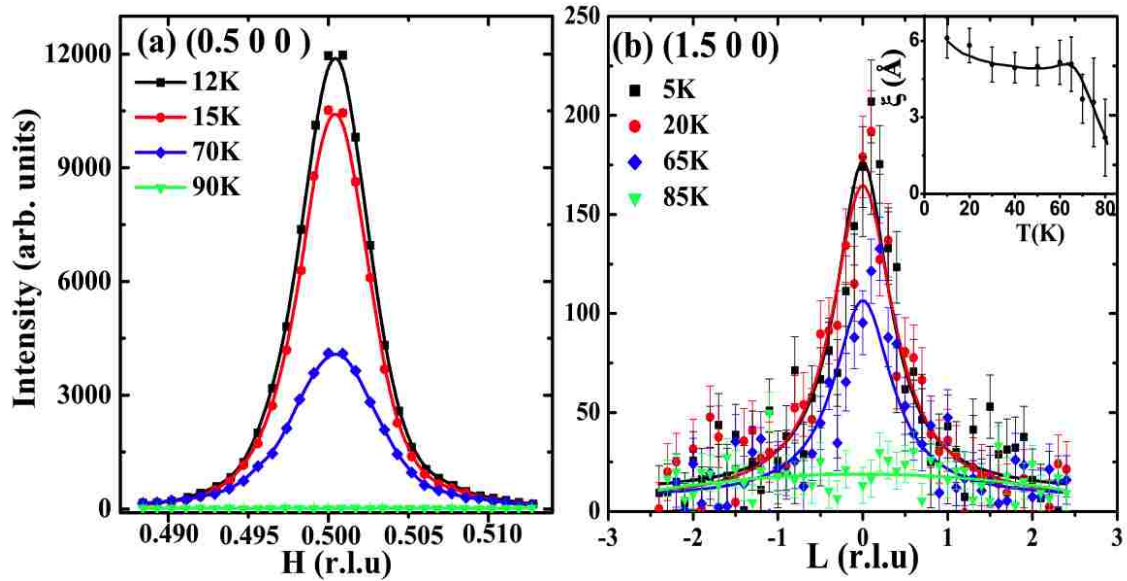


FIGURE 4.5 Neutron diffraction profiles at magnetic Bragg peaks. (a) $(0.5, 0, 0)$ in the $(H, K, 0)$ and (b) $(1.5, 0, 0)$ in the $(H, 0, L)$ scattering planes. The narrow (resolution limited) linewidth of the H scans is indicative of long-range AFM ordering in the basal plane while the very broad Lorentzian-profiles of L scans indicate short-range AFM ordering (see inset on Figure 4.4(b)) along the c -axis. The solid lines guides to the eye [1].

We argue that the Mn-induced magnetic structure is an *unusual* quasi-2D structure. A preliminary fit (i.e. we did not correct for the critical scattering contribution) of the I_B —which is proportional to M^2 —to the power-law scaling function $(1 - T/T_N)^{2\beta}$ resulted in a value of ~ 0.30 for the critical exponent β (see Figure 4.6). This value deviates from the expected value (~ 0.125) for 2D magnetism [75]. Although more detailed measurements would be required in order to obtain the precise value of β , our results are sufficient to indicate that such a Mn-induced 2D magnetic behavior cannot be explained by existing theory such as the 2D Ising model.

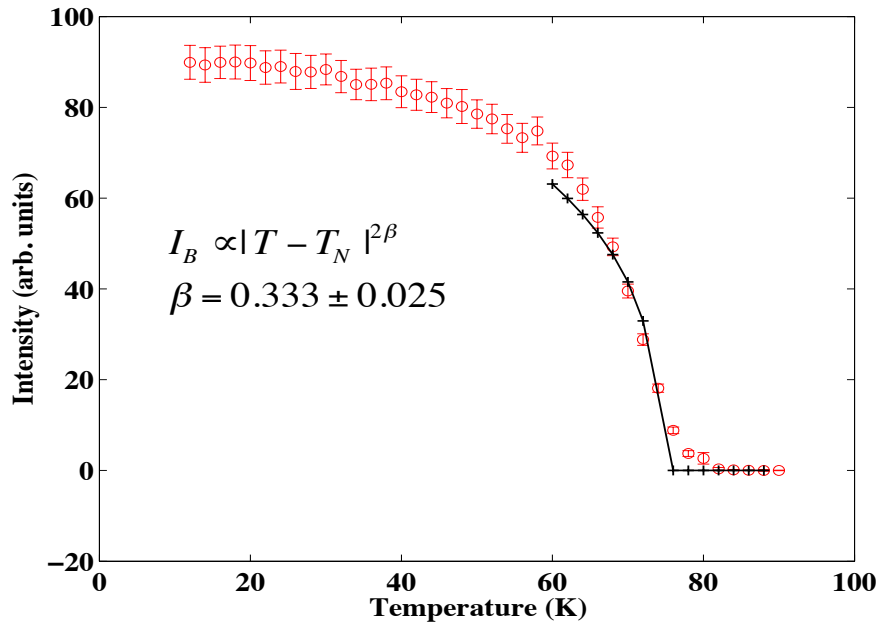


FIGURE 4.6 Fit of the Bragg intensity, I_B , in arbitrary units vs. Temperature of the magnetic superlattice peak (0.5, 0, 0) to the power law scaling function. In this plot we did not correct for the critical scattering contribution.

Finally, Figure 4.7 presents a schematic diagram of the Mn-induced SRMO16 spin structure in the bilayer block resulting from our *FullProf* magnetic refinement of the low- T neutron diffraction data. Our analysis revealed that: 1) the symmetry allowed magnetic structure with moments aligned along the c -direction provide the best description of the data; 2) the spins are

coupled ferromagnetically within the bilayer and antiferromagnetically along the basal plane; and 3) an upper limit value of $\sim 0.70 \mu_B/(\text{Ru/Mn})$ for the average ordered moment is obtained from the integrated magnetic scattering intensities.

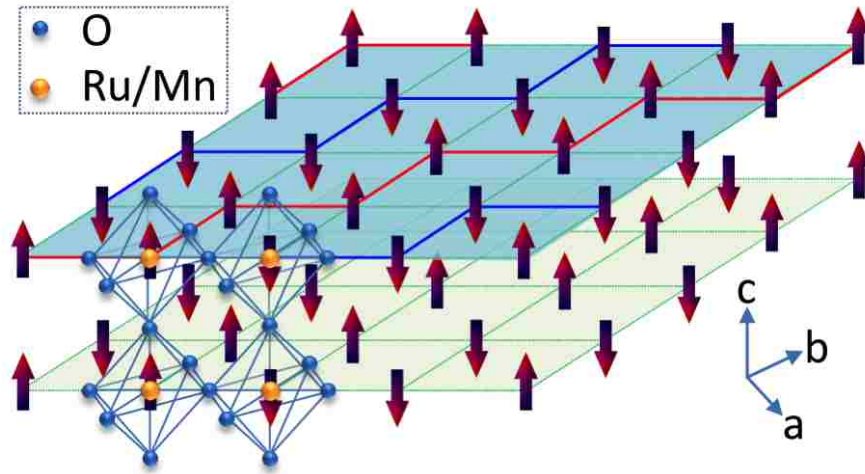


FIGURE 4.7 Schematic *E*-type AFM spin configuration in the ground state of SRMO 16 resulting from a magnetic refinement. The single bilayer-magnetic structure of the $(\text{Ru/Mn})\text{O}_6$ octahedra is displayed where the zigzag chains of the *E*-type AFM order are marked with solid lines. Two un-equivalent spins in the in-plane magnetic unit cell and associated octahedra are illustrated while the top and bottom $(\text{Ru/Mn})\text{O}_6$ layer have identical spin ordering structure [1].

4.3 $\text{Sr}_3(\text{Ru}_{1-x}\text{Mn}_x)_2\text{O}_7$ ($x = 0.125$)

Having characterized the magnetic structure in the ground state of SRMO 16, the next logical step would be to perform a similar analysis for lower concentrations of Mn-substitutions, with the primary objective of gaining further insight of the underlying physics behind the doping dependence of the magnetic structure in the antiferromagnetic ground state. Of particular interest are issues such as 1) how does Mn-doping induces both an AFM and an insulating ground state? And 2) how does the magnetic phase transition correlates with the electronic phase transition for different doping levels in these systems?

4.3.1 Experimental Details

Single crystals of SRMO12.5 were grown by the floating zone method and subsequently characterized by powder, single-crystal X-ray diffraction, and physical property measurements in Dr. Rongying laboratory at Louisiana State University by Dr. Biao Hu [45]. The single crystal used have a mosaic spread of $\sim 1^\circ$ and a mass of 0.378 grams. As with the SRMO 16 sample, the crystal structure (see Figure 4.1) is described using an orthorhombic cell consistent with the space group $Pban$ with room temperature lattice parameters $a = b = 5.50(1)$ Å and $c = 20.72(1)$ Å [40]. We index all diffraction peaks following the orthorhombic unit cell notation. The wave vector $\mathbf{Q} = (Q_x, Q_y, Q_z)$ is in units of Å^{-1} and $(H, K, L) = (Q_x a / 2\pi, Q_y a / 2\pi, Q_z a / 2\pi)$ is in reciprocal-lattice units (r.l.u).

We performed measurements on both the WAND located at HB-2C and the TAS HB-1A at the HFIR at ORNL. We focused on obtaining measurements of the magnetic peaks associated with the AFM ordering in the ground state. Specifically, we obtained the diffraction patterns in the $(H, K, 0)$ and $(H, 0, L)$ reciprocal scattering planes as a function of temperature and carried out a magnetic structure refinement following the same steps as we did with 16% Mn-substituted sample. As before, the single crystal samples were enclosed in a cylindrical vanadium can and subsequently mounted inside a standard orange HFIR-cryostat and a cryofurnace was used for regulating the temperature. The triple-axis spectrometer configuration consisted of a PG (002) analyzer for both the monochromator and analyzer with a fixed incident neutron wavelength of 2.359 Å ($E_i = 14.62$ meV) and collimations of $48'48' - \text{sample} - 40'68'$. Measurements on the US/Japan Wide Angle Neutron Diffractometer (WAND) installed at the beam port HB-2C at HFIR were taken with collimations of $48'40' - \text{sample} - 40'120'$. A Ge (111) single crystal for the monochromator was used to produce an incident neutron with a wavelength of 1.48 Å.

And diffraction patterns for magnetic refinement analysis were taken in steps of 0.2° covering a range of 125° .

4.3.2 Magnetic Structure

The wave vector associated with the magnetic order [$\mathbf{Q}_M = (0.5, 0, 0)$] in the 12.5 % Mn-substituted SRO 327 system is, as expected, consistent with previous studies and with the other concentration of Mn-substituted SRO 327 studied. The AFM transition temperature was obtained from the T -dependence of the order parameter and was found to have a value of $T_N \sim 66$ K, which was consistent with magnetic susceptibility measurements [45].

In order to be able to make a direct comparison to SRMO 16 studies, similarly to Figure 4.4, Figure 4.8 displays the obtained neutron diffraction patterns SRMO 12.5 in the $(H, K, 0)$ and $(H, 0, L)$ reciprocal planes for temperatures above and below T_N . The analysis of the spin configuration revealed the same results as those found for the 16 % sample. The nuclear Bragg peaks can be seen in Figure 4.8(a) at $T > T_N$. The majority of the peaks observed can be indexed using the $I4/mmm$ space group diffraction conditions while those not belonging to this symmetry indicate the lowering of the symmetry to Pbn space group which originates from the rotations of the RuO_6 octahedra about the c -axis. Both nuclear and magnetic scattering diffraction are shown on Figure 4.8(b) taken at $T = 4$ K. Extensive data collection along high symmetry directions, again indicates that the spin structure for the 12.5 % Mn-substituted SRO 327 sample is that of E -type AFM ordering. The expanded difference scattering patterns in the $(H, 0, L)$ scattering plane (intensity image in linear scale) between the low- T AFM phase and temperatures of $T > T_N$ are presented in Figures 4.8(c) and (d). In order to be able to show more clearly the studied magnetic Bragg peaks, the differential diffraction patterns have been zoomed in. Of particular interest in Figure 4.8(c) and (d) are the broadened $(0.5, 0, 0)$, $(1.5, 0, 0)$, and $(2.5, 0, 0)$

magnetic peaks along L . The neutron diffraction profiles behave exactly in the same way as those shown in Figure 4.5(b) for the $(1.5, 0, 0)$ peak in the $(H, 0, L)$ scattering plane for SRMO 16%; the L scans across any of these peaks exhibit very broad Lorentzian profiles, which is indicative of short-range AFM correlations along the c -axis.

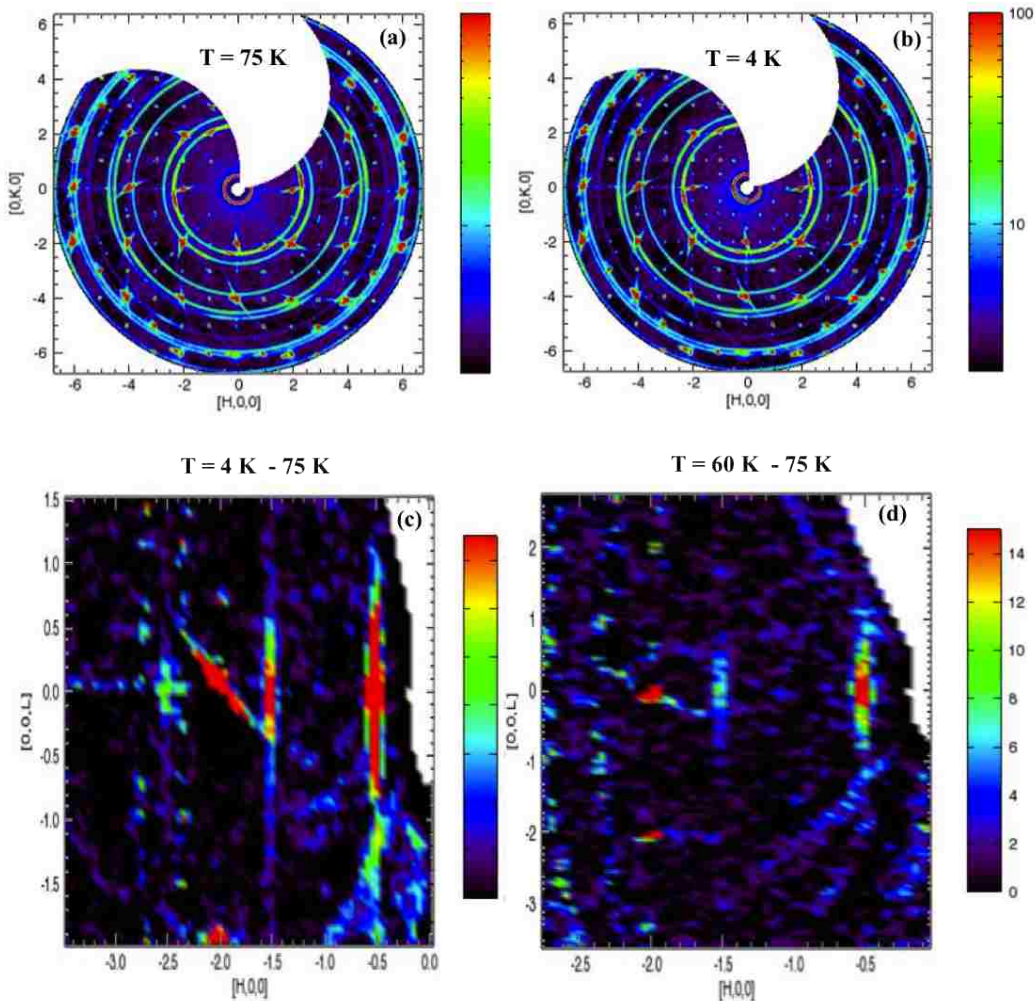


FIGURE 4.8 Neutron diffraction patterns of SRMO 12.5 in the $(H, K, 0)$ and $(H, 0, L)$ reciprocal planes for temperatures above and below T_N . The color bars represent the intensities in counts per 5 mins and the powder rings observed are those of the Aluminum. The raw data reported on the top panel (on a logarithmic scale) show (a) the structural peaks at $T > T_N$ and (b) the combination of both structural and magnetic peaks at $T < T_N$. Peaks are indexed using the orthorhombic notation. The differential diffraction patterns at $T = 4 \text{ K}$ from $T = 100 \text{ K}$ and that of $T = 60 \text{ K}$ from $T = 100 \text{ K}$ are shown in (c) and (d), where the studied magnetic Bragg peaks observed at the base T are zoomed in for clarity.

The dimensionality of the spin order in SRMO 12.5 % was characterized from the in plane $(H, K, 0)$ and out-of-plane $(H, 0, L)$ magnetic correlations from T -dependent line profiles (not shown here) of superlattice peaks. The neutron diffraction profiles were extracted from the temperature dependence of the integrated magnetic scattering intensity shown in Figure 4.9 (i.e. from the AFM order parameter) for the $(0.5, 0, 0)$ AFM Bragg peaks in the (a) $(H, K, 0)$ plane along H and (b) $(H, 0, L)$ plane along L . Consequently, magnetic correlation lengths $\zeta(T)$ were obtained in both scattering planes in order to reveal the dimensionality of the ordered spin structure in this lower doping concentration. Similar to the case of SRMO 16, as was evident from the zoomed in differential diffraction patterns given in 4.8 (c) and (d), L scans across the $(0.5, 0, 0)$ magnetic peak are characterized by broad Lorentzian-profiles, indicating short-range AFM correlations along the c -axis. The extracted c -axis magnetic correlation length $\zeta(T)$ shown in the insert of Figure 4.9(b) shows only a maximum value of $\zeta \sim 6 \text{ \AA}$ below T_N . On the other hand, in sharp contrast to the 16 % Mn-substituted system, the linewidth of the H scans across the $(0.5, 0, 0)$ magnetic Bragg peaks are *not* resolution limited, they are much broader than the instrumental resolution. After a convolution of the instrumental resolution with the Lorentzian profiles, a finite correlation length of $\zeta(T) \sim 30 \text{ \AA}$ is obtained for the ab -plane. An obvious conclusion from these results is that Mn-concentration in SRO 327 is directly proportional to the dimensionality of the spins along the ab -plane and has no impact on the already short-range correlations (exclusively restricted to the bilayered-block of the RuO_6 octahedra) existing along the c -direction.

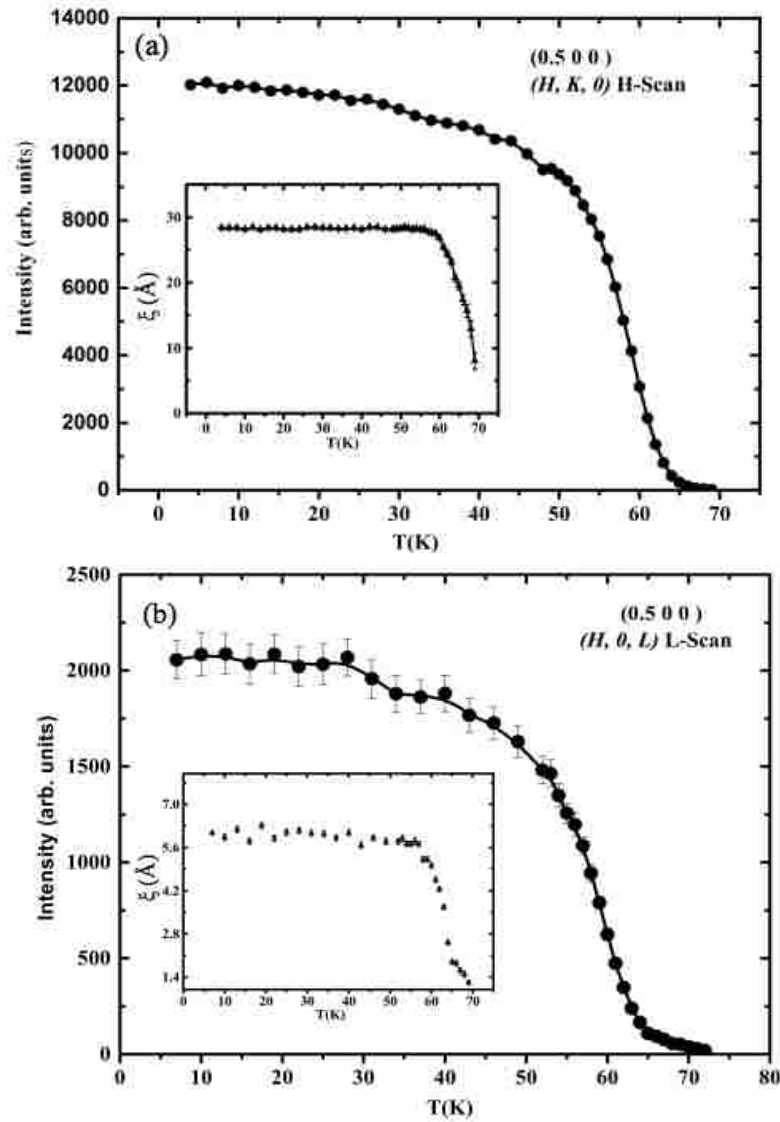


FIGURE 4.9 Temperature dependence of the integrated magnetic scattering intensity for the (0.5, 0, 0) AFM Bragg peaks. (a) $(H, K, 0)$ plane along H and (b) $(H, 0, L)$ plane along L . Insets show the extracted correlations lengths $\zeta(T)$ (from a convolution of the instrumental resolution with Lorentzian fits) from the line profiles obtained from the order parameter measurements.

As a result, the spin structure resulting from our *FullProf* magnetic refinement depicted in Figure 4.7 remains the same for this concentration. That is, moments aligned along the c -direction with spins coupled FM within the bilayer and AFM along the basal plane still provide the best fit for the data.

4.4 Summary

It is known that there is close correlation between the magnetic ground state and the structural distortion in the layered ruthenates attributed to a strong spin-lattice coupling. The rotational distortion of the RuO_6 octahedra tends to enhance the FM instability while the combination of tilting and flattening of the RuO_6 octahedra favors AFM fluctuations as manifested in the $\text{Ca}_{2-x}\text{Sr}_x\text{RuO}_4$ [76]. For chemical substituted $\text{Sr}_3\text{Ru}_2\text{O}_7$, the exact magnetic ground state depends on the nature of the substituent. It is intriguing to note that a small amount of Ti or Mn substitution can stabilize AFM ordering, either incommensurate (IC) in the case of Ti substitution or commensurate (CM) in the Mn substitution case, different from the dynamic AFM fluctuations observed in the parent compound. In case of nonmagnetic Ti substitution, a flattening of the unit cell is realized with the shrinking c-axis lattice constant and expanding those in the basal plane [74]. While it is not clear if additional rotational distortion of RuO_6 exists as in the Mn-doped sample, Ti substitution enhances the IC dynamics and ultimately leads to a static spin-density-wave (SDW) -type magnetic order at $x_{\text{cr}} \sim 0.04$ and above [74]. This occurs when the spin excitations are dominated by the fluctuations associated with dynamical nesting properties of the quasi 1D part of the Fermi surface that is controlled by the $4d_{xz}$ and $4d_{yz}$ orbitals.

The situation is different in Mn-substituted $\text{Sr}_3\text{Ru}_2\text{O}_7$ as the substituent is magnetic with a smaller ionic radius. The introduction of Mn flattens the RuO_6 octahedra by reducing out-of-the-plane Mn/Ru-O bond length without introducing a tilt distortion [45], similar to the case of Ti substitution [74]. This results in an increase of the d_{xz}/d_{yz} bandwidth. However in contrast to the case of Ti substitution, Mn substitution suppresses the rotational distortion present in parent compound, thus it has little effect on the in-plane Mn/Ru-O bond length. This implies that the $4d_{xy}$ orbital, associated with the quasi-2D sheet of the Fermi surface, does not play an important

role in the magnetism of this system. Thus, the structural modifications introduced by the substitution of Mn in this SRO 327 system are not consistent with an insulating ground state expected from first-principle calculations [76] or one resulting from a simple Mott-type scenario [3]. Our results lead us to conclude that the observed AFM insulating state in Mn-doped Sr₃Ru₂O₇ is then puzzling as is inconsistent with the *conventional wisdom* [76], and its origin is likely related to additional cooperative effects from doped magnetic ions.

To conclude, our elastic neutron scattering investigation has revealed the structure, orientation, and dimensionality of the magnetic structure in the bilayered ruthenate Sr₃(Ru_{1-x}Mn_x)₂O₇ for Mn concentrations of 12.5 and 16%. For the case of SRMO 16 single crystals, the ground state is characterized by a long-range *E-type* AFM spin arrangement described by a commensurate (0.5, 0, 0) propagation wave vector along the basal plane, with moments aligned along the *c*-direction. Within the same AFM-I regime, the SRMO 12.5 system is consistent with the findings reported above. However, the *E-type* AFM spin arrangement along the basal plane is characterized by a finite correlation length. The latter is an indication that although Mn concentrations as small as 5% induce AFM order in the system [46], increasing the amount of Mn has the effect of stabilizing the long-range *E-type* AFM spin texture along the basal plane in these systems.

To the best of our knowledge at the time of writing this thesis, this work reports the first detailed study of the magnetic order induced by Mn substitution in Sr₂Ru₃O₇ using neutron diffraction of single crystals. The accurate description of the magnetic structure is an important step towards a more global understanding of the evolution of the electronic properties as well as the nature of the metal-insulator transition that characterizes these systems.

Chapter 5

A Study on the Doping Dependence of Phase Segregation in the Colossal Magnetoresistive Manganite $\text{Pr}_{1-x}\text{Ca}_x\text{MnO}_3$ ($x = 0.30, 0.35,$ and 0.40)

5.1 Introduction

Manganites of the form $R_{1-x}A_x\text{MnO}_3$ (where R and A are rare- and alkaline-earth ions) provide an archetype laboratory for the study of phase inhomogeneities. In general, doping (x) not only causes a quenched disorder due to the ionic size mismatch of A-site cations (R vs. A) in the perovskite lattice but also induces a distinct chemical valence in Mn ions (Mn^{3+} vs. Mn^{4+} in the original portrayal [77, 78], introducing charge as a new degree of freedom. The vast array of stable ground states, as observed from the (T,x) phase diagrams, is responsible for the strong tendency towards phase separation and competition that is well-known to dominate the physics of manganites. For example, the spin-canted state, originally proposed by de Gennes [79] using the simple one-orbital model in the mean-field approximation, is now thought to be a mixture of ferromagnetic (FM) and antiferromagnetic (AF) states (see [16] and references therein). On the other hand, the famous charge/spin/orbital (CO-OO) order denoted as the CE -type checkerboard-like CO-OO state at low temperature (LT) [77] shown in Figure 5.1 which is found at concentrations near $x \sim 0.5$ in these systems, is known to promote an AF insulating phase that competes with the FM metallic state [22, 61, 80, 81].

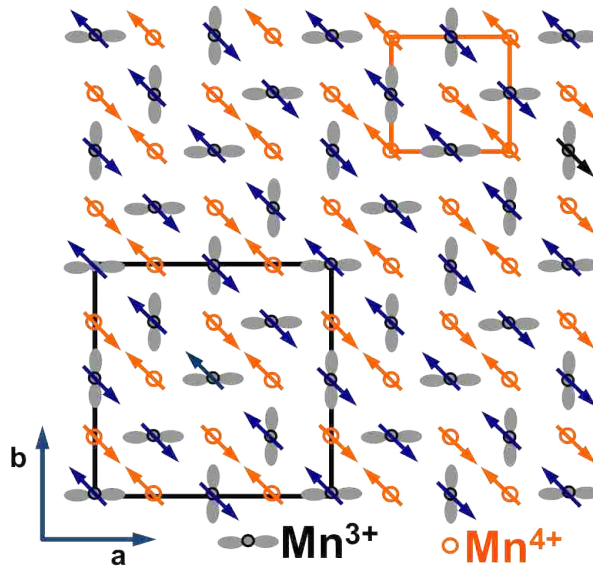


FIGURE 5.1 Schematic representation of the ab -plane of the CE-type structure with both orbital ($d_{3x^2-r^2}/d_{3y^2-r^2}$) and spin orderings. The bigger square denotes the Mn^{3+} orbital/magnetic unit cell while the smaller square shows the Mn^{4+} magnetic unit cell. Figure adapted from [2].

5.2 Properties of $\text{Pr}_{1-x}\text{Ca}_x\text{MnO}_3$ ($x = 0.30, 0.35, \text{ and } 0.40$)

The $\text{Pr}_{1-x}\text{Ca}_x\text{MnO}_3$ system is one that presents a particularly stable charge/spin/orbital order over a broad regime of whole-doping concentration, thus making it an ideal system for studies of the CO-OO state. For concentrations from $x = 0.30$ to 0.75 an AF CO-OO is stabilized as the ground state with an arrangement similar to that of the CE-type [82]. Numerous studies have been devoted to the study of the charge distribution of the ground state away from $x = 0.5$ due to the fact that the presented CE-type state is not “perfect” due to the changing doping concentration. As mentioned before, in a conventional CO-OO state, A *site-centered* CO-OO structure (see Figure 5.2 (a)), has been suggested in half-doped manganites ($x = 0.5$) with 1:1 ratio of Mn^{3+} and Mn^{4+} ions. However, another possible CO-OO pattern may also prevail, namely the so-called *bond-centered* structure (refer to Figure 5.2 (b)) in which the charge is localized not on Mn sites

but on Mn-O-Mn bonds with no distinctive $\text{Mn}^{3+}/\text{Mn}^{4+}$ sites [48, 83 – 86] thus raising an unsettled issue on the nature of the ground state around $x = 0.5$ [87].

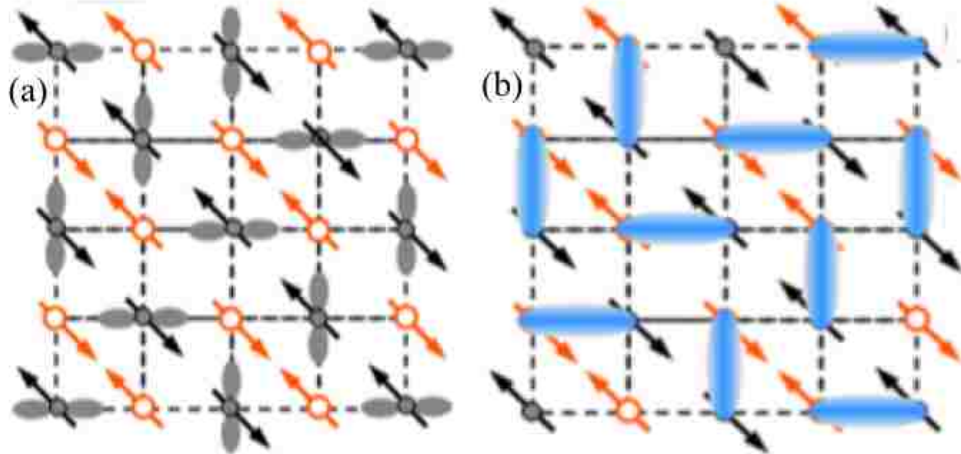


FIGURE 5.2 Schematic diagrams of the charge distribution scenarios in perovskite manganites with ground state near $x = 0.5$. Panel (a) displays the site-centered CO-OO structure where the charge is localized within the distinct Mn^{3+} and Mn^{4+} ions of the CE-type motif (as proposed in the 1950's [48] and [78]). (b) Bond center CO-OO structure of “Zener Polarons” in which the charge is distributed on the Mn-O-Mn bonds with no distinctive Mn sites [83].

Furthermore, even in some *non*-half-doped ($x \neq 0.5$) manganites, an ostensible *pseudo*-CE-type CO-OO state has also been reported [61, 88 – 92]. Within the CE-type CO-OO frame, excess of electronic charge (or Mn^{3+} ions) with respect to the ideal half-doped ($x = 0.5$) case exists in these *non*-half-doped compounds. Consequently, important issues are naturally raised: how is the excess of electronic charge distributed in the CO-OO state and what are the arrangement of spins and orbitals? There are at least three possible scenarios based on the charge distribution. One is that the excess of electronic charge is distributed *locally* (or even phase-separately) in the CE-type motif with distinct Mn^{3+} and Mn^{4+} sites. Apparently an electronic/magnetic phase separation is unavoidable due to unequal amount of Mn^{3+} and Mn^{4+} ions while keeping the rigid CE-type Mn^{3+} and Mn^{4+} order. Another possibility is that the excess

of charge is distributed *uniformly* in the CE-type motif in which there are still two Mn sublattices but each with partial e_g occupancy [i.e. charge disproportionation ($0 < \delta < 0.5e^-$)] [93 – 95]. Both scenarios can be categorized as *site-centered* structure because of having distinctive Mn sites, one inhomogeneous while the other homogeneous. The third scenario is the completely homogenous *bond-centered* structure with a Zener Polaron (ZP)-type ordered state in which all Mn sites are equivalent ($\delta = 0$) [83, 96]. So far it is unclear which charge arrangement is more appropriate for the observed CO-OO state. One avenue we set out to explore with this work is whether or not it could be possible that hole-doping concentration governs the evolution of the charge/spin/orbital order in these perovskite manganite systems. Thus, by probing the evolution of spin structure (which is presumably correlated to the electronic structure) we intend to gain insight into the phase evolution as a function of doping concentration.

5.3 Experimental Details

In this work, we report the signature of magnetic phase separation in the CO-OO state from neutron scattering studies of a prototype manganite system⁴ [2]: $\text{Pr}_{1-x}\text{Ca}_x\text{MnO}_3$. This colossal manganite system is a non-metallic perovskite with a CO-OO ground state over a broad doping range ($0.3 \leq x \leq 0.7$) [82]. Because Pr^{3+} and Ca^{2+} have almost equal ion radii (1.120 Å for Ca^{2+} vs. 1.126 Å for Pr^{3+}), $\text{Pr}_{1-x}\text{Ca}_x\text{MnO}_3$ has negligible quenched disorder, thus making it an ideal system to elucidate how doping affects the structure and evolution of CO-OO and magnetic ground states. Our results reveal a critical doping concentration (x_{cr}) that divides the inhomogeneous from the homogeneous charge/spin/and orbital ordered state, thus providing direct evidence of the effect that doping has on the evolution of the CO-OO state.

⁴ Sha Hao carried out the majority of the experiments. Dalgis Mesa performed the elastic experiments on PCMO 35 samples at NIST and at the HFIR.

Three single crystals with doping $x = 0.3$ (PCMO30), 0.35 (PCMO35) and 0.4 (PCMO40) were grown by the floating-zone method [61]. The crystals were characterized and found to have mosaic spreads of about 1° and volumes of $\sim 0.4 \text{ cm}^3$. The neutron scattering measurements were carried out using the HB-1 and HB-3 Triple-Axis spectrometers (TAS) at the High Flux Isotope Reactor (HFIR) at Oak Ridge National Laboratory (ORNL), as well as the BT-7 and BT-9 Triple-Axis beam lines at the National Institute of Standard and Technology (NIST). We have used pyrolytic graphite (PG) single crystals for both the monochromator and analyzer. Neutrons with a wavelength of 2.46 \AA ($E_f = 13.6 \text{ meV}$) were selected for measurements. For simplicity, we label all wave vectors in terms of the pseudo-cubic unit cells with lattice parameters of $a = 3.87 \text{ \AA}$, although all of our samples have orthorhombic structures slightly distorted from the cubic lattice. The wave vector $\mathbf{Q} = (Q_x, Q_y, Q_z)$ is in the unit of \AA^{-1} and $(H, K, L) = (Q_x a / 2\pi, Q_y a / 2\pi, Q_z a / 2\pi)$ is in reciprocal lattice units (r.l.u). The samples were aligned to allow the wave vector in the form of $(H, K, 0)$ accessible in the horizontal scattering plane.

All of the measurements were based upon the *CE*-type structure with CO-OO and AF ordering shown in Figure 5.4. Including the orbital part, the periodicity of AF order for Mn^{3+} spins is twice that of Mn^{4+} spins. Therefore, with respect to a reciprocal lattice vector $\boldsymbol{\tau}$, and in relation to the wave vector as $\mathbf{Q} = \mathbf{q} + \boldsymbol{\tau}$, the propagation wave vector \mathbf{q} is $(0.5, 0, 0)$ for the AF network of Mn^{4+} spins and $(0.25, 0.25, 0)$ for the AF network of the Mn^{3+} spins (which is also the same \mathbf{q} for the CO-OO structure). Based on the different \mathbf{Q} -dependence between structural- and magnetic form factor, one can choose “large” wave vectors \mathbf{Q} to probe CO structure and “small” \mathbf{Q} ’s to probe the magnetic ordering even though both have the same reduced propagation wave vector \mathbf{q} . As shown in Figure 5.3 (a) [10], we used $\mathbf{Q} = (2.25, 0.25, 0)$, $(1, 0, 0)$, $(0.75, 0.25, 0)$, and $(0.5, 0, 0)$, to probe the order of the CO-OO, FM, AF states at Mn^{3+} and Mn^{4+} sites,

respectively. The corresponding short-range correlations/clusters were also determined by measuring the diffuse scattering around these characteristic positions. After considering the instrument resolution function, we did not observe obvious q -orientation anisotropy in the scattering intensity profile. The results shown in this paper were taken along the longitudinal scan direction for the FM and along transverse one for the CO-OO, Mn^{3+} AF, and Mn^{4+} AF scattering [see Figure 5.3 (a)].

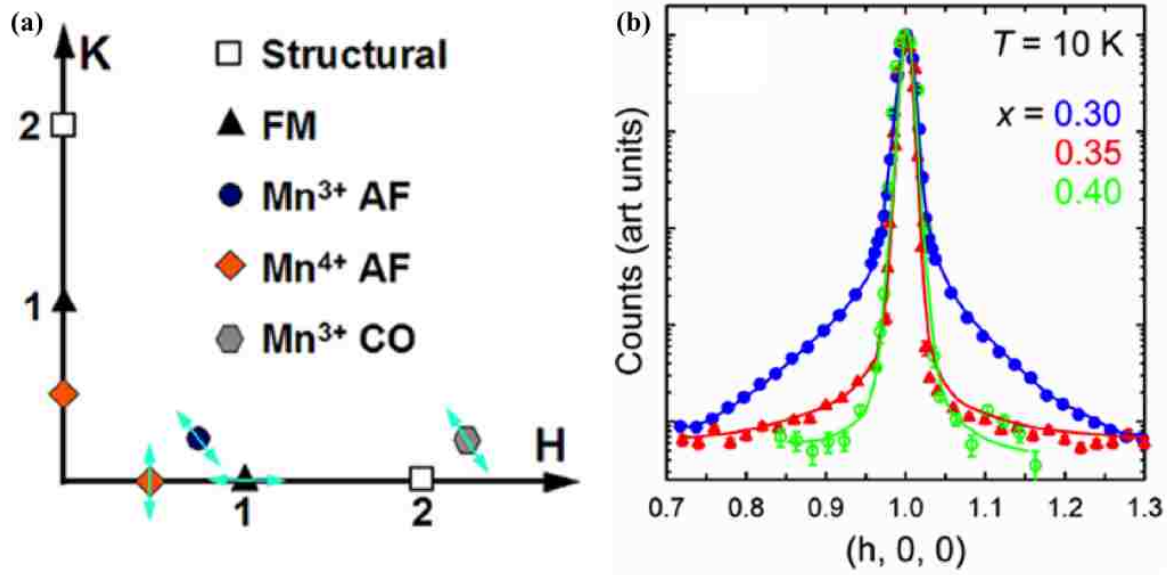


FIGURE 5.3 Schematic representations of probed peak positions in reciprocal space and representative q -scan profiles for various doping concentrations. (a) Probed superlattice peak positions and the scan directions (marked by arrows) in reciprocal space. (b) Normalized q -scan profiles of scattering peaks near $(1, 0, 0)$ at $T = 10\text{K}$ for PCMO30 (blue), PCMO35 (red), and PCMO40 (green). The solid lines serve as guides to the eye. Figure adapted from [2].

5.4 Doping Dependence of Phase Segregation

The scattering results confirm that the ground state of the three doping levels of crystals studied is a CO-OO state with primarily AF spin structure. As listed in Table 5.1, the measured transition temperatures for CO-OO, AF, and FM phase are in agreement with those reported in the literature. A canted long-range FM order coexists with AF structure in PCMO30 below $T_C = 110$ K (see the inset of Figure 5.5), known as a canted AF insulating (CAFI) phase [97 – 99]. However, no long-range FM order was detected in the ground state for either PCMO35 or PCMO40.

TABLE 5.1 The integrated intensity ratios of the magnetic diffuse and total (diffuse plus Bragg) scattering vs. doping in the ground state at 10 K. ρ_{FM} is the ratio obtained from the scan across (1, 0, 0) by subtracting the lattice contribution of the Bragg peak; ρ_{AF} , the ratio obtained from the scan across (0.5, 0, 0).

$\text{Pr}_{1-x}\text{Ca}_x\text{MnO}_3$	$x = 0.30$	$x = 0.35$	$x = 0.40$
$T_{\text{CO}}; T_{\text{N}}; T_{\text{C}}$ (K)	210; 125; 110	230; 160; N/A	245; 170; N/A
$\rho_{FM} = \frac{I_{\text{diffuse}}(FM)}{I_{\text{total}}(FM)} (\times 100 \%)$	15.1 ± 2.0	N/A	N/A
$\rho_{AF} = \frac{I_{\text{diffuse}}(AF)}{I_{\text{total}}(AF)} (\text{Mn}^{4+}) (\times 100 \%)$	28.7 ± 0.8	0.160 ± 0.003	0

To determine the FM, AF, and CO-OO short-range correlations in the ground state of $\text{Pr}_{1-x}\text{Ca}_x\text{MnO}_3$, we have measured the scattering profiles at (1, 0, 0), (0.75, 0.25, 0), (0.5, 0, 0), and (2.25, 0.25, 0), respectively with a wide \mathbf{q} -scan range. We observed a strong doping dependence of both AF and FM diffuse scattering. Figure 5.3 (b) displays the normalized \mathbf{q} -scans at (1, 0, 0) including both magnetic and structural scattering from the three doping levels. Similar to that

reported before [97 – 100] a strong diffuse component appears near the Bragg peak for PCMO30, which indicates that FM local spin clusters coexist with the long-range FM order in the ground state. In contrast, PCMO35 has a rather weak FM diffuse shoulder. PCMO40 shows only a nice Gaussian profile due to long-range lattice scattering with no sign of short-range spin correlation. The AF scatterings profiles at $(0.5, 0, 0)$ and $(0.75, 0.25, 0)$ demonstrate similar doping dependence of diffuse components (see Figure 5.4 (a)-(f)).

As summarized in Table 5.1, PCMO30 has a CAFI ground state with a significant amount of FM/AF clusters $\rho_{FM} \approx 15.1 \pm 2.0 \%$ and $\rho_{AF} \approx 28.7 \pm 0.8 \%$. While PCMO35 has an almost homogeneous AF ground state with a very small amount of spin clusters, PCMO40 has a completely uniform AF ground state. Therefore, a critical doping concentration (x_{cr}) must exist and be very close to the value of $x = 0.35$ thus serving as the boundary between the inhomogeneous and homogenous ground state of $\text{Pr}_{1-x}\text{Ca}_x\text{MnO}_3$.

To further reveal such a critical doping behavior for the inhomogeneity present in the magnetic structure, we have examined the T -dependence of the FM diffuse scattering intensity at $\mathbf{Q} = (0.96, 0, 0)$, which is outside the influence of the Bragg diffraction for long-range ordering. Figure 5.5 presents the measured intensity as a function of T/T_{CO} for all three doping levels. Similar behavior is obtained for different scattering wave vectors (see the inset (b) of Figure 5.5). The FM diffuse component clearly displays different T -dependence above and below T_{CO} (comparable results have also been reported by Kajimoto *et al.* [100]). When $T \geq T_{CO}$ all three doping levels of crystals exhibit similar T -dependence of the diffuse component, reflecting the FM spin fluctuations in paramagnetic (PM) phase, which are presumably induced by the DE interaction [17, 53].

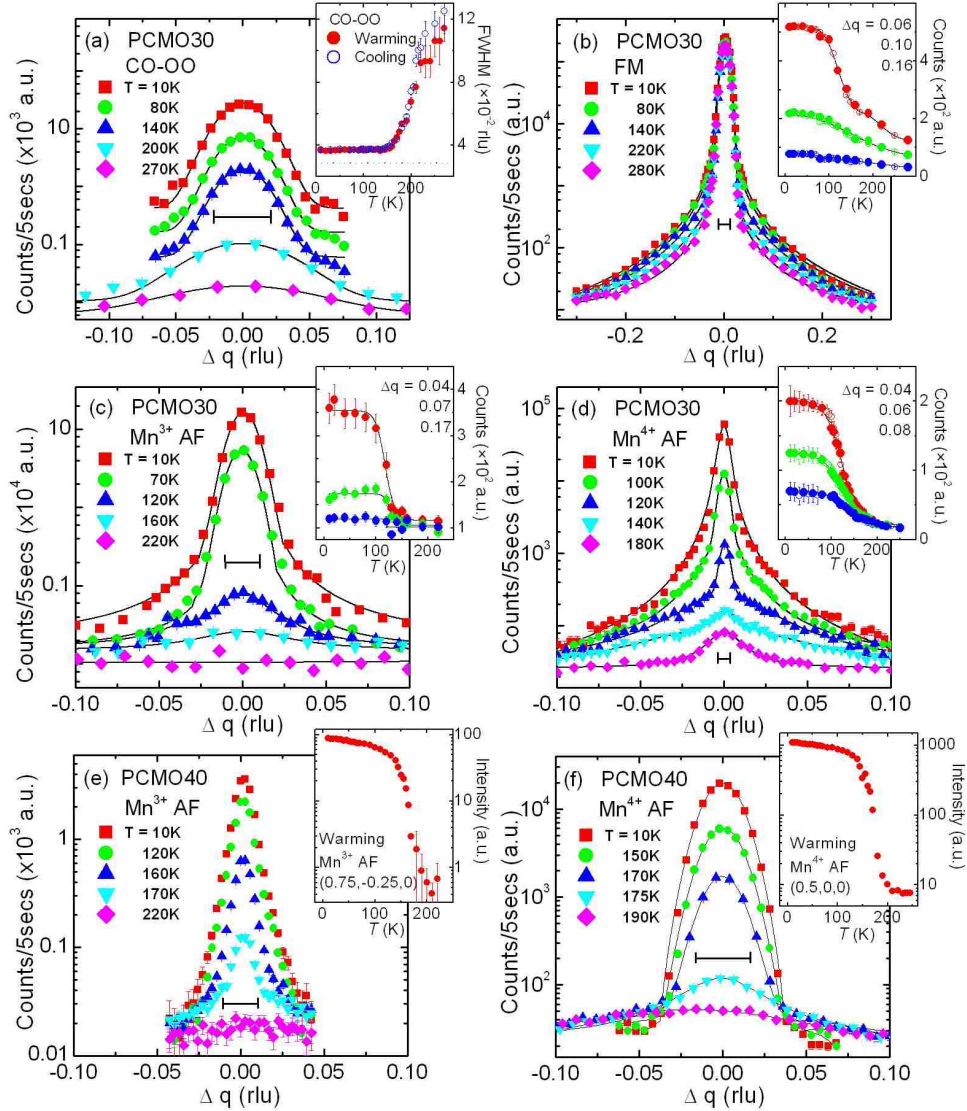


FIGURE 5.4 Representative q -scan profiles of the long- and short-range charge-ordered (CO), ferromagnetic (FM), and antiferromagnetic (AF) correlations in single crystals of PCMO30 and PCMO40. (a) PCMO30 CO peak near $(2.25, 0.25, 0)$, (b) PCMO30 FM peak near $(1, 0, 0)$, and PCMO30 AF components (c) at Mn^{3+} sites near $(0.75, 0.25, 0)$ and (d) at Mn^{4+} sites near $(0.5, 0, 0)$, PCMO40 AF components (e) at Mn^{3+} sites near $(0.75, -0.25, 0)$ and (f) at Mn^{4+} sites near $(0.5, 0, 0)$ at different temperatures when the sample was on warming. The T -dependence of CO peak width as well as FM, Mn^{3+} and Mn^{4+} -site AF diffuse scattering at the respective offset positions is presented in the insets of (a) as well as those of (b), (c) and (d), respectively. The solid symbols are for warming while open symbols for cooling. The solid lines are guides to the eyes and the data in (a), (c) are incrementally shifted for clarity. The dotted lines indicate the instrument resolution. The inserts of (e) and (f) show the integrated peak intensities associated with the PCMO40 Mn^{3+} and Mn^{4+} AF ordering respectively.

On the other hand, a completely different T -dependence of diffuse components for different doping levels appears below T_{CO} . For PCMO40, the FM spin fluctuations deteriorate below T_{CO} and vanish below T_N . In principle, such a T -dependence in PCMO40 can be understood as following: When $T < T_{CO}$, the FM fluctuations, which are mediated by DE interaction, will be suppressed by the charge localization due to the establishment of CO-OO phase. When $T < T_N$, the FM fluctuations are further diminished because of the onset of AF order. For PCMO35, the FM spin fluctuations exhibit the same T -dependence as those in PCMO40, thus indicating that they originate from the same mechanism. However, local spin clusters appear below ~ 65 K with both FM (see Figure 5.5) and AF characters as detected by the diffuse scattering at $(1, 0, 0)$, $(0.5, 0, 0)$, and $(0.75, 0.25, 0)$. This is distinctive from the FM fluctuations at high temperature. In sharp contrast with those in both PCMO35 and PCMO40, the population of spin clusters in PCMO30, reflected by the intensity of FM diffuse component, increases rather than decreases below T_{CO} . Surprisingly, it increases much more drastically below T_N , regardless of the establishment of long-range AF order, thus suggesting the spin clusters in the ground state may have a different nature from the DE-mediated FM fluctuations at high temperature.

The spin clusters appearing in PCMO30 for low- T regime also display both FM/AF characters, similar to those existing in the ground state of PCMO35. As shown in Figure 5.6, the integrated diffuse scattering intensity and the extracted short-range correlation length ξ near the FM peak at $(1, 0, 0)$ and AF peak at $(0.5, 0, 0)$ exhibit *very similar* T -dependence. In PCMO30, the spin clusters appear above T_N and then significantly increase their population and correlation length below T_N . From Table 5.1, we defined a spin population of local clusters in the ground state as the integrated intensity ratio of the magnetic diffuse and total magnetic scattering. The spin population in the local clusters in the ground state of PCMO30 was estimated as $\rho_{FM} \approx$

$15.1 \pm 2.0 \%$ and $\rho_{FM} \approx 28.7 \pm 0.8 \%$. The calculated average cluster diameter (*i.e.* correlation length) is $\xi_{FM} \sim 60 \text{ \AA}$ from FM and $\xi_{AF} \sim 80 \text{ \AA}$ from AF scattering.

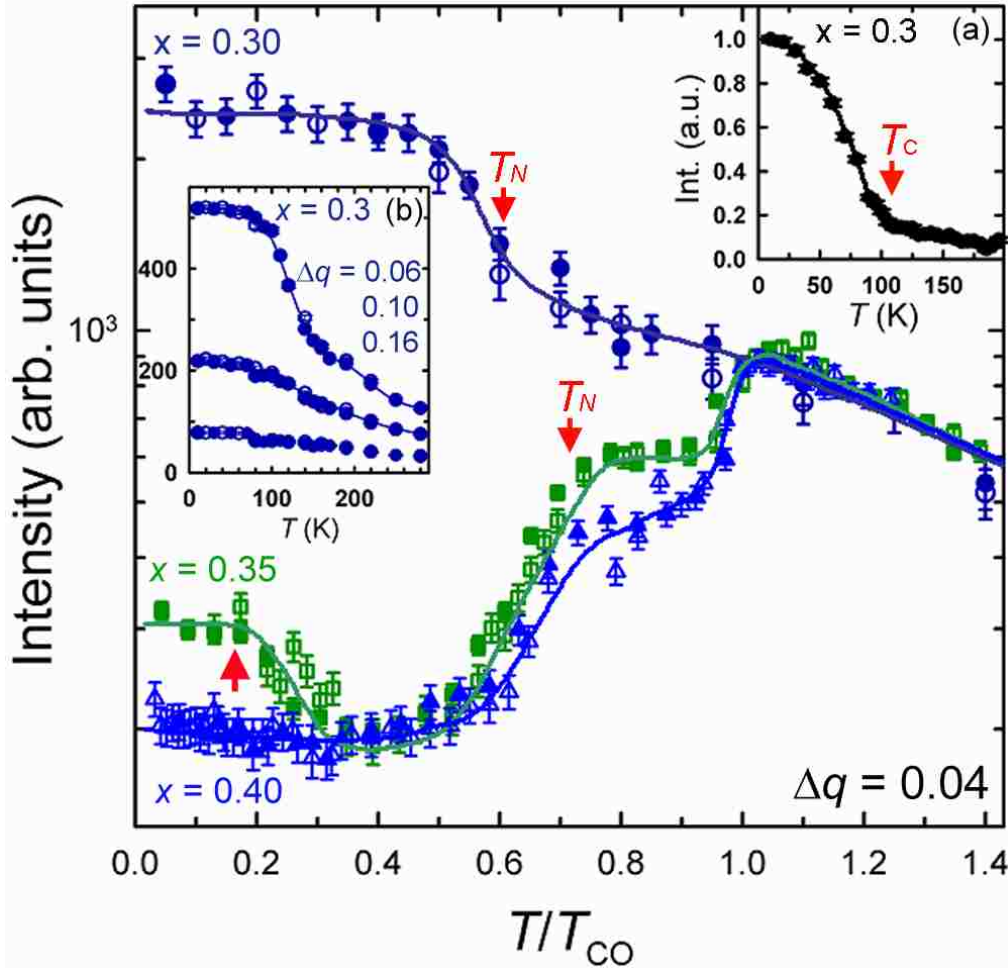


FIGURE 5.5 T -dependence of the FM diffuse component measured at $(0.96, 0, 0)$ ($\Delta q = 0.4$ r.l.u.) for different Ca-concentrations of $\text{Pr}_{1-x}\text{Ca}_x\text{MnO}_3$ on cooling (solid symbols) and warming (open symbols). The solid curves are a guide for the eye. Arrows mark the Curie and Néel temperatures, as well as the onset of spin phase separation for PCMO35. The insets present the T -dependence of (a) long-range FM order parameter obtained from the peak intensity at $(1, 0, 0)$ and (b) the FM diffuse component at selected Δq positions from $(1, 0, 0)$ for PCMO30. Taken from [2].

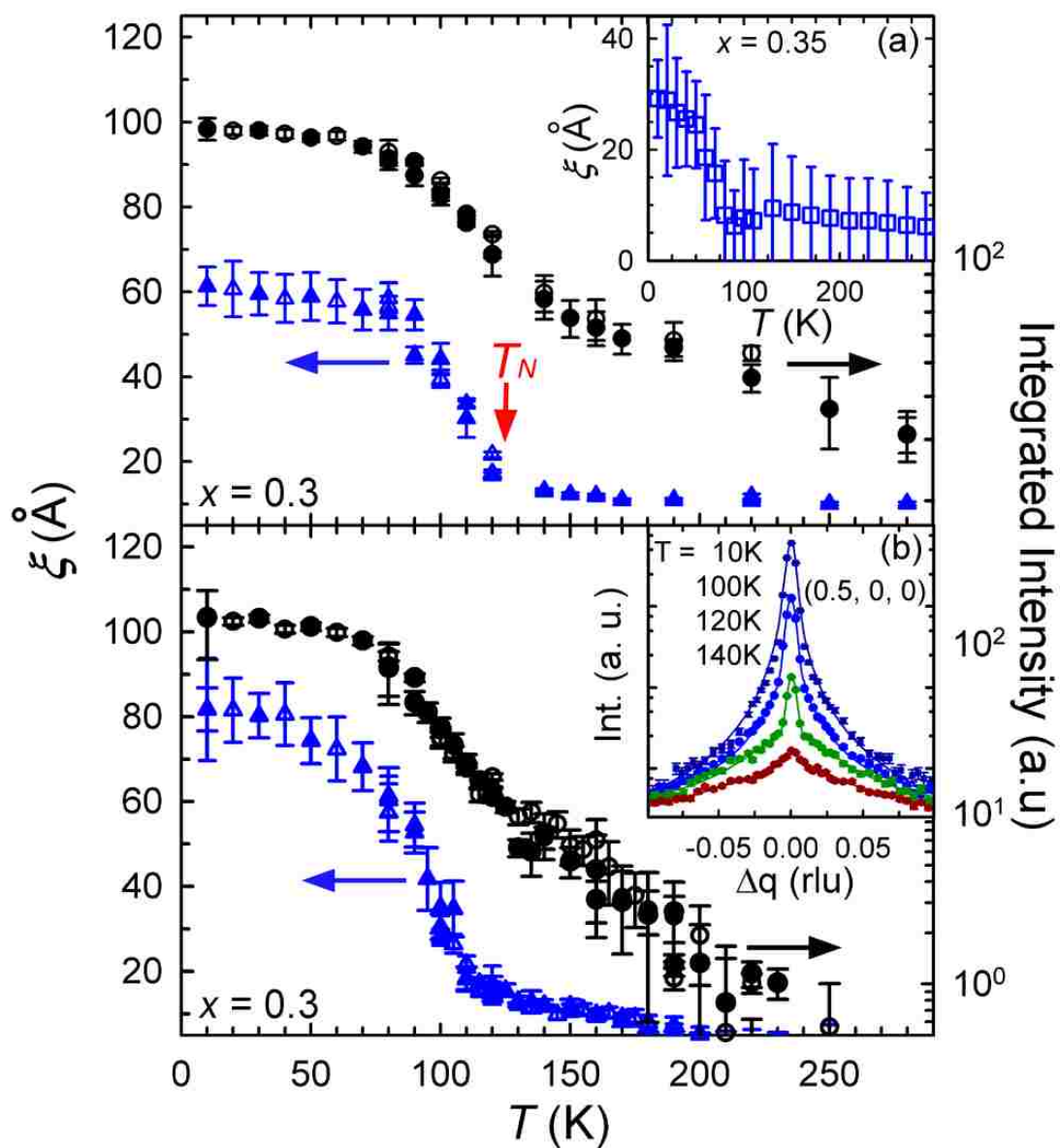


FIGURE 5.6 T -dependence of the intensity and extracted short-range correlation length of (top panel) FM at $(1, 0, 0)$ and (bottom panel) Mn^{4+} AF at $(0.5, 0, 0)$ diffuse scattering in PCMO30. The correlation length was obtained from the Lorentzian linewidth of the diffuse component through the deconvolution of the instrument resolution function determined by the second-order reflection. The solid lines are guides for the eye. The solid symbols are for cooling while open symbols for warming. The inset (a) on top panel is the T -dependence of FM short-range correlation length in PCMO35 with large error bars due to the weak diffuse scattering profiles while that of (b) on bottom panel show the normalized q -scan profiles of the Mn^{4+} AF peak at $(0.5, 0, 0)$ in PCMO30. Figure taken from [2].

Using a simple estimated population relation in the ab -plane of the crystal $\rho_{FM,AM} \propto n_{FM,AM} \xi_{FM,AM}^2$ where $n_{FM,AM}$ is the in-plane cluster density probed by FM or AF scattering, we find that $n_{FM} \cong n_{AF}$, regardless of the difference in correlation length. Therefore, we speculate that measured AF and FM diffuse scattering may be indeed caused from the same assembly of spin clusters.

Owing to the fairly weak diffuse scattering and uncertain correlation length (see inset (a) of Figure 5.6) we were not able to do the similar estimation for PCMO35. Nevertheless, the ground state in both PCMO30 and PCMO35 is a phase-separated state containing spin clusters embedded in either AF or CAF ordered matrix. The main difference between these two doping levels is that magnetic phase separation exists in all measured temperature range in PCMO30 but appears with much smaller population only at LT in PCMO35. One can anticipate that such a phase-separated ground state will disappear in a crystal of $\text{Pr}_{1-x}\text{Ca}_x\text{MnO}_3$ with a doping level slightly larger than $x = 0.35$. Such an evolution of phase separation with doping may provide some insight into the doping dependence of the observed CMR effect [61]. This evolution may also explain why smaller critical magnetic fields are required to melt the CO-OO structure for PCMO30 than that for PCMO35 and PCMO40 [5].

If indeed PCMO35 is a system that undergoes a phase evolution from homogeneous to inhomogeneous spin-ordered state by cooling, then the appearance of spin clusters at LT should affect the long-range order parameters as well. To elucidate this issue, we have investigated systematically the order parameters of CO-OO and AF at both Mn^{3+} and Mn^{4+} sites by measuring the T -dependence of the integrated Bragg peak intensity at $(2.25, 0.25, 0)$, $(0.75, 0.25, 0)$ and $(0.5, 0, 0)$, respectively. As shown in Figure 5.7, an anomaly characterized by a sudden drop in intensity of the measured order parameters in PCMO35 emerges at $\sim 35\text{K}$, coinciding with the

onset of local spin clusters, thus providing a clear signature of magnetic phase separation. In addition, we also realize that the line shape of these order parameters in PCMO30 near both T_{CO} and T_N is slightly different from that in PCMO35 and PCMO40. The transitions in PCMO35 and PCMO40 show more pronounced critical behavior than those in PCMO30. The nature behind this should be associated with the existence of phase separation near T_N and T_{CO} in PCMO30, which does not occur in the other two doping levels.

5.5 Summary

In summary, by using neutron scattering, we have observed a strong doping- x and T -dependence of magnetic phase separation in $\text{Pr}_{1-x}\text{Ca}_x\text{MnO}_3$ crystals (see panel (d) in Figure 5.7). Spin clusters with both AF and FM correlations coexist with CAFI structure in PCMO30, suggesting an inhomogeneous CO-OO state below T_{CO} . In contrast, the observed uniform AF ordered structure suggests a homogeneous AF CO state in PCMO40. We have identified a critical doping concentration x_{cr} , which should be very close to $x = 0.35$, that divides homogeneous and inhomogeneous CO-OO ground state. Whether the homogeneous CO-OO state that exists in PCMO40 can be categorized as a site-centered type with charge disproportionation ($\delta \neq 0$) or a bond-centered (Zener-polaron ordered) type is still unclear. One possible experimental method to distinguish these two types of CO-OO structures is resonant x -ray scattering [101]. Yet, it is clear that in a non-half doped manganite, a CE-type $\text{Mn}^{3+}/\text{Mn}^{4+}$ CO-OO state cannot survive without phase separation.

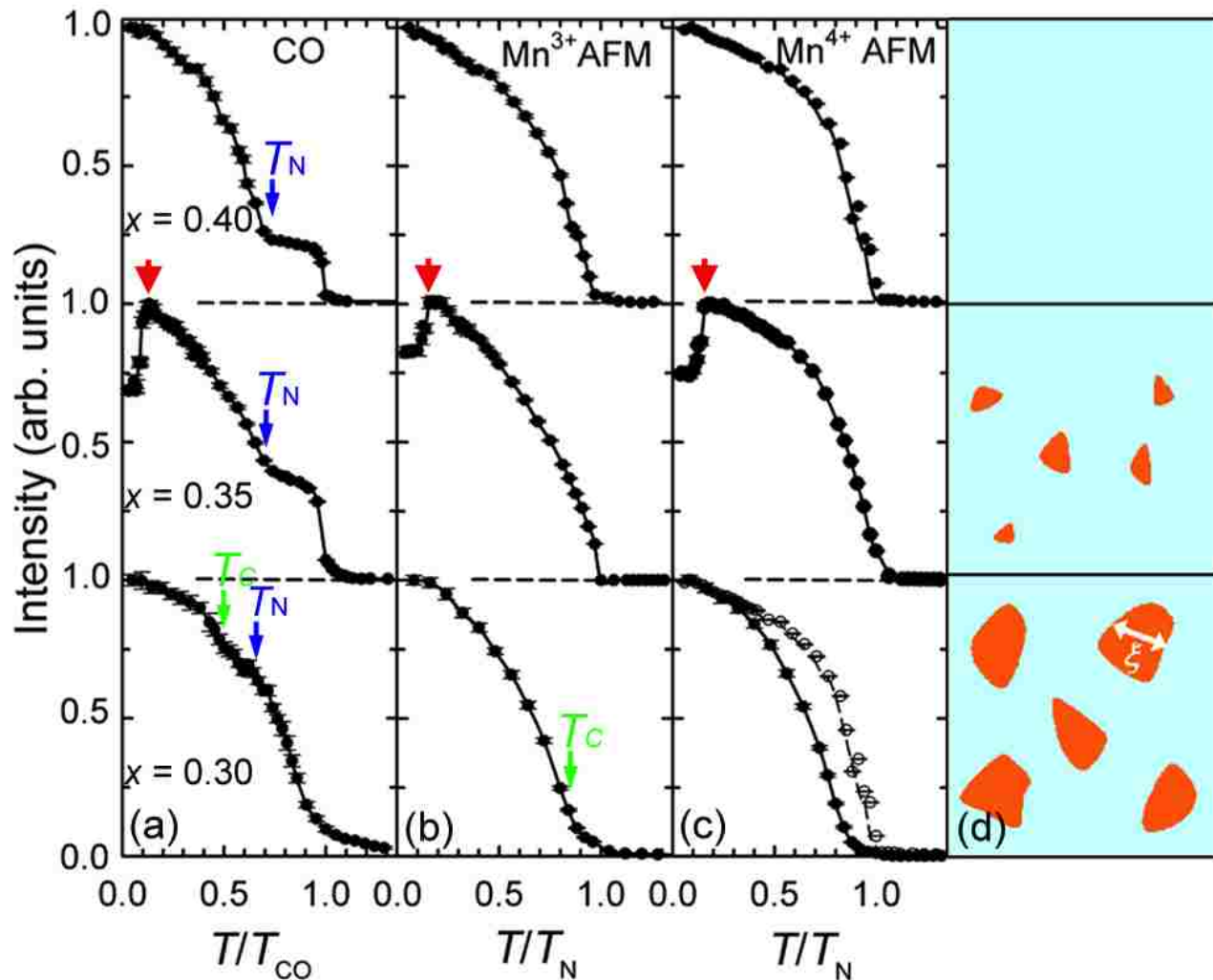


FIGURE 5.7 T -dependence of order parameters for (a) charge-/orbital-ordering (CO) measured at $(2.25, 0.25, 0)$, (b) Mn^{3+} AF ordering at $(0.75, 0.25, 0)$, and (c) Mn^{4+} AF ordering at $(0.5, 0, 0)$, for three different Ca-concentrations of $\text{Pr}_{1-x}\text{Ca}_x\text{MnO}_3$. The Mn^{4+} AF ordering parameters for both $x = 0.3$ and 0.4 (open dots) are plotted together in the bottom of panel c for comparison. Arrows mark the Curie and Néel temperatures as well as the onset of phase separation for PCMO35. Column (d) illustrates the evolution from an inhomogeneous to a homogeneous CO phase for corresponding doping levels of $\text{Pr}_{1-x}\text{Ca}_x\text{MnO}_3$. A T -induced change from homogeneous to inhomogeneous phase occurs in PCMO 35 [2].

Chapter 6

A Preliminary Study on Spin-Lattice Coupling in the Colossal Magnetoresistive Manganite $\text{La}_{1-x}\text{Ca}_x\text{MnO}_3$ ($x = 0.20$)

6.1 Properties of $\text{La}_{1-x}\text{Ca}_x\text{MnO}_3$ ($x = 0.20$)

The CMR manganite $\text{La}_{1-x}\text{Ca}_x\text{MnO}_3$ (LCMO) is a system that is commonly referred as an intermediate bandwidth (W) system. As a result, it is found to display ground states that are characteristic of large bandwidth manganites such as the presence of a robust FM metallic (M) phase over a wide range of whole doping concentrations ($0.17 < x < 0.5$) as well as the typical CO-state observed in truly small- W systems such as $\text{Pr}_{1-x}\text{Ca}_x\text{MnO}_3$ (PCMO). Among the ground states of perovskite manganites, the most studied ones are those associated with the Colossal Magnetoresistance (CMR) effect, that is, the FM-M and charge/spin, and orbital (CO) states. The least explored ground state is that of FM-I character, the ground state that 1) is the precursor of the FM-M ground state in which CMR is observed, and 2) it cannot be explained by the DE exchange interaction, which tends to induce delocalization and inhomogeneity on the FM-M phase (recall that DE interaction is known to qualitatively explain the CMR effect by promoting electric conduction and FM) [17].

As mentioned in Chapter 1, despite decades of intensive research, these manganite systems are not fully understood. Specifically, the nature of the FM-I phase has not been fully explored to the best of our knowledge. We believe that the study of this precursor phase (i.e. precursor to the CMR regime) is crucial to understanding the nature of the competing interactions (FM metallic-CO) responsible for the huge magnitude of the CMR effect in these perovskite manganites.

Studies on the low temperature (low- T) insulating behavior of perovskite manganites propose a phase separation scenario to explain the nature of the FM-I phase. For instance, tunneling experiments conducted on $\text{La}_{70}\text{Ca}_{30}\text{MnO}_3$ (LCMO 30) by M. Fath and collaborators [102], show evidence of the existence of micron-sized metallic FM clusters inside an AF/PM matrix.

Within the phase separated picture, some studies point at the existence of mixtures/cooperative interactions/and or competition of/between the CE-type $\text{Mn}^{3+}/\text{Mn}^{4+}$ and either charge-/orbital/spin-ordered states (CO-OO-SO) states. In this context, neutron scattering measurements by P. Dai and collaborators [103] and Adams *et. al.* [104] suggest that charge localization—which promotes insulating behavior in this peculiar ground state—is likely related to nanometer-size short-range charge ordering (CO). They found evidence that CE-type CO exists in the FM insulating regime of $\text{La}_{1-x}\text{Ca}_x\text{MnO}_3$ (LCMO). Theoretical studies by Hotta and Dagotto [105] and Mizokawa *et. al.*, [106] also proposed CO in order to explain the FM-insulating ground state. The former study concluded that $\text{Pr}_{75}\text{Ca}_{25}\text{MnO}_3$ (PCMO 25) becomes a FM-insulator due to a CO consisting of a checkerboard charge ordered plane and a purely Mn^{3+} plane stacking alternately along the z-axis while Mizokawa *et al.* findings show evidence that the FM insulating ground state in PCMO 25 is realized due to the existence of orbital polarons. In the latter, Mn^{4+} ions are surrounded by FM coupled Mn^{3+} ions. However, neither type of the above mentioned CO states have been experimentally detected so far. On the other hand, Kajimoto and collaborators [107] report on their neutron scattering and theoretical investigations evidence that rejects CO as possible FM insulating phase interpretations. Instead, their findings are consistent of a staggered type orbital ordered (OO) state. Other studies using resonant x-ray scattering support this OO state scenario. As an example, Zimmermann *et. al.*[92] reported an

OO state in PCMO 25 to be similar to that present in the parent compound of LCMO. However, in LaMnO_3 , the OO is accompanied by AFM spin ordering rather than by a FM order, as is the case for PCMO. Recently, soft x-ray scattering results on the small- W PCMO system by Zhou and collaborators [108] reported evidence of the cooperative interplay between the FM-I and spin ordering (SO) right at the transition between the FM insulating phase and the regime where CMR is observed.

On the other hand, electron magnetic resonance (EMR) [109, 110] transport measurements [111, 112], nuclear magnetic resonance (NMR) [113], inelastic neutron scattering [114], neutron powder diffraction [115], and x-ray absorption [116] studies indicate that the emergence of an insulating, as opposed to a metallic FM ground state, could be the result of local structural changes—i.e., Jahn-Teller (JT) distortions that would promote electron localization.

Alternatively recent experiments on the FM-insulating phase of the CMR manganites strongly suggest that a closer look at the competing interactions and specifically at magnetism might explain the peculiar insulating behavior in this regime. For example, the low-wave vector excitations in LCMO are well behaved spin waves with a stiffness constant of $D \sim 50 \text{ meV-}\text{\AA}^2$ [114, 117] which is about 1/3 of the typical spin wave stiffness constants in the FM metallic state of CMR manganites [107, 118]. Moreover, in his neutron scattering study, P. Dai *et. al.* [117] attest to the fact that the spin dynamics in the FM insulating ground state of LCMO exhibits properties that are inconsistent with current Heisenberg or DE models and leaves readers to ponder the possibility that this anomalous behavior in the spin excitation spectrum could be induced by the nanometer-size short-range charge ordering (CO) reported in his previous work [103]. Similar values for the spin wave stiffness constant in the FM insulating phase of PCMO25 ($\sim 60 \text{ meV-}\text{\AA}^2$) have been found in the work of Kajimoto *et.al.* [107]. In his own words: ‘*this fact*

[similarity of the spin-wave stiffness value in low-doped perovskite manganites] *evidences the common ground of the FM-insulating phase of the manganites.*'

Furthermore, not only the low-wave vector excitations are interesting but also as the wave-vector increases, the spin waves have been reported to be broad and exhibit unusual behavior. In this context, some NMR studies [112, 113, 119] have suggested the possibility that the unusual magnetic and transport properties could be the result of a mixture of FM insulating (distorted and non-conducting) and (DE) FM metallic. For this to be possible, a new FM coupling mechanism—i.e., FM super-exchange (SE)—would be required in order to successfully explain the electron localization in the system (see Figure 6.1). Recall that the typical SE interaction (as dictated by the Pauli exclusion principle) is usually characterized by the antiferromagnetic (AF) coupling between two next-to-nearest neighbors cations (in our case SE could be between either $\text{Mn}^{3+}/\text{Mn}^{3+}$ or $\text{Mn}^{4+}/\text{Mn}^{4+}$) mediated by a non-magnetic anion (e.g. O^{2-}) (see Figure 6.1).

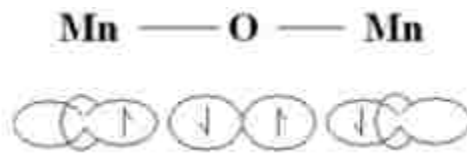


FIGURE 6.1 Schematic representation of the Super Exchange mechanism. For a detailed explanation refer to the text.

Supporting the a picture governed by FM SE, are the magnetic and transport measurements reported by Wanjun Jiang *et. al.*, [120]. Their work revealed the presence of OO-stabilized FM-SE and DE linked sites as the system evolves from FM insulating to FM-metallic. This emerging consensus—that the relevant interaction initiating magnetism in the insulating phase is SE—is reflected by the latest investigations (at the time of writing) using synchrotron x-ray and neutron diffraction [121] as well as by inelastic neutron scattering [122 – 124] work. In particular,

Hennion *et al.* [124] have reported the observation of broad modes and gaps in the spin wave dispersion of LCMO ($x = 0.17$ and 0.20) along high symmetry directions (Figure 6.2 (a)). The gaps observed were attributed to independent energy levels described as “quantized” flat modes. These q -independent energy levels have been described as standing spin waves embedded in an assembly of nano-sized FM domains with SE coupling (due to ‘hole-poor domains’). The latest inelastic neutron scattering investigation (at the time of writing) from Petit *et al.* [123] on the FM insulating phase of $\text{La}_{1-x}(\text{Sr,Ca})_x\text{MnO}_3$ confirms the existence of such quantized spin waves in small FM clusters (Figure 6.2 (b)) but reveals the existence of long-range ordering of such domains.

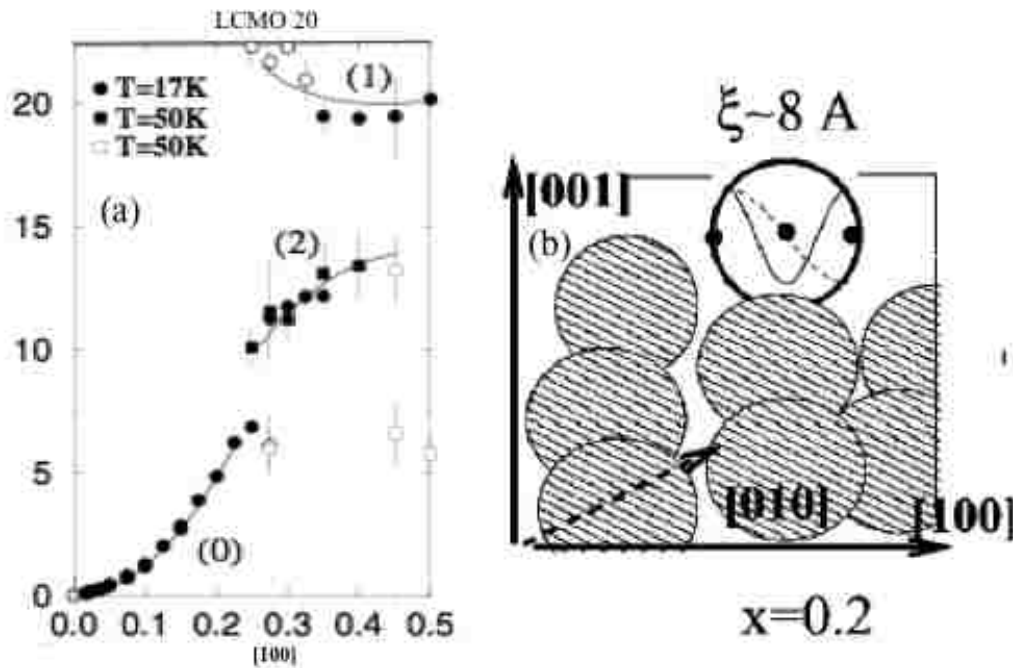


FIGURE 6.2 Anomalous spin wave behavior and ferromagnetic domains (FM) with superexchange (SE) couplings reported from neutron scattering experiments. (a) Magnetic excitations (“quantized flat modes”) measured along $[1+q, 0, 0]$ reported by Hennion *et al.* [122]. Solid and open circles correspond to main and weak intensities, respectively. (b) Standing spin waves embedded in an assembly of nano-sized FM domains with SE coupling and long-range ordering [123, 124].

Motivated by the possible role that magnetism and competing interactions might play on the FM-I phase of manganites and thus on the CMR effect, we report in this chapter a preliminary inelastic neutron scattering study on the spin and lattice excitations in the FM-Insulating phase of LCMO 20.

6.2 Experimental Details

We have characterized the unusual behavior that has been reported of the spin wave excitation spectrum found in the low- T insulating ground state of these manganite systems. We measured the spin wave excitation spectrum on a high quality single crystal of $\text{La}_{0.80}\text{Ca}_{0.20}\text{MnO}_3$ ($\sim 0.4 \text{ cm}^3$ in volume, $T_C = 180 \text{ K}$) provided by Y. Tokura's group and grown by the floating zone method [62]. This unpolarized thermal neutron scattering experiment was performed at the High Flux Isotope Reactor at Oak Ridge National Laboratory using the HB-1 Triple Axis Spectrometer. The final neutron energy was fixed at $E_f = 14.7 \text{ meV}$ while the analyzers, filters, and monochromator were all pyrolytic graphite (PG) single crystals yielding an energy resolution at the FWHM $\sim 1.1 \text{ meV}$. Our measurements were made in constant transfer \mathbf{Q} mode where $\mathbf{Q} = \mathbf{G} + \mathbf{q}$ and \mathbf{G} as the reciprocal lattice vector. The components of the wave vector $\mathbf{Q} = (Q_x, Q_y, Q_z)$ are in units of \AA^{-1} and $(H, K, L) = (Q_x a / 2\pi, Q_y a / 2\pi, Q_z a / 2\pi)$ is in the reciprocal lattice units (r.l.u). The samples were aligned to allow the wave vector in the form of $(H, K, 0)$ accessible in the horizontal scattering plane. For this 20% doped sample all wave vectors are labeled in terms of the pseudo cubic unit cell with lattice parameters of $a = 3.86 \text{\AA}$.

Measurements of the spin wave excitation spectra were taken along the $q = [\xi, 0, 0]$ directions in the first and second Brillouin zones (BZ) at 5 K and 255 K, respectively. The obtained neutron counts vs. energy scans were normalized using a linear background and fitted

to a Gaussian profile (long-range order). Shown in Figure 6.3 are the probed peak positions and scan direction (denoted by arrows) in reciprocal space.

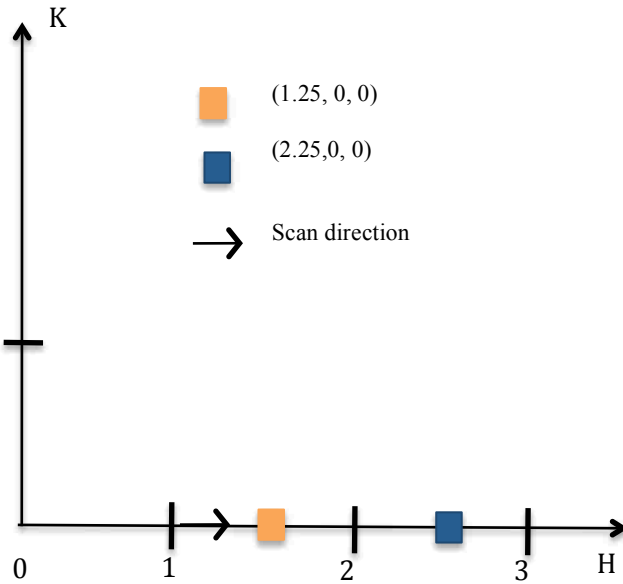


FIGURE 6.3 Schematic diagram of probed peak positions and scan direction (denoted by the black arrow) in reciprocal space.

6.3 Spin-Lattice Coupling

The top panel of Figure 6.4 shows the colour plot (a) and dispersion relation (b) of the spin and lattice excitations in the first Brillouin zone at base temperature. Shown at the bottom panel are representative intensity profiles of the magnon (sw) and phonon excitation spectra for the (1.25, 0, 0) and (1.30, 0, 0) scattering wave vectors from which the dispersion relation (shown in (b)) was obtained.

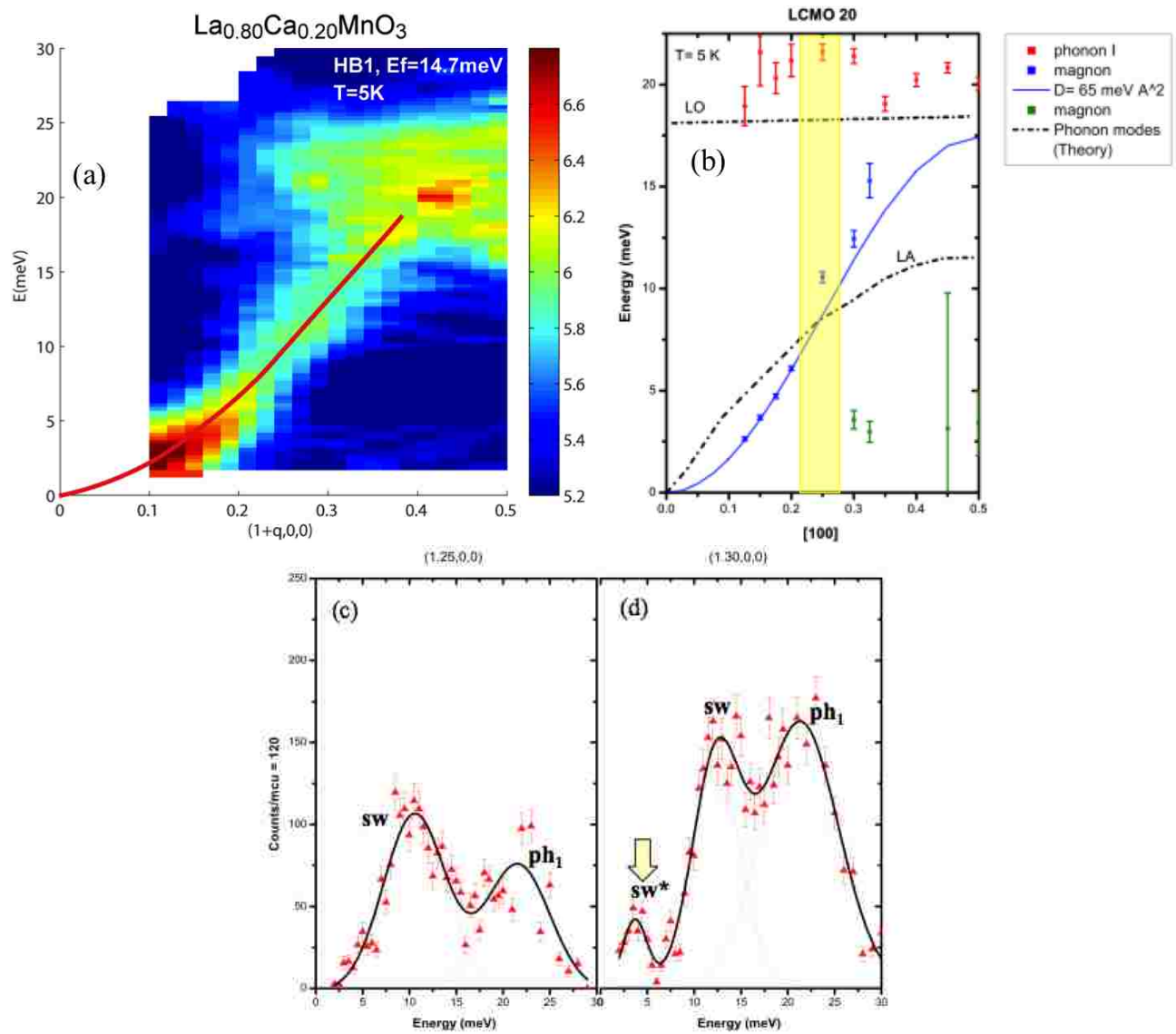


FIGURE 6.4 Experimental results on the LCMO20 single crystal specimen. Top panel (a) colour plot (line is just a guide to the eye) and dispersion relation (b) of the spin and lattice excitations in the first Brillouin zone at base temperature. In (b) from top to bottom: red data points ~ 20 meV correspond to a longitudinal optical (LO) phonon mode, the green ones are very weak spin wave excitations that became more prominent for values of $q \geq 0.3$, the spin-wave dispersion relation is fitted (guide to the eye) in blue on (b) using a known spin-wave stiffness constant value from previous studies [114, 117] while the segmented black lines are theoretical phonon modes reported on [125]. Bottom panel (c) and (d) display the magnon (sw) and phonon (ph) excitation spectra for (1.25,0,0) and (1.30,0,0) for the 1st B.Z. normalized to a linear background and fitted with a Gaussian. The yellow arrow denotes the appearance of a new spin wave branch shown near the highlighted region in (b).

The intensity of the colour plot taken at 5 K clearly shows two significantly different regions, one at low q and small values of E and another one for values of $q \geq 0.3$ located at values of $E \sim 20$ meV. This is in agreement with polarized neutron scattering studies [117] reported by P.Dai and collaborators, where an anomalous softening and broadening of magnons was found to exist in LCMO 30 near the zone boundary. Similarly to what we have observed, they reported that magnons soften and broaden considerably in the vicinity of $E = 20$ meV.

The dispersion relation (E vs. q) obtained at the base temperature of 5K is shown on Figure 6.4 (b). From top to bottom, the red data points correspond to a longitudinal optical (LO) phonon mode ($E = 20$ meV). The spin wave dispersion relation is represented by the blue data points, which are fitted (only to serve as a guide to the eye) in blue using a known spin wave stiffness constant reported for the FM insulating phase of PCMO25 (~ 60 meV-Å²) [107]. The green data points were determined to be very weak spin wave excitations that became more prominent for values of $q \geq 0.3$. Theoretical phonon modes reported on [125, 126] have been added to this plot as segmented black lines (the purpose of this will be explained later). Two interesting features are to note in this dispersion relation. The first one being the section highlighted in yellow for values of $0.2 \leq q \leq 0.3$, which is where a new spin wave excitations (green data points) first develop. And the second is the fact that at those same values of q , the longitudinal acoustic phonon mode reported in the theory crosses our spin wave dispersion curve, thus providing evidence of the spin-lattice coupling in the FM-I phase of manganites.

In order to better understand the physics of the region highlighted in yellow on figure 6.4 (b), we show the magnon (sw) and phonon (ph) excitation spectra in the first Brillouin zone at (1.25, 0, 0) and (1.30, 0, 0) scattering wave vectors. For $q = 0.25$ we observe a magnon at $E \sim 10$ meV and a phonon close to $E \sim 20$ meV. As the vector q increases, we see the evolution of these two

peaks as well as the addition of a new magnon at even lower energies $E \sim 5$ meV. This spin wave shows significant broadening and as a result (see the large error bar) and at this point in the investigation no further assertions can be made about its appearance or behavior, other than it is a feature of the excitation spectra and it appears in the vicinity of where there is the possibility of spin-lattice coupling.

Phonon/spin wave excitations along the $[1,0,0]$ direction in the 2nd B.Z ($T = 5$ K) are presented in Figure 6.5 (a). Similarly to the measurements taken at the 1st BZ shown in Figure 6.4 (b), we find a spin wave branch (blue data points) that becomes increasingly over-damped as the wave-vector increases. We also observe a longitudinal optical phonon (LO) centered around $E = 20$ meV (red data points) as well as a spin wave branch showing severe broadening (blue fit just as a guide to the eye) in the vicinity of this LO phonon. The yellow and purple data points represent longitudinal acoustical (LA) phonon modes that become prominent only when we measured in the second zone. In addition, we have also included the theoretical phonon modes (segmented black lines) reported in the literature [125, 126] for this BZ.

Comparing our results side by side with those from Figure 6.2 (a) (shown here as 6.5 (b) for side by side comparison purposes), we see that we do observe similar branches and energies ranges. However, unlike Hennion *et al.*, [124] we believe these observations to be indicative of a strong “magneto-elastic coupling”, i.e., of a strong spin-lattice interaction [118, 127 – 130] since what they refer to as quantized flat modes appear to be phonon branches in our spin wave dispersion relation. Upon comparison (both plots have the same scale), our results indicate that these gaps at specific values of q emerge in the vicinity of the crossing of a phonon mode (either black-segmented line theoretically predicted and both purple/yellow phonon dispersion experimentally obtained) with the spin wave dispersion.

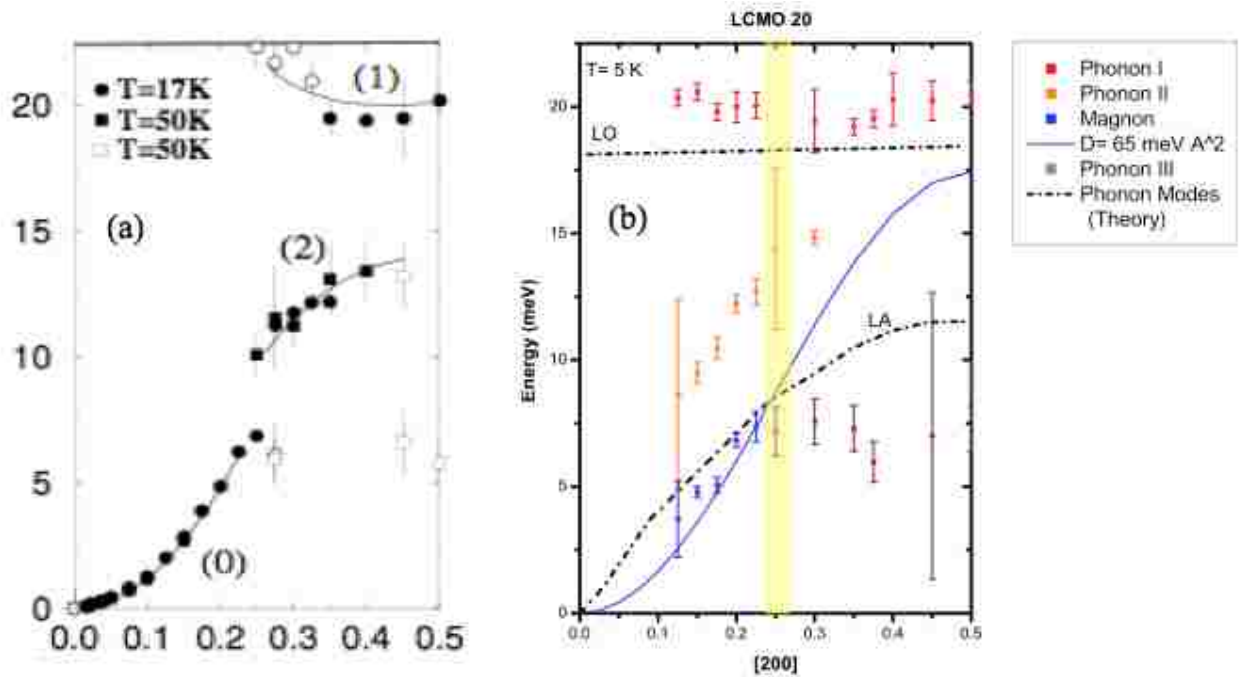


FIGURE 6.5 Spin wave dispersion relations of our experimental results and previously reported ones. (a) Magnetic excitations (“quantized flat modes”) measured along $[1+\xi, 0, 0]$ reported by Hennion *et al.* [124] are shown in (16b). Solid and open circles correspond to main and weak intensities, respectively. (b) Our experimental results (from top to bottom) red data points ~ 20 meV correspond to a longitudinal optical (LO) phonon mode, the yellow ones are from a longitudinal acoustic (LA) phonon mode, the spin-wave dispersion relation is fitted (guide to the eye) in blue on using a known spin-wave stiffness constant value from previous studies [see text], the data points in purple represent a phonon mode evident only in $[200]$ while the segmented black lines are theoretical phonon modes reported on [125].

It is appropriate to mention as well that recent theoretical studies of the spin wave excitation [131] reported by Tai-Ming Cheng and Lin Li found evidence of a strong spin-lattice coupling. By employing the lattice dynamics as opposed to the long wave approximation for a two dimensional Heisenberg FM system, they have investigated the spin wave excitation under a magnon-phonon coupling scenario. Under these conditions, they found magnon softening in these systems and they attribute it to magnon-phonon coupling, spin wave stiffness constant,

among other factors. Specifically, their results indicate that the longitudinal phonon (LO) absorbs energy from magnon, thus resulting in a mere hardening of the phonon's dispersion curve.

6.4 Summary

Even though we are at very early stages of the investigation, our preliminary measurements of spin and lattice excitations in the FM-I phase of the prototype CMR manganite $\text{La}_{1-x}\text{Ca}_x\text{MnO}_3$ shows clear evidence that 1) the spin-wave dispersion seems to be characterized by broad modes and anomalous behavior, particularly at large wave vectors, and 2) magnon-phonon coupling might be a driving force behind the gaps (quantized flat modes) reported to dominate the spin-wave dispersion. Thus, the results of this investigation indicate that spin-lattice coupling plays an important role in the FM insulating phase and thus could be relevant to the large CMR effect that characterizes these perovskite manganite

6.5 Future Work

The current status of the research and our preliminary inelastic neutron scattering results on the FM insulating ground state of doped perovskite manganites strongly suggest the need for a comprehensive and systematic study of the competing interactions, and magnetism in order to understand the nature of the FM insulating phase.

At the time of writing this thesis, only preliminary studies could be completed. However, we had set forth a research plan that included inelastic, elastic, quasi-elastic and polarized neutron scattering experiments as well as the use of advanced transmission electron microscopy (TEM) techniques as a complimentary probe in order to be able to fully characterize the FM-I phase present in CMR manganites.

Because neutron scattering allows for the determination of magnetic excitations and fluctuations like no other condensed matter probe, it is the main experimental technique chosen

to complete this study. Preliminary measurements have been taken on LCMO, however, experiments will be conducted on the truly small- W system of PCMO as well. Both PCMO and LCMO single crystals exhibit a FM insulating ground state in the range of $0.15 < x < 0.30$ and $0.1 < x < 0.25$, respectively. However, in contrast to LCMO, PCMO has a larger JT distortion and since the ionic size of Pr^{3+} is almost identical to Ca^{2+} it also has negligible quenched disorder. Thus, the selection of these two model systems allows us to characterize the effect of static/dynamic JT distortion and quenched disorder on the insulating character of the FM insulating ground state.

Our goal is to perform a systematic study of the competing interactions and coupling in the FM insulating phase in these CMR manganites. To this extent, we will carry out a series of elastic neutron scattering experiments to measure the evolution of possible isotropic/anisotropic AFM spin clusters in the FM insulating phase. From these elastic neutron scattering measurements, we will obtain the diffuse scattering profile and will be able to observe superlattice peaks and the lattice distortions due to CO and OO. The peaks will be analyzed and fitted appropriately in order to reveal cluster size, lifetime, as well as their evolution with temperature. The anomalous spin wave behavior will be studied from inelastic neutron scattering experiments as we have done for the FM metallic phase of manganites presented in Chapter 5. Polarized inelastic neutron scattering experiments will be crucial in order to identify the phonon and spin wave contributions to verify/dismiss the magnon-phonon coupling observed in the preliminary experiments. In the case of LCMO ($x = 0.2$), the broad feature around 20 meV present in the dispersion relation (believed to be a LO phonon mode) will be carefully addressed, especially at higher wave vectors with the aim of determining the possible mixing/coupling of the magnon and phonon modes. The second set of experiments will consist of inelastic neutron scattering

studies aimed at obtaining the spin wave dispersion relations along high-symmetry directions at low temperatures as well as the temperature dependence (across the FM insulating transition) of the spin wave stiffness for order parameter behavior for other doping concentrations of LCMO and PCMO. From the magnon dispersion relation, we can estimate the spin-exchange interaction, which is affected by the OO due to the anisotropic character of the e_g orbital and compare it to existing models and thus characterize the orbital state.

In order to further investigate the phase separation scenario—e.g. the possible existence of FM clusters such as those proposed by Hennion *et. al.*, [122] or the segregation of insulating and metallic phases due to CO and/or OO—we would like to use advanced transmission electron microscopy techniques (TEM). From TEM and quasi-elastic neutron scattering measurements we will be able to obtain local structural and electronic phase information in real space and average local phase correlations in momentum space, respectively. Thus, the combination of these two techniques will result in a powerful and comprehensive approach towards the study of nanoscale phase separation and inhomogeneity.

Chapter 7

Conclusions

In this dissertation magnetism and local correlation in manganese-substituted ruthenium oxides and hole-doped manganese oxides were investigated using elastic and inelastic neutron scattering.

Studies on single crystals of Mn-substituted $\text{Sr}_3\text{Ru}_2\text{O}_7$ ($x = 0.16$ and 0.125) have revealed a long-range *E*-type AFM spin arrangement in the ground state characterized by 1) a commensurate propagation wave vector of $(0.5, 0, 0)$ along the basal plane with moments aligned along the *c*-direction, and 2) only one single-bilayer ferromagnetic correlations out of plane. The evolution of the magnetic structure as a function of doping concentration has uncovered a non-linear doping dependence of the in-plane correlation of the *E*-type AFM structure. That is, while increasing Mn-substitution in the parent compound stabilizes the long-range *E*-type AFM spin arrangement along the basal plane, the correlation length jumps by a factor ≥ 10 unit cells from the 12.5 % to the 16 % Mn concentration. Demonstrating in this way the vital role that competing interactions play in these materials; one is simple unable to predict the impact that changing Mn by only a few percent will have on the magnetism of the system.

Experiments carried out on the colossal magnetoresistive manganite $\text{Pr}_{1-x}\text{Ca}_x\text{MnO}_3$ ($x = 0.3$, 0.35 and 0.4) indicate that the charge-/orbital-ordered (CO-OO) ground state not only evolves as a function of doping but it also shows a strong doping dependence of the magnetic phase separation in this system. That is, our analysis on the ferromagnetic, antiferromagnetic, and CO-OO correlations have provided direct indication that the CO-OO state is indeed phase separated and of the existence of a critical doping concentration close to $x = 0.35$ that divides the inhomogeneous from homogeneous CO state.

A preliminary investigation of spin and lattice excitations in the ferromagnetic insulating (FM-I) ground state of the perovskite manganite $\text{La}_{1-x}\text{Ca}_x\text{MnO}_3$ ($x = 0.20$) suggests that magnon-phonon coupling could be responsible for the anomalous behavior of the spin wave spectra reported in these systems. Albeit in its infancy, these results might help explain the nature of the FM-I insulating ground state, which is the precursor to the ferromagnetic metallic state where the colossal magnetoresistive effect is observed.

Our work sheds light on the understanding of the complexity of magnetism and of the competing interactions present in ruthenates and manganite systems from which exotic phenomena such as colossal magnetoresistance, quantum criticality, and high temperature superconductivity emerge.

References

- [1] D. Mesa, F. Ye, S. Chi, J. A. Fernandez-Baca, W. Tian, B. Hu, R. Jin, E. W. Plummer, and J. Zhang, *Physical Review B* **85**, 180410(R) (2012). (<http://link.aps.org/abstract/PRB/v85/p180410>). Copyright (2012) by the American Physical Society.
- [2] H. Sha, F. Ye, P. Dai, J. Fernandez-Baca, D. Mesa, J. Lynn, Y. Tomioka, Y. Tokura, and J. Zhang, *Physical Review B* **78**, 052410 (2008). (<http://link.aps.org/abstract/PRB/v78/p052410>). Copyright (2008) by the American Physical Society.
- [3] M. Imada, A. Fujimori, and Y. Tokura, *Reviews of Modern Physics* **70**, 1039 (1998).
- [4] S. A. Grigera, R. S. Perry, A. J. Schofield, M. Chiao, S. R. Julian, G. G. Lonzarich, S. I. Ikeda, Y. Maeno, A. J. Millis, and A. P. Mackenzie, *Science* **294**, 329 (2001).
- [5] Y. Tomioka and Y. Tokura, *Physical Review B* **66**, 104416 (2002).
- [6] S. Nakatsuji and Y. Maeno, *Phys. Rev. Lett.* **84**, 2666 (2000).
- [7] J. Paglione and R. L. Greene, *Nature Physics* **6**, 645 (2010).
- [8] R. A. Borzi, S. A. Grigera, J. Farrell, R. S. Perry, S. J. S. Lister, S. L. Lee, D. A. Tennant, Y. Maeno, and A. P. Mackenzie, *Science* **315**, 214 (2007).
- [9] F. Weber, D. N. Argyriou, O. Prokhnenko, and D. Reznik, *Physical Review B* **88**, 241106(R) (2013).
- [10] F. Ye, J. Fernandez-Baca, P. Dai, J. Lynn, H. Kawano-Furukawa, H. Yoshizawa, Y. Tomioka, and Y. Tokura, *Physical Review B* **72**, 212404 (2005).
- [11] S. Nakatsuji and Y. Maeno, *Phys. Rev. Lett.* **84**, 2666 (2000).
- [12] O. Friedt, M. Braden, G. André, P. Adelman, S. Nakatsuji, and Y. Maeno, *Physical Review B* **63**, 174432 (2001).
- [13] Y. Kamihara, T. Watanabe, M. Hirano, and H. Hosono, *J. Am. Chem. Soc.* **130**, 3296 (2008).
- [14] N. W. Ashcroft and N. D. Mermin, *Solid State Physics* (Holt, Rinehart and Winston, 1976).
- [15] P. Fazekas, *Lecture Notes on Electron Correlation and Magnetism* (World Scientific, 2003).

- [16] E. Dagotto, T. Hotta, and A. Moreo, *Physics Reports* **1** (2001).
- [17] E. Dagotto, *Nanoscale Phase Separation and Colossal Magnetoresistance* (Springer-Verlag Berlin Heidelberg, New York, 2003).
- [18] T. Chatterji, *Colossal Magnetoresistive Manganites* (Kluwer Academic, 2004).
- [19] T. Bruckel, G. Heger, D. Richter, and R. Zorn, editors, *Lectures of the JCNS Laboratory Course on Neutron Scattering* (Forschungszentrum Julich GmbH, 2008).
- [20] P. A. Cox, *Transition Metal Oxides* (Oxford University Press, 1992).
- [21] M. Gerloch and R. C. Slade, *Ligand-Field Parameters* (Cambridge, London, 1973).
- [22] Y. Tokura and N. Nagaosa, *Science* **288**, 462 (2000).
- [23] S. N. Ruddlesden and P. Popper, *Acta Crystallographica* **11**, 54 (1958).
- [24] S. N. Ruddlesden and P. Popper, *Acta Crystallographica* **10**, 538 (1957).
- [25] A. P. Mackenzie and Y. Maeno, *Reviews of Modern Physics* **75**, 657 (2003).
- [26] Y. Maeno, H. Hashimoto, K. Yoshida, S. Nishizaki, T. Fujita, J. G. Bednorz, and F. Lichtenberg, *Nature* **372**, 532 (1994).
- [27] P. B. Allen, H. Berger, O. Chauvet, L. Forro, T. Jarlborg, A. Junod, B. Revaz, and G. Santi, *Physical Review B* **53**, 4393 (1996).
- [28] L. Klein, J. S. Dodge, C. H. Ahn, G. J. Snyder, T. H. Geballe, M. R. Beasley, and A. Kapitulnik, *Phys. Rev. Lett.* **77**, 2774 (1996).
- [29] R. Borzi, S. Grigera, R. Perry, N. Kikugawa, K. Kitagawa, Y. Maeno, and A. Mackenzie, *Phys. Rev. Lett.* **92**, 216403 (2004).
- [30] F. Ronning, R. Hill, M. Sutherland, D. Hawthorn, M. Tanatar, J. Paglione, L. Taillefer, M. Graf, R. Perry, Y. Maeno, and A. Mackenzie, *Phys. Rev. Lett.* **97**, 067005 (2006).
- [31] P. Gegenwart, F. Weickert, M. Garst, R. Perry, and Y. Maeno, *Phys. Rev. Lett.* **96**, 136402 (2006).
- [32] K. Iwaya, S. Satow, T. Hanaguri, N. Shannon, Y. Yoshida, S. Ikeda, J. He, Y. Kaneko, Y. Tokura, T. Yamada, and H. Takagi, *Phys. Rev. Lett.* **99**, 057208 (2007).
- [33] A. Tamai, M. Allan, J. Mercure, W. Meevasana, R. Dunkel, D. Lu, R. Perry, A. Mackenzie, D. Singh, Z. X. Shen, and F. Baumberger, *Phys. Rev. Lett.* **101**, 026407 (2008).

- [34] B. Binz and M. Sigrist, *Europhys. Lett.* **65**, 816 (2007).
- [35] R. Perry, L. Galvin, S. Grigera, L. Capogna, A. Schofield, A. Mackenzie, M. Chiao, S. Julian, S. Ikeda, S. Nakatsuji, Y. Maeno, and C. Pfleiderer, *Phys. Rev. Lett.* **86**, 2661 (2001).
- [36] R. Perry, K. Kitagawa, S. Grigera, R. Borzi, A. Mackenzie, K. Ishida, and Y. Maeno, *Phys. Rev. Lett.* **92**, 166602 (2004).
- [37] S. A. Grigera, P. Gegenwart, R. A. Borzi, F. Weickert, A. J. Schofield, R. S. Perry, T. Tayama, T. Sakakibara, Y. Maeno, A. G. Green, and A. P. Mackenzie, *Science* **306**, 1154 (2004).
- [38] S. Ikeda, Y. Maeno, S. Nakatsuji, M. Kosaka, and Y. Uwatoko, *Physical Review B* **62**, 6089(R) (2000).
- [39] S.-I. Ikeda, Y. Maeno, S. Nakatsuji, M. Kosaka, and Y. Uwatoko, *Physical Review B* **62**, 6089(R) (2012).
- [40] Q. Huang, J. W. Lynn, R. W. Erwin, J. Jarupatrakorn, and R. J. Cava, *Physical Review B* **58**, 8515 (1998).
- [41] L. Capogna, E. Forgan, S. Hayden, A. Wildes, J. Duffy, A. Mackenzie, R. Perry, S. Ikeda, Y. Maeno, and S. Brown, *Physical Review B* **67**, 012504 (2003).
- [42] M. Stone, M. Lumsden, R. Jin, B. Sales, D. Mandrus, S. Nagler, and Q. YY, *Physical Review B* **73**, 174426 (2006).
- [43] K. Kitagawa, K. Ishida, R. Perry, T. Tayama, T. Sakakibara, and Y. Maeno, *Phys. Rev. Lett.* **95**, 127001 (2005).
- [44] O. Friedt, P. Steffens, M. Braden, Y. Sidis, S. Nakatsuji, and Y. Maeno, *Phys. Rev. Lett.* **93**, 147404 (2004).
- [45] B. Hu, G. T. McCandless, V. O. Garlea, S. Stadler, Y. Xiong, J. Y. Chan, E. W. Plummer, and R. Jin, *Physical Review B* **84**, 174411 (2011).
- [46] R. Mathieu, A. Asamitsu, Y. Kaneko, J. He, X. Yu, R. Kumai, Y. Onose, N. Takeshita, T. Arima, H. Takagi, and Y. Tokura, *Physical Review B* **72**, 092404 (2005).
- [47] M. A. Hossain, B. Bohnenbuck, Y. D. Chuang, M. W. Haverkort, I. S. Elfimov, A. Tanaka, A. G. Cruz Gonzalez, Z. Hu, H. J. Lin, C. T. Chen, R. Mathieu, Y. Tokura, Y. Yoshida, L. H. Tjeng, Z. Hussain, B. Keimer, G. A. Sawatzky, and A. Damascelli, *Physical Review B* **86**, 041102 (2012).

- [48] C. Zener, *Physical Review* **82**, 403 (1951).
- [49] P. W. Anderson and H. Hasegawa, *Physical Review* **100**, 675 (1955).
- [50] Y. Tomioka, A. Asamitsu, H. Kuwahara, Y. Moritomo, and Y. Tokura, *Physical Review B* **53**, 1689(R) (1996).
- [51] S. W. Cheong and H. Y. Hwang, *Contribution to Colossal Magnetoresistance Oxides, Monographs in Condensed Matter Science* (Gordon & Breach, London, 1999).
- [52] P. Schiffer, A. P. Ramirez, W. Bao, and S. W. Cheong, *Phys. Rev. Lett.* **75**, 3336 (1995).
- [53] E. Dagotto, *Science* **309**, 257 (2005).
- [54] R. Pynn, LANSCE, Los Alamos Neutron Science Center (Www.Mrl.Ucsb.Edu/~Pynn) (1990).
- [55] G. Shirane, S. M. Saphiro, and J. M. Tranquada, *Neutron Scattering with a Triple-Axis Spectrometer Basic Techniques* (Cambridge University Press, New Work, 2002).
- [56] A. Furrer, J. Mesot, and T. Strassle, *Neutron Scattering in Condensed Matter Physics* (World Scientific, 2009).
- [57] G. L. Squires, *Introduction to the Theory of Thermal Neutron Scattering* (Dover Publications, INC, Mineola, New York, 1978).
- [58] G. E. Bacon, *Neutron Diffraction* (Clarendon Press Oxford, 1975).
- [59] W. Marshall and S. W. Lovesey, *Theory of Thermal Neutron Scattering* (Oxford University Press, New York, 1971).
- [60] B. T. M. Willis and C. J. Carlile, *Experimental Neutron Scattering* (Oxford University Press, New York, 2009).
- [61] Y. Tomioka, A. Asamitsu, H. Kuwahara, Y. Moritomo, and Y. Tokura, *Physical Review B* **53**, R1689 (1996).
- [62] T. Okuda, Y. Tomioka, A. Asamitsu, and Y. Tokura, *Physical Review B* **61**, 8009 (2000).
- [63] R. T. Azuah, L. R. Kneller, Y. Qiu, P. L. W. Tregenna-Piggott, C. M. Brown, J. R. D. Copley, and R. M. Dimeo, *Journal of Research of the National Institute of Standards and Technology* **114**, 341 (2009).

- [64] J. Lynn, D. Argyriou, Y. Ren, Y. Chen, Y. Mukovskii, and D. Shulyatev, *Physical Review B* **76**, 014437 (2007).
- [65] B. M. Brockhouse, *Reviews of Modern Physics* 735751 (1996).
- [66] J. W. Lynn, Y. Chen, S. Chang, Y. Zhao, S. Chi, W. Ratcliff II, B. G. Ueland, and R. W. Erwin, *Journal of Research of the National Institute of Standards and Technology* **117**, 60 (2012).
- [67] H. Rietveld, *Acta Crystallographica* **22**, 151 (1967).
- [68] H. Rietveld, *Journal of Applied Crystallography* **2**, 65 (1969).
- [69] R. A. Young, editor, *The Rietveld Method* (Oxford University Press, 1996).
- [70] J. Rodriguez-Carvajal, *Physica B: Condensed Matter* **192**, 55 (1993).
- [71] M. A. Hossain, I. Zegkinoglou, Y. D. Chuang, J. Geck, B. Bohnenbuck, A. G. C. Gonzalez, H. H. Wu, C. Schüßler-Langeheine, D. G. Hawthorn, J. D. Denlinger, R. Mathieu, Y. Tokura, S. Satow, H. Takagi, Y. Yoshida, Z. Hussain, B. Keimer, G. A. Sawatzky, and A. Damascelli, *Sci. Rep.* **3**, (2013).
- [72] B. Hu, G. T. McCandless, M. Menard, V. B. Nascimento, J. Y. Chan, E. W. Plummer, and R. Jin, *Physical Review B* **81**, 184104 (2010).
- [73] H. Shaked, J. D. Jorgensen, O. Chmaissem, S. Ikeda, and Y. Maeno, *Journal of Solid State Chemistry* **154**, 361 (2000).
- [74] P. Steffens, J. Farrell, S. Price, A. Mackenzie, Y. Sidis, K. Schmalzl, and M. Braden, *Physical Review B* **79**, 054422 (2009).
- [75] L. Fisher, *Reports on Progress in Physics* **30**, 615 (1967).
- [76] Z. Fang and K. Terakura, *Physical Review B* **64**, 020509 (2001).
- [77] J. B. Goodenough, *Physical Review* **100**, 564 (1955).
- [78] E. O. Wollan and W. C. Koehler, *Physical Review* **100**, 545 (1955).
- [79] P. G. De Gennes, *Physical Review* **118**, 141 (1960).
- [80] Z. Jirak, S. Krupicka, V. Nekvasil, E. Pollert, G. Villeneuve, and F. Zounove, *J. Magn. Mater* **15-18**, 519 (1980).
- [81] Y. Tokura, H. Kuwahara, Y. Morimoto, Y. Tomioka, and A. Asamitsu, *Phys. Rev. Lett.* **76**, 3184 (1996).

- [82] Z. Jirak, S. Krupicka, Z. Simsa, M. Dlouha, and Z. Vratilav, *J. Magn. Magn. Mater* **53**, 153 (1985).
- [83] A. Daoud-Aladine, J. Rodriguez-Carvajal, L. Pinsard-Gaudart, M. Fernández-Díaz, and A. Revcolevschi, *Phys. Rev. Lett.* **89**, 097205 (2002).
- [84] V. Ferrari, M. Towler, and P. Littlewood, *Phys. Rev. Lett.* **91**, 227202 (2003).
- [85] G. Zheng and C. Patterson, *Physical Review B* **67**, 220404(R) (2003).
- [86] J. S. Zhou and J. B. Goodenough, *Physical Review B* **62**, 3834 (2000).
- [87] D. V. Efremov, J. van den Brink, and D. I. Khomskii, *Nature Materials* **3**, 853 (2004).
- [88] E. Pollert, S. Krupicka, and E. Kuzmicova, *J. Phys. Chem. Solids* **43**, 1137 (1982).
- [89] T. Asaka, S. Yamada, S. Tsutsumi, C. Tsuruta, K. Kimoto, T. Arima, and Y. Matsui, *Phys. Rev. Lett.* **88**, 097201 (2002).
- [90] Y. Tokura, *Reports on Progress in Physics* **69**, 797 (2006).
- [91] D. E. Cox, P. G. Radaelli, M. Marezio, and S. W. Cheong, *Physical Review B* **57**, 3305 (1998).
- [92] M. Zimmermann, C. Nelson, Y. J. Kim, J. Hill, D. Gibbs, H. Nakao, Y. Wakabayashi, Y. Murakami, Y. Tokura, Y. Tomioka, T. Arima, C. C. Kao, D. Casa, C. venkataraman, and T. Gog, *Physical Review B* **64**, 064411 (2001).
- [93] J. Van de Brink and G. Khaliullin, *Phys. Rev. Lett.* **83**, 5118 (1999).
- [94] Z. Popović and S. Satpathy, *Phys. Rev. Lett.* **88**, 197201 (2002).
- [95] S. Grenier, J. Hill, D. Gibbs, K. Thomas, M. Zimmermann, C. Nelson, V. Kiryukhin, Y. Tokura, Y. Tomioka, D. Casa, T. Gog, and C. venkataraman, *Physical Review B* **69**, 134419 (2004).
- [96] C. Jooss, L. Wu, T. Beetz, R. F. Klie, M. Beleggia, M. Schofield, S. Schramm, J. Hoffmann, and Y. Zhu, *Pnas* **104**, 13597 (2007).
- [97] H. Yoshizawa, H. Kawano, Y. Tomioka, and Y. Tokura, *Physical Review B* **52**, 13145(R) (1995).
- [98] P. Radaelli, R. Ibberson, D. Argyriou, H. Casalta, K. Andersen, S. W. Cheong, and J. Mitchell, *Physical Review B* **63**, 172419 (2001).

- [99] J. Fernandez-Baca, P. Dai, H. Kawano-Furukawa, H. Yoshizawa, E. Plummer, S. Katano, Y. Tomioka, and Y. Tokura, *Physical Review B* **66**, 054434 (2002).
- [100] R. Kajimoto, T. Kakeshita, Y. Oohara, H. Yoshizawa, Y. Tomioka, and Y. Tokura, *Physical Review B* **58**, 837(R) (1998).
- [101] P. Abbamonte, *Physical Review B* **74**, 195113 (2006).
- [102] M. Fath, S. Freisem, A. Menovsky, Y. Tomioka, J. Aarts, and J. A. Mydosh, *Science* **285**, 1540 (1999).
- [103] P. Dai, J. A. Fernandez-Baca, Y. Wakabayashi, E. W. Plummer, Y. Tomioka, and Y. Tokura, *Phys. Rev. Lett.* **85**, 2553 (2000).
- [104] C. P. Adams, J. W. Lynn, Y. M. Mukovskii, A. A. Arsenov, and D. A. Shulyatev, *Phys. Rev. Lett.* **85**, 3954 (2000).
- [105] T. Hotta and E. Dagotto, *Physical Review B* **61**, 11879(R) (2000).
- [106] T. Mizokawa, D. Khomskii, and G. Sawatzky, *Physical Review B* **63**, 024403 (2000).
- [107] R. Kajimoto, H. Mochizuki, H. Yoshizawa, S. Okamoto, and S. Ishihara, *Physical Review B* **69**, 054433 (2004).
- [108] S. Y. Zhou, Y. Zhu, M. C. Langner, Y. D. Chuang, P. Yu, W. L. Yang, A. G. Cruz Gonzalez, N. Tahir, M. Rini, Y. H. Chu, R. Ramesh, D. H. Lee, Y. Tomioka, Y. Tokura, Z. Hussain, and R. W. Schoenlein, *Phys. Rev. Lett.* **106**, 186404 (2011).
- [109] V. Markovich, E. Rozenberg, A. Shames, G. Gorodetsky, I. Fita, K. Suzuki, R. Puzniak, D. Shulyatev, and Y. Mukovskii, *Physical Review B* **65**, 144402 (2002).
- [110] A. Shames, E. Rozenberg, G. Gorodetsky, and Y. Mukovskii, *Physical Review B* **68**, 174402 (2003).
- [111] J. Alonso, E. Herrero, J. M. Gonzalez-Calbet, M. Vallet-Regi, J. L. Martinez, J. M. Rojo, and A. Hernando, *Physical Review B* **62**, 11328 (2000).
- [112] P. Algarabel, J. De Teresa, J. Blasco, M. Ibarra, C. Kapusta, M. Sikora, D. Zajac, P. Riedi, and C. Ritter, *Physical Review B* **67**, 134402 (2003).
- [113] G. Papavassiliou, M. Fardis, M. Belesi, T. G. Maris, G. Kallias, M. Pissas, and D. Niarchos, *Phys. Rev. Lett.* **84**, 761 (2000).
- [114] G. Biotteau, M. Hennion, F. Moussa, J. Rodriguez-Carvajal, L. Pinsard, A. Revcolevschi, Y. Mukovskii, and D. Shulyatev, *Physical Review B* **64**, 104421 (2001).

- [115] M. Pissas, I. Margiolaki, G. Papavassiliou, D. Stamopoulos, and D. Argyriou, *Physical Review B* **72**, 064425 (2005).
- [116] Y. Jiang, F. Bridges, L. Downward, and J. Neumeier, *Physical Review B* **76**, 224428 (2007).
- [117] P. Dai, J. Fernandez-Baca, E. Plummer, Y. Tomioka, and Y. Tokura, *Physical Review B* **64**, 224429 (2001).
- [118] J. A. Fernandez-Baca, P. Dai, H. Y. Hwang, C. Kloc, and S. W. Cheong, *Phys. Rev. Lett.* **80**, 4012 (1998).
- [119] G. Papavassiliou, M. Belesi, M. Fardis, and C. Dimitropoulos, *Phys. Rev. Lett.* **87**, 177204 (2001).
- [120] W. Jiang, X. Zhou, G. Williams, R. Privezentsev, and Y. Mukovskii, *Physical Review B* **79**, 214433 (2009).
- [121] M. Pissas and G. Papavassiliou, *J. Phys.: Condens. Matter* **16**, 6527 (2004).
- [122] M. Hennion and F. Moussa, *New Journal of Physics* **7**, 84 (2005).
- [123] S. Petit, M. Hennion, F. Moussa, D. Lamago, A. Ivanov, Y. Mukovskii, and D. Shulyatev, *Phys. Rev. Lett.* **102**, 207201 (2009).
- [124] M. Hennion, F. Moussa, P. Lehouelleur, F. Wang, A. Ivanov, Y. Mukovskii, and D. Shulyatev, *Phys. Rev. Lett.* **94**, 057006 (2005).
- [125] J. Zhang, P. Dai, J. Fernandez-Baca, E. Plummer, Y. Tomioka, and Y. Tokura, *Phys. Rev. Lett.* **86**, 3823 (2001).
- [126] W. Reichardt and M. Braden, *Physica B* **263-264**, 416 (1999).
- [127] H. Y. Hwang, P. Dai, S. W. Cheong, G. Aeppli, D. A. Tennant, and H. A. Mook, *Phys. Rev. Lett.* **80**, 1316 (1998).
- [128] P. Dai, H. Y. Hwang, J. Zhang, J. Fernandez-Baca, S. W. Cheong, C. Kloc, Y. Tomioka, and Y. Tokura, *Physical Review B* **61**, 9553 (2000).
- [129] N. Furukawa, *J. Phys. Soc. Jpn.* **68**, 2522 (1999).
- [130] J. Zhang, F. Ye, H. Sha, P. Dai, J. A. Fernandez-Baca, and E. W. Plummer, *J. Phys.: Condens. Matter* **19**, 315204 (2007).
- [131] T.-M. Cheng and L. Li, *Journal of Magnetism and Magnetic Materials* **320**, 1 (2008).

Appendix: Letter of Permission



AMERICAN PHYSICAL SOCIETY

One Physics Ellipse, College Park, MD 20740 · <http://www.aps.org>

March 31, 2014

Dalgis Mesa
Physics Graduate Student
Louisiana State University
Department of Physics & Astronomy
202 Nicholson Hall, Tower Dr. # 133
Baton Rouge, LA 70803-4001

Ref # 26315

Thank you for your permission request dated Mar. 3, 2014. We are pleased to grant you a non-exclusive, non-transferable permission, English rights, limited to **print and electronic format**, provided you meet the criteria outlined below. Permission is for a one-time use and does not include permission for future editions, updates, databases, translations, or any other matters. Permission must be sought for each additional use. This permission does not include the right to modify APS material.

Please print the required copyright credit line on the first page that the material appears: "Reprinted (abstract/excerpt/figure) with permission from [FULL REFERENCE CITATION] as follows: authors names, journal title, volume number, page number and year of publication. Copyright (YEAR) by the American Physical Society.

The following language must appear somewhere on the website: "Readers may view, browse, and/or download material for temporary copying purposes only, provided these uses are for noncommercial personal purposes. Except as provided by law, this material may not be further reproduced, distributed, transmitted, modified, adapted, performed, displayed, published, or sold in whole or part, without prior written permission from the American Physical Society."

Provide a hyperlink from the reprinted APS material (the hyperlink may be embedded in the copyright credit line). APS's link manager technology makes it convenient and easy to provide links to individual articles in APS journals. For information, see: <http://link.aps.org/>.

You must also obtain permission from at least one of the authors for each separate work, if you haven't done so already. The author's name and address can be found on the first page of the published Article.

Use of the APS material must not imply any endorsement by the American Physical Society.

Permission is granted for use of the following APS material only:

- Phys. Rev. B 78, 052410 – Published 27 August 2008
- Phys. Rev. B 85, 180410(R) – Published 25 May 2012

Permission is limited to the single title specified of the publication as follows:

A thesis entitled "NEUTRON SCATTERING STUDIES OF UNUSUAL SPIN STRUCTURE AND LOCAL CORRELATION IN COMPLEX OXIDES" to be published by Louisiana State University.

If you have any questions, please refer to the Copyright FAQ at: <http://publish.aps.org/copyrightFAQ.html> or send an email to assocpub@aps.org.

Sincerely,

A handwritten signature in black ink that reads "Jamie L. Casey". The signature is written in a cursive style.

Jamie L. Casey
Circulation and Fulfillment Assistant

Vita

Dalgis Mesa is a native of Havana, Cuba. She graduated from Florida International University in Miami, Florida with a Bachelor of Science in Physics in the year 2007. Miss Mesa started her graduate studies in Physics at Florida International University in the year 2007. In January of 2010, she transferred to the Department of Physics and Astronomy at Louisiana State University in Baton Rouge, Louisiana to continue with the doctoral program. Dalgis expects to receive her Doctor of Philosophy degree in Physics in May of 2014.